ADVANCED QUASIPARTICLE INTERFERENCE IMAGING FOR COMPLEX SUPERCONDUCTORS

A Dissertation

Presented to the Faculty of the Graduate School

of Cornell University

in Partial Fulfillment of the Requirements for the Degree of

Doctor of Philosophy

by

Rahul Sharma

May 2020

ADVANCED QUASIPARTICLE INTERFERENCE IMAGING FOR COMPLEX SUPERCONDUCTORS

Rahul Sharma, Ph.D.

Cornell University 2020

State-of-the-art low-temperature spectroscopic imaging scanning tunneling microscopy offers a powerful tool to study materials with unprecedented spatial (subangstrom) and energy (micro-electronvolts) resolution. Imaging the quasiparticle interference of eigenstates in a material, offers a window into the underlying Hamiltonian. In this thesis, we performed quasiparticle interference imaging under extreme (milliKelvin temperatures) conditions and developed novel analysis techniques to address important contemporary problems in superconductivity which have defied complete understanding due to their complex multiband nature and small energy scales.

Discovered almost 25 years ago, the momentum space gap structure of Sr_2RuO_4 has remained a mystery despite being an intensely researched topic due to possibilities of correlated and topological superconductivity. The multiband nature of Sr_2RuO_4 makes the problem complicated because usual thermodynamical probes cannot directly reveal which bands the subgap quasiparticles are coming from. Our first advanced approach addresses this problem by applying milliKelvin spectroscopic imaging scanning tunneling microscopy (SI-STM) to visualize the Bogoliubov quasiparticle interference (BQPI) pattern deep within the superconducting gap at T=90 mK. From T-matrix modeling of the subgap scattering, we are able to conclude that the major gap lies on $\alpha : \beta$ bands and the minima/nodes lie along $(\pm 1, \pm 1)$ directions. Further angular analysis of

the scattering features reveals that the nodes must be within 0.05 radians of the $(0,0) \rightarrow (\pm 1, \pm 1)$ lines. These observations, along with the other theoretical and experimental literature at the present moment, are most consistent with a $B1_g$ symmetry ($d_{x^2-y^2}$-wave) gap on $\alpha : \beta$ bands of Sr_2RuO_4. This conclusion indicates that Sr_2RuO_4 may not be a chiral odd-parity superconductor as believed for many years.

While many techniques exist to measure the magnitude of the superconducting gap, only a few can probe its phase. High-quality BQPI patterns can be analyzed for phase information to determine the sign of the gap. Such techniques rely on centering a single atomic defect in the field of view (FOV). Since the defect concentration determines the BQPI signal intensity, this usually forces the choice of a smaller field of view, limiting the momentum-space resolution and the BQPI signal intensity. As a second advanced approach, we implement quantum phase-sensitive technique which can work with multiple atomic defects in the FOV. We first show that our multiple atom phase-analysis technique reproduces the results for FeSe, a material previously studied with single impurity phase-analysis. Then we implement our technique to study LiFeAs. Our multi-atom analysis reveals that the gap sign changes from hole band to electron band. This establishes that the gap symmetry in LiFeAs is $s_{\pm}$. This multi-atom innovation extends applicability to more disordered superconductors, enables its application to larger fields of view thereby enhancing k-space resolution, and greatly increases the signal to noise ratio by suppressing phase randomization due to scattering interference coming from multiple atomic centers. Overall, it represents a powerful and general new approach for the determination of the superconducting order-parameter for complex superconductors.

BIOGRAPHICAL SKETCH

Rahul Sharma was born on August 27th, 1990 in the city of Varanasi on the banks of holy river Ganga. He grew up in a working-class neighborhood with his loving mother and three sisters. He went to school at Kendriya Vidyalaya, a small local government-run school. As a kid, he was always interested in making toys, trying to figure out magic tricks, which perhaps were indications of the things to come. He also studied Indian classical percussion instrument, Tabla, apart from his studies during his formative years at Varanasi.

He went to the Indian Institute of Technology Bombay where he completed an Integrated B-Tech M.-Tech Dual Degree Program in Engineering Physics with a Minor in Electrical Engineering. His interest was piqued in condensed matter physics with a seminar course he did with Prof. Alok Shukla in 2011. He later got an opportunity to do a summer internship in 2012 at Penn State University with Prof. Nitin Samarth where he performed experiments on topological insulators. For his Masters's thesis, he performed experiments at IIT-Bombay and Tata Institute of Fundamental Research under the guidance of Prof. Parinda Vasa to study non-linear optics and plasmonics of nanostructures and nanoparticles. For his overall academic performance in the class of 2014, he was awarded the Institute Gold medal.

For graduate school, he chose to come to Cornell which is known for its low temperatures in both physics and life! He worked with Prof. Davis on performing millikelvin spectroscopic imaging scanning tunneling microscopy experiments on exotic superconductors. Apart from searching for exotic phase transitions in nature by looking at atoms and wavefunctions in real and reciprocal space, he also likes to experiment with flour, fat and sugar to look for tasty phase transitions in the world of baking.

Dedicated to Maa who made everything possible

ACKNOWLEDGEMENTS

Words are not enough, but I first and foremost would like to thank my mother, whose faith in me knows no bounds. When my father passed away when I was 4, she had to take up the work to support our family. Despite not much formal education, she did it all and braved the harsh world to make sure her kids get educated to the highest standards. Despite her frail health she decided to send me to the US so that I can pursue my research dreams. Her love and faith has been the strongest feature which made this thesis possible.

I would like to thank all my colleagues and friends who provided great camaraderie. Yi Xue, who was omnipresent and eager to help like I had an extra pair of hands. He's been a great source of calm and entertainment, driving us to dinners, movies and all the fun. Peter, who was like a wise elder brother and always guided me in the right direction. Yi Xue and he held me a lot of times when I fell and always willing to help and talk. Steve from whom I learned a lot about Science, Life and professionalism. Andrey Kostin, who was a great source of intellectual stimulation and inspired a life-changing and lifelong love of physical fitness. Andreas, Xiaolong, Kazu, Mo and Chung-Koo, who shared their knowledge freely. Ritika for being the sweet sister from the same culture. Azar for interesting discussions. Younger colleagues and friends Varshith, Jesse, Elizabeth Benjamin, Andrew and Tabatha for providing opportunities for stimulating physics discussions and enjoyable lunch breaks. All friends from Physics and AEP from my class for being really nice and bringing a smile to my face whenever I see them in corridors of Clark Hall.

I would like to thank all the staff at LASSP who assisted me during my years in multiple ways to make my research as smooth as possible. Eric for providing a perennial supply liquid Helium and rich experience of low-temperature

physics instrumentation. Nate from whom I learned the art of machining, a skill I really cherish. All the machine shop wizards, Robert, Stan, Jeff and Chris helped bring me design dreams to reality. Robert Spankle at the LASSP store took all the hassle of ordering lab equipment away by being super helpful and efficient. Jason, Bob, Todd and others who helped us move our heavy equipment around and took care of our sophisticated electrical and structural infrastructure of lab. All the custodial staff, who maintained our labs in clean working conditions.

Last but not the least, I would like to thank my advisor Prof. Séamus Davis whose enthusiasm for physics is contagious and known no bounds. Performing research under him was a great learning experience. He never let me feel any lack of resources. His reply to a flood in our lab was "Good!"! This reflects his never-fail attitude and I hope to emulate his scientific temperament in my own life and spread it as far as I can.

TABLE OF CONTENTS

LIST OF TABLES

LIST OF FIGURES

CHAPTER 1

COMPLEX SUPERCONDUCTIVITY

The first glimpses of superconducting phenomena, a chunk of material floating on the top of a magnet and moving on a rail are really awe-inspiring and create a lasting impression. As I learned more about their physics, starting from undergraduate education, the mysteries of mother Nature in creating something so extraordinary, a macroscopic quantum state of matter was one of the biggest inspirations for me to take up research in condensed matter physics.

In this chapter, we will discuss the mathematical formalism to see how such a fascinating quantum state materializes. This will lay the groundwork which will enable us to look at the systems where observed superconductivity seems to defy conventional understanding, which we deem complex in this thesis. We will examine the generalizations in the conventional formalism which are required to understand complex superconductivity.

1.1 Conventional Superconductivity

On the 8th of April 1911, Henry Kamerlingh Onnes discovered that the resistivity of mercury wire vanishes when dipped in liquid Helium (at 4.2K). He immediately realized the significance of his discovery as he wrote in his lab notebook *" Mercury has passed into a new state, which on account of its extraordinary electrical properties may be called the superconductive state"* [1]. Many great minds of 20th century tried to understand why mother Nature produces this new superconducting state. The names include Einstein, Feynman and many others stalwarts of Physics, but it was not until after decades later that this mystery of nature was

finally solved in 1957 with joint efforts of John Bardeen, Leon Cooper and John R. Schrieffer (BCS) [2]. In this section, we will follow their treatment to understand why superconductivity occurs. We will also see an equivalent mean-field treatment which is less cumbersome in dealing with excited states of superconducting ground states, which are the excitations involved in our tunneling experiments.

1.1.1 Cooper Pairs

First came the realization due to Cooper in 1956 [3], that the metals are unstable! More precisely, a filled Fermi sea of electrons is unstable to the pairing of electrons for arbitrarily weak attractive interactions. For our purposes, we will describe this phenomenology by closely following Tinkham [4]. Let us consider two electrons above Fermi sea ($k > k_F$) which do not interact with Fermi sea apart from the Pauli's exclusion principle. The joint wavefunction can be written as

$$\psi(\mathbf{r}_2, \mathbf{r}_2) = \sum_{\mathbf{k}} g_{\mathbf{k}} e^{i\mathbf{k}\cdot\mathbf{r}_1} e^{-i\mathbf{k}\cdot\mathbf{r}_2} \tag{1.1}$$

Notice that we are considering a wavefunction with zero net momentum. The total wavefunction of a pair of electrons has to be antisymmetric. Anticipating an attractive interaction, we can the choose cosine part in the exponential, as it has higher values for $\mathbf{r}_1$ close to $\mathbf{r}_2$. Since the orbital part is this chosen to be even, the spin part has to be odd i.e. a spin-singlet [1] Hence overall wavefunction

[1] One of the materials under study in this thesis was touted to be a spin-triplet superconductor with an odd parity wavefunction. In general, depending upon the nature of the interactions leading to the attractive potential to pair the electrons (pairing glue), the wavefunction may differ from this ideal form. We revisit this issue in section 1.2 and generalize this formalism to include spin-triplet pairing as well.

can be written as:

$$\psi(\mathbf{r}_2, \mathbf{r}_2) = \sum_{k>k_F} g_{\mathbf{k}} \cos \mathbf{k} \cdot (\mathbf{r}_1 - \mathbf{r}_2) \left(|1\uparrow\rangle|2\downarrow\rangle - |2\downarrow\rangle|1\uparrow\rangle\right) \tag{1.2}$$

We insert the Cooper wavefunction (1.2) into the schrödinger equation $H_{\text{unpert.}}\psi + V_{\mathbf{k}\mathbf{k}'}\psi = E\psi$, where we have a possible attractive term, $V_{\mathbf{k}\mathbf{k}'}$ which scatters a Cooper pair $(\mathbf{k}', -\mathbf{k}')$ to $(\mathbf{k}, -\mathbf{k})$. Collecting coefficients of state $\mathbf{k}$, we get the unperturbed energy of the two electrons $\epsilon_{\mathbf{k}}$ and the additional term due to the attractive potential, adding to give the total energy as:

$$2\epsilon_{\mathbf{k}} g_{\mathbf{k}} + \sum_{k'>k_F} V_{\mathbf{k}\mathbf{k}'} g_{\mathbf{k}'} = E g_{\mathbf{k}} \tag{1.3}$$

If for some set of $g_{\mathbf{k}}$ satisfying the Schrödinger equation (1.3), the total energy $E < 2E_F$, then there is a net energy gain of $2E_F - E$ from forming a pair and the Fermi surface (metal) will be unstable! Cooper introduced a simplifying assumption to see this. We take $V_{\mathbf{k}\mathbf{k}'} = -V$, where V is a positive number, up to a cutoff energy $\hbar\omega_c$ outside the Fermi level, and 0 beyond the cutoff $\hbar\omega_c$. This is basically an attractive force, close to the Fermi surface.

$$V_{\mathbf{k},\mathbf{k}'} = \begin{cases} -V & \text{if } \epsilon_{\mathbf{k}} \text{ and } \epsilon_{\mathbf{k}'} \text{ are both} < E_F + \hbar\omega_c \\ 0 & \text{otherwise} \end{cases} \tag{1.4}$$

With this assumption, the $V_{\mathbf{k}\mathbf{k}'}$ can be taken out of the sum in schrödinger equation (1.3) and we get:

$$\begin{aligned} 2\epsilon_{\mathbf{k}} g_{\mathbf{k}} - V \sum_{k'>k_F} g_{\mathbf{k}'} &= E g_{\mathbf{k}} \\ \implies \frac{g_{\mathbf{k}}}{V} &= \frac{\sum_{k>k_F} g_{\mathbf{k}}}{2\epsilon_{\mathbf{k}} - E} \end{aligned} \tag{1.5}$$

We can sum over both sides $\sum_{k>k_F}$ to cancel out $\sum_{k>k_F} g_{\mathbf{k}}$ and get

$$\frac{1}{V} = \sum_{k>k_F} \frac{1}{2\epsilon_{\mathbf{k}} - E} \tag{1.6}$$

This sum can be changed to an integral, using the density of states at the Fermi level $N(0)$, and keeping in mind that this integral will only run from E_F to the cutoff energy $E_F + \hbar\omega_c$, where $N(0)$ is (effectively constant) density of states. This is true only when $\hbar\omega_c \ll E_F$, which is generally true for most metals. This gives us

$$\begin{aligned}
\frac{1}{V} &= N(0) \int_{E_F}^{E_F+\hbar\omega_c} \frac{d\epsilon}{2\epsilon - E} \\
&= \frac{1}{2} N(0) \ln \frac{2E_F - E + 2\hbar\omega_c}{2E_F - E} \\
\implies e^{\frac{2}{N(0)V}} &= \frac{2E_F - E + 2\hbar\omega_c}{2E_F - E} \\
\implies 2E_F - E &= 2E_F e^{-\frac{2}{N(0)V}} - E e^{-\frac{2}{N(0)V}} + 2\hbar\omega_c e^{-\frac{2}{N(0)V}} \\
\implies E(1 - e^{-\frac{2}{N(0)V}}) &= 2E_F(1 - e^{-\frac{2}{N(0)V}}) - 2\hbar\omega_c e^{-\frac{2}{N(0)V}}
\end{aligned} \tag{1.7}$$

In most classic superconductors $N(0)V < 0.3$ and we can make the approximation $N(0)V \ll 1 \implies 1 - e^{-\frac{2}{N(0)V}} \approx 1$. This finally gives us:

$$E \approx 2E_F - 2\hbar\omega_c e^{-\frac{2}{N(0)V}} \tag{1.8}$$

Hence, there is energy of the order of $2\hbar\omega_c e^{-\frac{1}{N(0)V}}$ is to be gained by pairing, and the Fermi surface will be unstable to formation of these Cooper pairs! It can be noted that the form of the binding energy is not analytic as V goes to 0, i.e. it cannot be expanded in powers of V, this is the reason that this was outside the realm of perturbation theory and cracking this problem took so long.

Question now is, where does this weak attractive interaction may come from in a metal? The ideas for this weak attractive force were actually developed before the BCS theory by Fröhlich who realized that the ion of lattice might have a role to play in superconductivity [5]. An intuitive picture is that when a negatively charged electron travels in a lattice, it pulls the positively charged lattice towards it a bit and leaves this trail of slightly positive charge, which might attract another moving electron towards it. This is possible since the lattice dynamics are much slower compared to electrons due to their enormous mass difference. However, at much shorter distances, this interaction becomes repulsive and limits the highest achieved critical temperature [6], at which the superconductivity goes away.

Since the size of a Cooper pair is critical to ensure attractive interaction, let us make a quick hand waving estimation about the size of the Cooper pairs using the Uncertainty principle limit.

$$\delta x \delta p \approx \hbar \tag{1.9}$$

The energy of a Cooper-pair can be estimated to be of the order of 2Δ where Δ is the superconducting gap, ~ the energy to break a Cooper-pair (we will see in a later section). Then

$$\begin{aligned} \delta\left(\frac{p^2}{2m}\right) &\approx 2\Delta \\ \implies \delta p\left(\frac{p_F}{m}\right) &= 2\Delta \\ \implies \delta p &= \frac{2m\Delta}{p_F} \end{aligned} \tag{1.10}$$

Where we have used the estimate for the momentum of the Cooper pair, since

they are close to Fermi surface, as p_F. This gives us the size of Cooper pair ξ as:

$$\begin{aligned} \xi &\approx \frac{\hbar}{\delta p} = \frac{\hbar p_F}{2m\Delta} = \frac{\hbar^2 k_F}{2m\Delta} = \frac{\hbar^2 k_F^2}{2mk_F\Delta} \\ \implies \xi &\approx \frac{E_F}{k_F\Delta} \end{aligned} \tag{1.11}$$

This number is on the order of 1000 Å for conventional superconductors, which is about 1000 atomic spacings! Hence Cooper pairs are highly overlapping and extend over 100s of atoms!

1.1.2 BCS Formalism

We start with the BCS Hamiltonian, which involves the attractive pairing interaction $V_{\mathbf{k}\mathbf{k}'}$ suggested by Cooper, which leads to Cooper pairing and resulting instability of Fermi-surface:

$$H_{\text{BCS}} = \sum_{\mathbf{k}\sigma} \epsilon_{\mathbf{k}} c^\dagger_{\mathbf{k}\sigma} c_{\mathbf{k}\sigma} + \sum_{\mathbf{k},\mathbf{k}'} V_{\mathbf{k},\mathbf{k}'} c^\dagger_{\mathbf{k}\uparrow} c^\dagger_{-\mathbf{k}\downarrow} c_{-\mathbf{k}'\downarrow} c_{\mathbf{k}'\uparrow} \tag{1.12}$$

The most general N-particle wavefunction which can be written for this Hamiltonian is

$$|\psi_N\rangle = \sum g(\mathbf{k_1}, \ldots, \mathbf{k}_M) c^\dagger_{\mathbf{k}_1\uparrow} c^\dagger_{-\mathbf{k}_1\downarrow} \ldots c^\dagger_{\mathbf{k}_M\uparrow} c^\dagger_{-\mathbf{k}_M\downarrow} |0\rangle \tag{1.13}$$

Where $|0\rangle$ is the vacuum state with no particles and N/2 pairs are created with creation operations $c^\dagger_{\mathbf{k}_i\uparrow} c^\dagger_{-\mathbf{k}_i\downarrow}$ which occupy 1 to M values which are occupied in a given term with the weight g. The number of terms to determine however will be ${}^M C_N$, which will be huge ($10^{10^{20}}$)!

Another genius in the story of the solution of the issue of superconductivity was the flash of brilliance a 25-year-old graduate student Schrieffer had while

riding on a New York subway to attend an APS meeting in 1957. He realized that with such a large number of particles, one can only work with average occupancy and treat total number N in mean-field or only statistically. Then in a grand canonical ensemble, the total number need not be conserved. He wrote down the wavefunction on the subway [7]!

$$|\psi_{\text{BCS}}\rangle = \prod_{\mathbf{k}} \left(u_{\mathbf{k}} + v_{\mathbf{k}} c^{\dagger}_{\mathbf{k}\uparrow} c^{\dagger}_{-\mathbf{k},\downarrow}\right)|0\rangle \tag{1.14}$$

Where $u_{\mathbf{k}}$ and $v_{\mathbf{k}}$ are complex coefficients with $|u_{\mathbf{k}}|^2 + |v_{\mathbf{k}}|^2 = 1$. Inspecting the wavefunction, one can see that the probability of a pair state ($\mathbf{k}\uparrow, -\mathbf{k}\downarrow$) being occupied is $|v_{\mathbf{k}}|^2$ and the probability of it being unoccupied is $|u_{\mathbf{k}}|^2 = 1 - |v_{\mathbf{k}}|^2$. Also, it can be noted that this wavefunction is actually a superposition of states each containing a fixed number of Cooper pairs. Due to the superposition, the number is uncertain in this wavefunction, but due to number and phase being conjugate variables [4], the phase for this wavefunction is fixed, as $u_{\mathbf{k}}$ and $v_{\mathbf{k}}$ are complex numbers and, in general, will have a phase relationship between them. This well-defined phase or macroscopic phase coherence of wavefunction is the key property of a superconductor which makes it a macroscopic quantum material and we discuss this at length in Appendix B and derive electrodynamical properties of Superconductors from this property of having a well-defined phase. The mean number of particles and fluctuations from this mean can also be calculated and it can be seen that the assumption of mean N being large and fluctuations from this mean being small is also valid [4].

This wavefunction can be used to variationally minimize the free energy $H-\mu N$ in the grand canonical ensemble, to find the values for $u_{\mathbf{k}}$ and $v_{\mathbf{k}}$ and solve the Hamiltonian to get energy spectrum. However this is quite cumbersome and we will solve the problem using a more modern approach of Hartree-Fock mean-field theory [8] in the next section. For variational treatment, please see

Tinkham [4].

1.1.3 Mean-Field Formalism

The key idea in BCS theory is that the statistical mean number of pairs is large in the superconducting state and the fluctuations from this mean are small. This allows us to use Hartree-Fock mean-field treatment to rewrite the BCS Hamiltonian. In Hartree-Fock mean-field treatment, we choose a mean-field order parameter, a quantity which is non-zero in the phase of interest. In our case of superconductivity, due to the phase coherence (or conversely because the number not being conserved, as number and phase are conjugate variables [4]) the operators like $c_{-\mathbf{k}\downarrow}c_{\mathbf{k}\uparrow}$ will have a non-zero value in the superconducting state, rather than averaging out to 0 as in normal metals. Hence we can write this operator as a sum of the mean-value (mean-field) and the fluctuations from this mean value, which will be small as BCS showed.

$$c_{-\mathbf{k}\downarrow}c_{\mathbf{k}\uparrow} = \langle c_{-\mathbf{k}\downarrow}c_{\mathbf{k}\uparrow}\rangle + (c_{-\mathbf{k}\downarrow}c_{\mathbf{k}\uparrow} - \langle c_{-\mathbf{k}\downarrow}c_{\mathbf{k}\uparrow}\rangle) \tag{1.15}$$

Inserting this expression into the BCS Hamiltonian (1.12), and ignoring the second-order terms in the fluctuation which is in the parenthesis in (1.15), we get the mean field Hamiltonian.

$$H_{\mathrm{BCS}}^{\mathrm{MF}} = \sum_{\mathbf{k}\sigma} \xi_{\mathbf{k}} c_{\mathbf{k}\sigma}^{\dagger} c_{\mathbf{k}\sigma} + \sum_{\mathbf{k}\mathbf{k}'} V_{\mathbf{k}\mathbf{k}'} \left(c_{\mathbf{k}\uparrow}^{\dagger} c_{-\mathbf{k}\downarrow}^{\dagger} \langle c_{-\mathbf{k}'\downarrow} c_{\mathbf{k}'\uparrow}\rangle + \langle c_{-\mathbf{k}\downarrow} c_{\mathbf{k}\uparrow}\rangle^{*} c_{-\mathbf{k}'\downarrow} c_{\mathbf{k}'\uparrow} - \langle c_{-\mathbf{k}\downarrow} c_{\mathbf{k}\uparrow}\rangle^{*} \langle c_{-\mathbf{k}\downarrow} c_{\mathbf{k}\uparrow}\rangle \right) \tag{1.16}$$

where we are measuring energies from chemical potential and $\xi_{\mathbf{k}}$ is simply $\epsilon_{\mathbf{k}} - \mu$,

μ being the chemical potential. We define the order parameter for superconductivity as

$$\Delta_{\mathbf{k}} = -\sum_{\mathbf{k}'} V_{\mathbf{k}\mathbf{k}'} \langle c_{-\mathbf{k}'\downarrow} c_{\mathbf{k}'\uparrow} \rangle \tag{1.17}$$

Then the final Mean-field Hamiltonian becomes

$$H_{\text{BCS}}^{\text{MF}} = \sum_{\mathbf{k}\sigma} \xi_{\mathbf{k}} c_{\mathbf{k}\sigma}^{\dagger} c_{\mathbf{k}\sigma} - \sum_{\mathbf{k}} \left(\Delta_{\mathbf{k}} c_{\mathbf{k}\uparrow}^{\dagger} c_{-\mathbf{k}\downarrow}^{\dagger} + \Delta_{\mathbf{k}}^{*} c_{-\mathbf{k}\downarrow} c_{\mathbf{k}\uparrow} \right) \tag{1.18}$$

where $\sum_{\mathbf{k}} \Delta_{\mathbf{k}} \langle c_{-\mathbf{k}\downarrow} c_{\mathbf{k}\uparrow} \rangle^{*}$ is a scalar and absorbed in the chemical potential. Hartree-Fock mean-field is a self-consistent solution method and the $\Delta_{\mathbf{k}}$ needs to be determined self-consistently using (1.17). Notice that the number in the Hamiltonian is no longer conserved and this mean-field Hamiltonian can create or destroy pairs. However, now the mean-field, the superconducting order parameter in (1.17) has a fixed phase. This again demonstrates the number and phase conjugation and is the defining feature of a superconductor as we discuss in Appendix B.

The mean-field Hamiltonian in (1.18) can be written as a matrix equation (after absorbing some scalar/non-operator terms into the chemical potential),in the basis vectors $\Psi_{\mathbf{k}}^{\dagger} = \left(c_{\mathbf{k}\uparrow}^{\dagger}, c_{-\mathbf{k}\downarrow} \right)$ as

$$H_{\text{BCS}}^{\text{MF}} = \sum_{\mathbf{k}} \Psi_{\mathbf{k}}^{\dagger} H_{\text{BdG}} \Psi_{\mathbf{k}} \tag{1.19}$$

The matrix H_{BdG} usually called the Bogoliubov de Gennes Hamiltonian as Bogoliubov [9] (and independently Valatin [10]) showed how to to diagonalize this Hamiltonian and is given as:

$$H_{\text{BdG}} = \begin{pmatrix} \xi_{\mathbf{k}} & \Delta_{\mathbf{k}} \\ \Delta_{\mathbf{k}}^{*} & -\xi_{\mathbf{k}} \end{pmatrix} \tag{1.20}$$

The linear transformations which diagonalize this Hamiltonian are called

Bogoliubov Transformations and given as [8]:

$$\begin{pmatrix} \gamma_{\mathbf{k}\uparrow} \\ \gamma^{\dagger}_{-\mathbf{k}\downarrow} \end{pmatrix} = \begin{pmatrix} u^{*}_{\mathbf{k}} & v_{\mathbf{k}} \\ -v^{*}_{\mathbf{k}} & u_{\mathbf{k}} \end{pmatrix} \begin{pmatrix} c_{\mathbf{k}\uparrow} \\ c^{\dagger}_{-\mathbf{k}\downarrow} \end{pmatrix} \tag{1.21}$$

It can be shown that the values of $u_{\mathbf{k}}$ and $v_{\mathbf{k}}$ which diagonalize the H_{BdG} are [8]

$$\begin{aligned} |u_{\mathbf{k}}|^2 &= \frac{1}{2}\left(1 + \frac{\xi_{\mathbf{k}}}{E_{\mathbf{k}}}\right) \\ |v_{\mathbf{k}}|^2 &= \frac{1}{2}\left(1 - \frac{\xi_{\mathbf{k}}}{E_{\mathbf{k}}}\right) \end{aligned} \tag{1.22}$$

where

$$E_{\mathbf{k}} = \sqrt{\xi^2_{\mathbf{k}} + |\Delta_{\mathbf{k}}|^2} \tag{1.23}$$

with these values, the mean-field Hamiltonian (1.18) becomes [8]

$$H^{\text{MF}}_{\text{BCS}} = \sum_{\mathbf{k}\sigma} E_{\mathbf{k}} \gamma^{\dagger}_{\mathbf{k}\sigma} \gamma_{\mathbf{k}\sigma} + \text{constant.} \tag{1.24}$$

Here we can see that we have new quasiparticles, with number operator $\gamma^{\dagger}_{\mathbf{k},\sigma}\gamma_{\mathbf{k},\sigma}$ and energy $E_{\mathbf{k}}$! These quasiparticles are called Bogoliubons and these are what, as we shall see in later chapters, SI-STM detects while tunneling into superconductors. Also, since they appear with energy $E_{\mathbf{k}}$, given by (E.11), the minimum energy required to spawn a Bogoliubon is the magnitude of the mean-field order parameter $|\Delta_{\mathbf{k}}|$. Hence the order-parameter plays the role of an energy gap, below which there are no quasiparticles as can be seen in fig. 1.1 and one needs to supply this energy $\Delta_{\mathbf{k}}$ to a Cooper-pair in the BCS ground state to break it and create a Bogoliubon $\gamma_{\mathbf{k}}$.

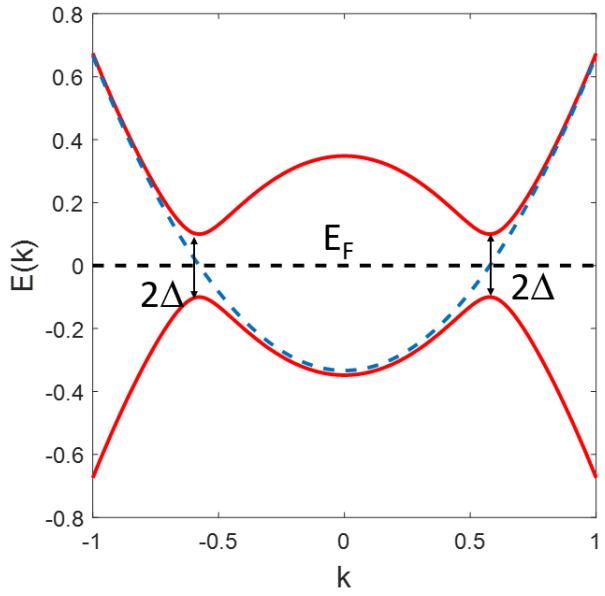

Figure 1.1: The Superconducting gap and the Bogoliubov quasiparticle dispersion. A gap of magnitude 2Δ opens at Fermi level E_F (black dashed line)in the normal state dispersion (blue dashed line) and Bogoliubov quasiparticle spectrum (red solid line) appears in the superconducting state.

1.2 Complex Superconductivity

We saw in the previous section that the defining characteristic of a superconductor is the appearance of a mean-field order parameter $\Delta_{\mathbf{k}}$ given in (1.17). This order parameter was defined with the pairing potential $V_{\mathbf{kk'}}$ which in the most simplified version (1.4) is just taken as a constant for all $\mathbf{k}$ on the Fermi surface for energies within a cutoff energy $\hbar\omega_c$ and the spins were always considered to pair in singlets, so we did not consider spin-dependence at all. We also discussed on how it comes about due to an electron-phonon (lattice) interaction in section 1.1.1. The Cooper-pair wavefunctions which form with this attractive interactions have a maximum at zero separation to take advantage of this attractive interaction to pair-up. This pairing is called s-wave which peak at $r = 0$ (think of s-orbitals on H-atom which also peak at $r = 0$, we will look at proper

group theoretical classification and nomenclature in sec 1.3.).

Mother Nature, however, is ever mysterious and it turns out that there are materials where the pairing interaction $V_{\mathbf{kk'}}$ may not be as simple and may have a spin-dependence and a form which doesn't allow a Cooper-pair to form with a constant Δ, but only if the $\Delta_{\mathbf{k}}$ has a form which creates an attractive interaction (pairing glue) out of the $V_{\mathbf{kk'}}$. Such superconductors are usually referred to as *unconventional superconductors*. The first discovered example of this important generalization was not a solid, but superfluid ^{3}He, a discovery made at Cornell [11]! The atoms are much larger than electrons and obviously have a hard core. It would be energetically costly to have a pairing wavefunction which is peaked at zero separation. It was discovered that the pairing actually occurs with a node at zero separation instead, in a p-wave symmetry (think of p-orbitals on H-atom, we will look at proper group theoretical classification and nomenclature in sec 1.3) [12]. Another well-known example is the high-temperature superconductor family of cuprates which have an order parameter symmetry of d-wave [13].

Even for such unconventional paired-fermion systems, my advisor Prof. Davis, a pioneer in superfluid ^{3}He physics [14] as well, likes to remark that *superfluid ^{3}He is the spherical cow of solid-state physics!*, This (I infer) is because it is a fluid and due to the lack of a lattice, the Fermi-surface is spherical which admitted to theoretical developments on standard models of condensed matter physics [12]. With a solid, having a lattice, one has to take into account the Fermi surface, the spin-orbit coupling and possible presence of multiple orbitals in the picture. Especially for multi-orbital systems, it is important to understand the $\Delta_{\mathbf{k}}$ for a complete understanding of the superconducting state in these materi-

als. In this section, we look at very basic definitions to enable us to talk about these new exotic states of matters. We first talk about important generalization where $\Delta_{\mathbf{k}}$ is no longer constant. The description of such superconductors is not so simple anymore [15] and one needs to expand the horizons of theory and experiment to understand these *complex superconductors*, which was the primary aim of this thesis.

1.2.1 Generalization of Order Parameter: Spin

The discussion of superconductivity in section 1.1 has been limited to a pairing interaction given in (1.4), where it is taken to be a constant, independent of $\mathbf{k}$ for energies within a cutoff energy $\hbar\omega_c$ over E_F. Also, in the BCS Hamiltonian, (1.12), the interaction term was constructed for only spin-singlets , pairing $\mathbf{k}\uparrow$ and $-\mathbf{k}\downarrow$. Mother nature provides examples of exotic states where these special cases are violated and exotic states of matter emerge. In this part, we will develop a theoretical framework to be able to address these generalizations.

We write the most general form of BCS Hamiltonian [16]:

$$H = \sum_{\mathbf{k}\sigma} \xi_{\mathbf{k}} c^{\dagger}_{\mathbf{k},\sigma} c_{\mathbf{k}\sigma} + \sum_{\mathbf{k}\mathbf{k}'\alpha\beta\gamma\delta} V_{\alpha\beta\gamma\delta}(\mathbf{k},\mathbf{k}') c^{\dagger}_{\mathbf{k}\alpha} c^{\dagger}_{-\mathbf{k}\beta} c_{-\mathbf{k}'\gamma} c_{\mathbf{k}'\delta} \tag{1.25}$$

Following the usual steps in the mean field treatment as spelled out in section 1.1.3, General BCS Hamiltonian (1.25) in the mean-field approximation becomes

$$H^{\mathrm{MF}} = \sum_{\mathbf{k}\sigma} \xi_{\mathbf{k}} c^{\dagger}_{\mathbf{k},\sigma} c_{\mathbf{k}\sigma} + \sum_{\mathbf{k}\alpha\beta} \left(c^{\dagger}_{\mathbf{k}\alpha} c^{\dagger}_{-\mathbf{k}\beta} \Delta_{\alpha\beta}(\mathbf{k}) + \Delta^{*}_{\alpha\beta}(\mathbf{k}) c_{-\mathbf{k}\alpha} c_{\mathbf{k}\beta} \right) \tag{1.26}$$

where we have defined the order parameter as a 2×2 matrix

$$\Delta_{\alpha\beta}(\mathbf{k}) = \sum_{\mathbf{k}'\gamma\delta} V_{\alpha\beta\gamma\delta}(\mathbf{k}, \mathbf{k}')\langle c_{-\mathbf{k}'\gamma} c_{\mathbf{k}'\delta}\rangle \tag{1.27}$$

Notice that the Fermion anti-commutation implies the parity symmetry for the order parameter will be given as

$$\Delta_{\alpha\beta}(\mathbf{k}) = -\Delta_{\beta\alpha}(-\mathbf{k}) \tag{1.28}$$

The 2×2 matrix order-parameter can be expressed in terms of a scalar order parameter $\Delta_{\mathbf{k}}$ and a vector order parameter $\mathbf{d}(\mathbf{k})$ as

$$\begin{pmatrix} \Delta_{\uparrow\uparrow}(\mathbf{k}) & \Delta_{\uparrow\downarrow}(\mathbf{k}) \\ \Delta_{\downarrow\uparrow}(\mathbf{k}) & \Delta_{\downarrow\downarrow}(\mathbf{k}) \end{pmatrix} = i(\Delta_{\mathbf{k}} I + \mathbf{d}(\mathbf{k}) \cdot \boldsymbol{\sigma})\sigma_y = \begin{pmatrix} -d_x(\mathbf{k}) + id_y(\mathbf{k}) & \Delta_{\mathbf{k}} + d_z(\mathbf{k}) \\ -\Delta_{\mathbf{k}} + d_z(\mathbf{k}) & d_x(\mathbf{k}) + id_y(\mathbf{k}) \end{pmatrix} \tag{1.29}$$

The parity of the general order parameter (1.28) now implies

$$\begin{aligned} \Delta_{\mathbf{k}} &= \Delta_{-\mathbf{k}} \\ \mathbf{d}(\mathbf{k}) &= -\mathbf{d}(-\mathbf{k}) \end{aligned} \tag{1.30}$$

Hence, the scalar order parameter is even and the vector order parameter is odd. Usually these cases occur separately because near T_c, the gap equation is linear and the solution must have a definite parity, while away from T_c, if T_c is different for both solutions, the one with more energy gain will win. However, we should not count out the wonders of Mother Nature as in principle, they are allowed. We have discussed spin-singlet systems in section 1.1.3. The

only confirmed system with a spin-triplet pairing till date is superfluid ^{3}He [11], however a lot of early research on Sr_2RuO_4 claimed that Sr_2RuO_4 may be a spin-triplet superconductor as well. This equivalently[2] means that the order parameter will be odd, meaning $\Delta_{\mathbf{k}} = 0$ and the vector order parameter $\mathbf{d}(\mathbf{k})$ is non-zero.

The Bogoliubov quasiparticle energies for this case of odd-parity superconductor, analogous to the case in mean-filed theory (E.11) is given as [16]:

$$E_{\mathbf{k}}^{\text{Odd-Parity SC}} = \sqrt{\xi_{\mathbf{k}}^2 + \mathbf{d}(\mathbf{k}) \cdot \mathbf{d}^*(\mathbf{k}) \pm |\mathbf{d}(\mathbf{k}) \times \mathbf{d}^*(\mathbf{k})|} \tag{1.31}$$

If $|\mathbf{d}(\mathbf{k}) \times \mathbf{d}^*(\mathbf{k})| = 0$, the pairing state is referred to as *unitary* and all electrons are Cooper paired. Also, the vector $\mathbf{d}(\mathbf{k})$ then can be physically identified as a vector having magnitude of the excitation-gap in Bogoliubov quasiparticle spectrum for pairs $(\mathbf{k}, -\mathbf{k})$. If $|\mathbf{d}(\mathbf{k}) \times \mathbf{d}^*(\mathbf{k})| \neq 0$, the the pairing state is referred to as *non-unitary* and the resulting states can have two gaps, one of which might even be zero, leading to finite quasiparticle density (not all electrons Cooper paired) at $T = 0$. Another notable fact about $\mathbf{d}(\mathbf{k})$ is that it is always perpendicular the the spins of the Cooper pair. A quick way to see is to have a $\mathbf{d}(\mathbf{k})||z$ i.e. $\mathbf{d}(\mathbf{k}) = (0, 0, d_z)$. Then, from (1.29), it can be seen that $\Delta_{\uparrow\uparrow}(\mathbf{k}) = \Delta_{\downarrow\downarrow}(\mathbf{k}) = 0$, hence the total spin S lies in xy plane , and $\mathbf{d}(\mathbf{k})||S$. (For detailed proof, see Appendix of [17, 18])

For Sr_2RuO_4, the triplet order parameters under scrutiny were:

$$\begin{aligned} \mathbf{d}(\mathbf{k}) &= (k_x + ik_y)\hat{\mathbf{z}} \quad \text{chiral p-wave} \\ \mathbf{d}(\mathbf{k}) &= k_x\hat{\mathbf{x}} + k_x\hat{\mathbf{y}} \quad \text{helical p-wave} \end{aligned} \tag{1.32}$$

[2]Overall Cooper pair wavefunction needs to be antisymmetric under exchange. Spin Triplet means that the spin part is symmetric, hence the orbital part has to be odd.

We will discuss what our experiment, in light of all the other experiments till date, implies for the fate of these order parameters in chapter 4 of this thesis.

1.2.2 Generalization of Order Parameter: k-dependence

Having seen that the freedom in choosing spin leads to more exotic order parameters, let us now examine the **k**-dependence. In this discussion we will suppress the spin index as we already discussed that in the previous section. Let us allow $V_{\mathbf{k}\mathbf{k}'}$ to depend on **k**, however it should still be invariant under simultaneous rotation of **k** and **k**′ so it can be expressed as [12] :

$$V_{\mathbf{k}\mathbf{k}'} = \sum_{\mathbf{k}} V_l(k,k') P_l\left(\hat{\mathbf{k}}\cdot\hat{\mathbf{k}}'\right) \tag{1.33}$$

where $P_l\left(\hat{\mathbf{k}}\cdot\hat{\mathbf{k}}'\right) = P_l(\cos(\theta_{\mathbf{k}\mathbf{k}'}))$ are the usual Legendre polynomials and $\theta_{\mathbf{k}\mathbf{k}'}$ is the angle between **k** and **k**′. This pairing potential is still unmanageable to solve the gap equation (1.3). To solve this issue, we can introduce a cutoff $\hbar\omega_c$ (as Cooper did originally) for each V_l:

$$V_l = \begin{cases} -V & \text{if } \epsilon_{\mathbf{k}} \text{ and } \epsilon_{\mathbf{k}'} \text{ are both} < \hbar\omega_c \\ 0 & \text{otherwise} \end{cases} \tag{1.34}$$

With this constraint and assuming that this cutoff $\hbar\omega_c$ is much larger than the maximum possible gap magnitude $|\Delta|$, if we solve the gap equation (1.3) with the generalized pairing potential (1.33), we find that different l values approximately decouple and the solution corresponds to $l = l_0$ for which the V_l is most negative (most attractive). A fairly well approximated expression for solution $\Delta_{\mathbf{k}}$ can be written in terms of Laplace's spherical harmonics $Y_{l_0 m}(\theta,\phi)$ where θ

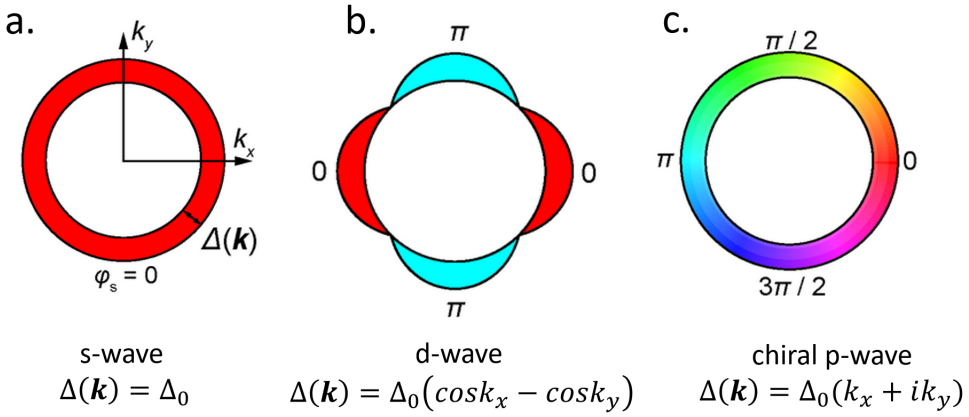

Figure 1.2: Illustration of various order parameter symmetries. a) A s-wave order parameter with a constant gap all around the Fermi surface. b) A d-wave order parameter with gap magnitude having 4 nodes and the sign of order parameter changing every $\pi/2$ rotation around Fermi surface. c) A chiral p-wave order parameter (A-phase of ^{3}He [11]) with constant magnitude around the Fermi surface but continuously changing phase. Figure reproduced from S. Yonezawa, Condens. Matter, 4(1), 2 (2019)

and ϕ are angles of $\mathbf{k}$ [12]

$$\Delta(\mathbf{k}) = \sum_m a_m Y_{l_0 m}(\theta, \phi) \tag{1.35}$$

This is where the nomenclature s-wave, p-wave and d-wave etc. comes from. Depending on l_0 where the attractive interaction V_{l_0} is maximum, a superconductor can be s-wave for $l_0 = 0$, p-wave for $l_0 = 1$ and d-wave for $l_0 = 2$ and so on. Superfluid ^{3}He [11] is a well-known example of a p-wave symmetry and and Cuprate superconductors [19, 20] are well-known examples of a d-wave symmetry. Fig. 1.2 shows an illustration of different order parameter symmetries.

We should remind ourselves here that the nomenclature s-wave, p-wave, d-wave etc. to refer to the symmetry of an order parameter makes sense in the spherically symmetric system where angular momentum l is a conserved

quantity. A more accurate way to refer to the pairing symmetry is to use Group symmetry classification scheme [21], which we shall discuss next.

1.3 Classification of Order Parameter Symmetry

For a quantum mechanical state ψ in a crystal, one can consider following symmetries

- Gauge symmetry: $\psi \rightarrow \psi e^{i\theta}$ (see Appendix A for details)
- Time translational symmetry: $\psi(t) \rightarrow \psi(t+T), \forall T$
- Space translational symmetry: $\psi(\mathbf{r}) \rightarrow \psi(\mathbf{r}+\mathbf{R}) \forall \mathbf{R}$
- Spin rotational symmetry
- Crystal point group symmetry

Gauge Symmetry

Despite popular terminology of spontaneous breaking of gauge symmetry, the gauge symmetry is never actually broken but a macroscopic phase is acquired in the superconducting state. Gauge invariance and gauge covariance of superconducting order parameter then, can explain all its fascinating properties like perfect conductivity, Meissner effect, flux quantization etc. See Appendix B for details. Apart from picking a macroscopic phase, if a superconductor breaks symmetries which are present in the normal state of the system, it is referred to as an *unconventional superconductor* [22].

Time and Space Translational Symmetry

The Cooper pairs we have considered thus far are of the form $\sim c^{\dagger}_{\mathbf{k}\sigma} c^{\dagger}_{-\mathbf{k}\sigma}$. This describes a Cooper pair with zero net center-of-mass momentum ($\mathbf{k} - \mathbf{k} = 0$) and no time dependence. Hence the space translational and time translational symmetry are preserved for such superconductors. There are two exotic states which break these symmetries. The translational symmetry can be broken if the Cooper-pairing takes place with finite momentum Q. Such a state will have the cooper-pair density modulate in real-space and generate a pair-density wave or PDW. It was originally proposed to exist in the magnetic-field by Fulde and Ferrel, and Larkin and Ovchinnikov hence it is dubbed FFLO state. Cuprate superconductors were also hypothesized to have this PDW [23] and it was discovered for the first time in Davis group [24, 25]! Similarly time translational symmetry can also, in principle be broken to lead to the so-called *odd-frequency-pairing*[26] and such states are proposed to exist in ferromagnet-superconductor multilayer systems.

Spin Rotational Symmetry

This has been discussed in detail in the section 1.2.1 and in conclusion, the odd ($d(\mathbf{k})$) or even ($\Delta(\mathbf{k})$) parity of the superconducting order parameter can be used to classify this symmetry.

Crystal Point Group Symmetry

A crystallographic point group is a set of symmetry operations, where each operation S in the set leaves the atoms of a crystal in the same place ($\psi(S\,r) = \psi(r)$).

A unique list of such operations is called an *irreducible representation* of the crystallographic point group. Among all these possible irreducible representations of symmetry operations allowed by a crystallographic point group, the superconducting order parameter $\Delta(\mathbf{k})$ in eq. (1.27) may pick one. This choice is a reflection of the pairing glue $V_{\mathbf{k}\mathbf{k}'}$. Rather than using s-wave, d-wave, p-wave which are terminologies coming from a spherically symmetric system where angular momentum is conserved, a more accurate way of referring to the symmetry of $\Delta(\mathbf{k})$ is to use the character table of the crystal under consideration which lists all possible irreducible representations. These irreducible representations can be figured out using the machinery of group theory [27, Chapter 12],[28], but are widely available for crystal point groups. Knowledge of magnitude and sign of $\Delta(\mathbf{k})$ enables figuring out how it would transform under the symmetry operations S, listed under different columns of the character table, by applying $S\Delta(\mathbf{k}) = q\Delta(\mathbf{k})$. A list of such q's will match one of the rows and that will be the symmetry of the superconducting order parameter $\Delta(\mathbf{k})$

For example, a character table of one of the materials studied in this thesis, Sr_2RuO_4 which has a D_{4h} crystallographic point group is shown in table 1.1. If a D_{4h} crystal point group material had a gap $\Delta(\mathbf{k}) = \Delta_0$, a constant, then it will be invariant under all the symmetry operations listed under the row i,e, $S\Delta(\mathbf{k}) = \Delta_0$ for all symmetry operations S in the columns. Hence all the q's are 1. The corresponding row is the first row, and such an order parameter would be called having an A_{1g} symmetry, which in the looser terminology of a spherically symmetric system referred to as a s-wave. Our SI-STM study of Sr_2RuO_4 is consistent with having a fourfold minima/node along diagonals of the Brillouin zone as we shall discuss in Ch. 4. In light of recent evidence, the simplest explanation is the order parameter having a B_{1g} which is referred to

as $d_{x^2-y^2}$-wave in the looser but more common spherically symmetric system terminology.

Respecting Brillouin Zone boundaries

Once the crystallographic point group symmetry of the gap is determined, the character table also lists the simplest functions which follow the same symmetry, hence they can be used to represent the function. However, to respect the Brillouin zone boundaries i.e. making sure that the function is periodic with respect to Brillouin zone, as a state in a crystal should be, we make the replacements

$$k \to \sin(k) \quad k^2 \to 1 - \cos(k) \tag{1.36}$$

For example, the B_{1g} symmetry for a D_{4h} crystal as listed in table 1.1, has the basis function $k_x^2 - k_y^2$. Hence with the above scheme, the gap function in a Brillouin zone can be represented as:

$$\begin{aligned} \Delta(k_x, k_y) &= \Delta_0((1 - \cos(k_x)) - (1 - \cos(k_y))) \\ &= \Delta_0(\cos(k_y) - \cos(k_x)) \end{aligned} \tag{1.37}$$

In this section for the classification of symmetry, we have not discussed the spin-orbit coupling. This works when the spin-orbit coupling is small. When spin-orbit coupling is large, the spin-rotation and crystal point group symmetries may be combined and transform together. We do not go into these details here but interested readers can find this discussion in Ref. [22, 21] and for the special case of Sr_2RuO_4, a list of all group theoretical possibilities can be found in Ref. [29].

	E	$2C_4$	C_2	$2C_2'$	$2C_2''$	i	$2S_4$	σ_z	$\sigma_{x,y}$	$\sigma_{d,d'}$	Basis	Nodes	Spin
A_{1g}	1	1	1	1	1	1	1	1	1	1	1	none	0
A_{2g}	1	1	1	-1	-1	1	1	1	-1	-1	$k_x k_y (k_x^2 - k_y^2)$	eightfold	0
B_{1g}	1	-1	1	1	-1	1	-1	1	1	-1	$k_x^2 - k_y^2$	fourfold diagonal	0
B_{2g}	1	-1	1	-1	1	1	-1	1	-1	1	$k_x k_y$	fourfold vert./horz.	0
E_g	2	0	-2	0	0	2	0	-2	0	0	$k_z(k_x, k_y)$	equator+twofold	0
A_{1u}	1	1	1	1	1	-1	1	-1	-1	-1	$k_x k_y k_z (k_x^2 - k_y^2)$	equator+eightfold	1
A_{2u}	1	1	1	-1	-1	-1	1	-1	1	1	k_z	equator	1
B_{1u}	1	-1	1	1	-1	-1	-1	-1	-1	1	$k_x k_y k_z$	equator+fourfold vert./horz.	1
B_{2u}	1	-1	1	-1	1	-1	-1	-1	1	-1	$k_z(k_x^2 - k_y^2)$	equator+fourfold diagonal	1
E_u	2	0	-2	0	0	-2	0	-2	0	0	$k_z(k_x, k_y)$	twofold (Real) none (complex)	1

Table 1.1: Character Table of D_{4h}. For details of notation, please see [28].

CHAPTER 2

SPECTROSCOPIC-IMAGING STM (SI-STM)

I was really awestruck by quantum tunneling while learning quantum mechanics as a new student. It is one of the most striking quantum phenomena which has no classical analog. Imagine a hill: a potential energy barrier, and a ball on one side of it. If the ball has enough energy, it will climb up and go down to pass this barrier and emerge on the other side of the hill. If the ball doesn't have enough energy, the ball cannot pass this barrier and emerge on the other side. However in the quantum world, the probability of a particle passing through an energy barrier is always finite, even if the energy of the particle is less than the energy of the barrier. This amazing phenomenon of *tunneling* forms the basis of the techniques used for the research presented in this thesis.

In this chapter, I introduce the formal tunneling framework under which we interpret SI-STM results. I explain briefly how an SI-STM functions, a technique which has led to important directions in quantum material research [30, 31, 32]. I mention some SI-STM specific issues and how to resolve them. I describe the dilution fridge at Cornell which enabled us to make discoveries about the order parameter of Sr_2RuO_4, a superconductor with very low $T_C = 1.45$K. I also layout the vibration and RF isolation employed in our lab which makes the sensitive measurements using our SI-STM possible by bringing the signal to noise ratio low enough so that measurements can be completed in time before the dewar runs out of liquid helium.

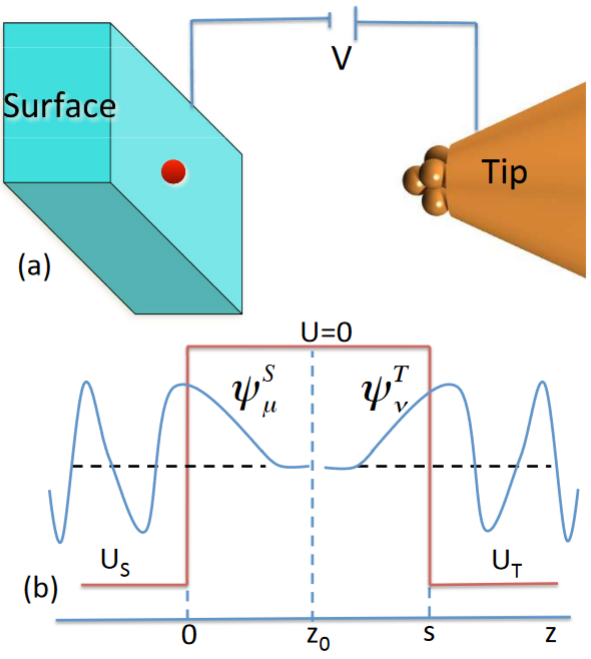

Figure 2.1: The tunneling setup a) STM schematic where a tip is in proximity with the sample surface. b) Corresponding potential energy landscape and wavefunctions in sample and tip. Wavefunctions existing in tip/sample decay in vacuum which acts as the energy barrier. Tunneling can take place if the distance is small enough for the wavefunctions to overlap. Figure reproduced from [33]

2.1 Tunneling Framework

Figure 2.1 shows a typical tunneling setup. There are two materials separated by an energy barrier. In the case of an STM, they are tip and sample separated by vacuum as shown in a). Tunneling takes place when particles from one side can pass through the barrier to appear on the other side. Essentially the Hamiltonian involves three parts: the sample Hamiltonian H_S, the tip Hamiltonian H_T and the Tunneling Hamiltonian H_M:

$$H = H_S + H_M + H_T \tag{2.1}$$

Bardeen [34] first provided the theoretical framework to track this problem with important assumptions which are employed in the interpretation of typical tunneling experiments. Tunneling is essentially treated as single-particle problem and electron-electron interactions in the tunneling Hamiltonian are ignored (However the sample and tip Hamiltonians can be many-body states). A direct interaction of tip and sample is not supposed to lead to coupled electron states, a reasonable assumption for typical tip-sample distances (5 Å).

When tip and sample are far from each other or unperturbed, the energy eigenstates $\psi^i_{\mathbf{k}}$ (where i can be S for the sample or T for the tip, $\mathbf{k}$ denotes the momentum basis) in them satisfy the Schrödinger equation:

$$\left(-\frac{\hbar^2}{2m}\frac{\partial^2}{\partial z^2} + U_i\right)\psi^i_{\mathbf{k}} = E_i\psi^i_{\mathbf{k}} \tag{2.2}$$

When tip is close enough so that the tunneling can occur, the time evolution of the wavefunction ψ, is governed by the Schrödinger equation with the full potential $U_S + U_T$ as:

$$\left(-\frac{\hbar^2}{2m}\frac{\partial^2}{\partial z^2} + U_S + U_T\right)\psi = i\hbar\frac{\partial\psi}{\partial t} \tag{2.3}$$

Since the time scale of electron dynamics is on the order of femtoseconds (10^{-15}s), much faster than the motion of the tip which is of the order of seconds, the term U_T can be considered to be turned on adiabatically. Under these assumptions, the term U_T can be treated under time-dependent perturbation theory and first-order result, famously known as Fermi's golden rule [35] gives us the rate of probability of transition from sample eigenstate to tip eigenstate, the tunneling rate $P^T_{\mathbf{kq}}(t)$ as:

$$P^T_{\mathbf{kq}}(t) = \frac{2\pi}{\hbar}\delta(E^S_{\mathbf{k}} - E^T_{\mathbf{q}})\left|M_{\mathbf{kq}}\right|^2 \tag{2.4}$$

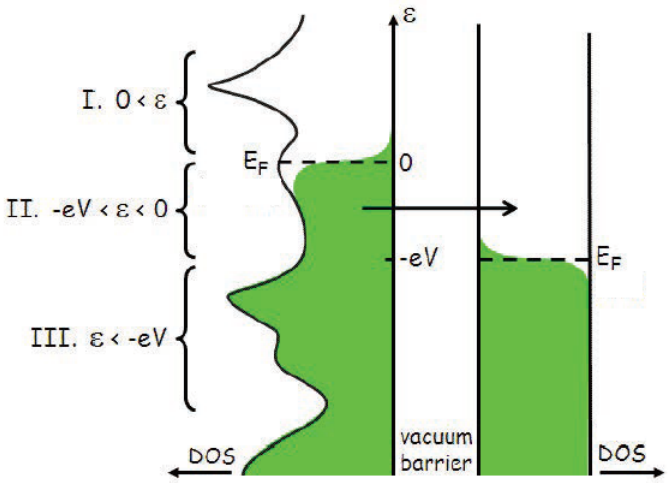

Figure 2.2: Schematic view of the tunneling from the sample to the tip. The sample is shown on the left and the tip on the right. Green color indicates occupied states. Tunneling can take place only from occupied states to unoccupied states (region II). The tip density of states (DOS) is shown flat, as is required to make useful inference about the sample density of states (DOS)

where $M_{\mathbf{kq}}$ is the tunneling matrix element

$$M_{\mathbf{kq}} = \langle \psi_{\mathbf{k}} | U_T | \psi_{\mathbf{q}} \rangle^2 \tag{2.5}$$

To get to the steady-state current, we need to sum over this single-particle tunneling rate. The tunneling can only occur from an occupied state in sample to unoccupied state in tip as shown in figure 2.2. We need to take care of this fact by introducing Fermi-Dirac density of states $f_{\mathbf{k}}$ which represents the occupation at non-zero temperatures. The steady-state current from sample to tip then, is given as:

$$I_{S\to T} = \frac{4\pi e}{\hbar} \sum_{\mathbf{k},\mathbf{q}} \left| M_{\mathbf{kq}} \right|^2 f_{\mathbf{k}} \left(1 - f_{\mathbf{q}}\right) \delta\left(E_{\mathbf{k}} - E_{\mathbf{q}}\right) \tag{2.6}$$

An additional factor of 2 takes the spin degeneracy of electrons into account, if the tip is not spin selective. Similarly, transition rate from the tip to the sample

can be written as:

$$I_{T\to S} = \frac{4\pi e}{\hbar}\sum_{\mathbf{k},\mathbf{q}} \left|M_{\mathbf{kq}}\right|^2 f_{\mathbf{q}}\left(1-f_{\mathbf{k}}\right)\delta\left(E_{\mathbf{q}}-E_{\mathbf{k}}\right) \tag{2.7}$$

The net current from the sample to the tip is:

$$I = I_{S\to T} - I_{T\to S}$$

If the chemical potential is the same for the tip and the sample, no current flows in equilibrium as $I_{T\to S}$ and $I_{S\to T}$ are both occupied to the same level and tunneling cannot take place (see Fig. 2.2). For a net current from the sample to the tip, a chemical potential difference between the sample and the tip is needed. This is provided in STM by a voltage difference of V between the tip and the sample. We can simplify the current expression by assuming that the matrix element is constant within eV of the chemical potential and we are very low temperatures $T \approx 0$ so that the Fermi-Dirac distribution is very sharp, and effectively a Heaviside distribution (step function) at E_F^i. The sum over momentum states $\mathbf{k}, \mathbf{q}$ can be converted into integral over energies using the density of states $N(E)$ $\sum_{\mathbf{k}} \to \int N(E)dE$. This gives us:

$$I = \frac{4\pi e}{\hbar}\left|M\right|^2 \int_0^{eV} N_S(E_F^S + E)N_T(E_F^T + E - eV)dE \tag{2.8}$$

To make a useful interpretation of the sample density of states $N_S(E)$, the tip density can be made independent of energy in the region of our interest. We ensure this in each of our measurements by preparing our Tungsten tip in-situ under cryogenic vacuum by applying a high voltage between the tip and a gold sample which causes field emission and changes the end of the tip. We continue this process unless we establish a sharp tip with a flat density of states in the tip as shown in figure 2.3. Assuming the tip density of states constant in our region of interest within eV, we finally get the tunneling current as:

$$I = \frac{4\pi e}{\hbar}\left|M\right|^2 N_T(E_F^T)\int_0^{eV} N_S(E_F^S + E)dE \tag{2.9}$$

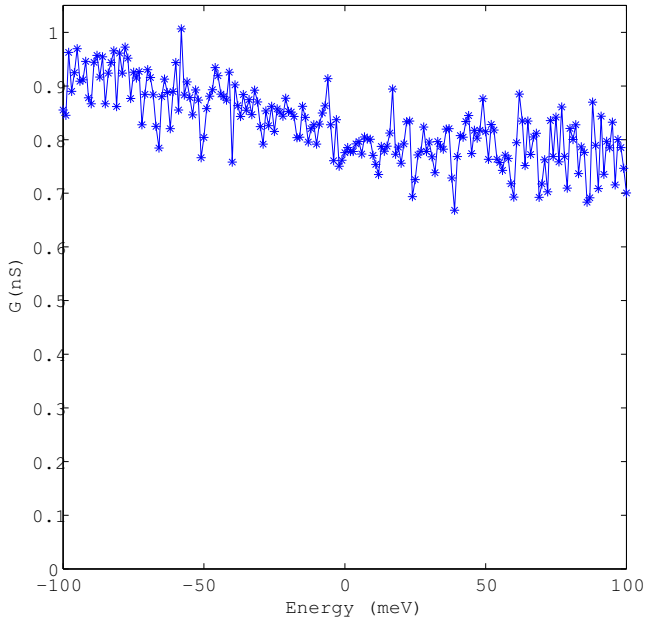

Figure 2.3: A typical spectrum of a prepared tip on a gold substrate. The density of states over a wide range of -100meV to 100meV varies only by 0.1 nS, effectively a constant density of states for our purposes.

Thus, the tunneling current in STM is the integrated density of states up to the bias voltage V. In SI-STM, we can also measure the differential conductance. By performing the differentiation with respect to V, we obtain:

$$\frac{dI}{dV} = \frac{4\pi e}{\hbar} |M|^2 N_T(E_F^T) N_S(E_F^S + eV) \propto N_S(E_F^S + eV) \tag{2.10}$$

This equation shows the unique power of SI-STM that it can access both occupied and unoccupied states (by applying positive or negative voltage bias) as the differential conductance is proportional to the density of states at any given location. At finite temperatures, the Fermi-Dirac distribution actually leads to a thermal smearing $\sim 3.5k_BT$ [30] as it is no longer sharp like a step function. This is why our dilution fridge STM operating at 90mK offers an energy resolution of $\sim 30\mu eV$, making the study of low Tc superconductors like Sr_2RuO_4 possible.

The matrix element M may play an important role in the interpretation of STM data [33] and we will discuss it as needed in further sections. However for

general purposes, we treat it as constant within our energy range eV. As figure 2.1 shows, the wavefunctions from the tip and sample decay exponentially in the barrier. Formally it can be treated under WKB approximation [35] for a square barrier. Though the bias voltage induces a tilt in the square barrier, the bias induced tilt eV is much smaller than the height of the barrier which is the energy required to pull an electron out of a material to the vacuum, the work function ϕ. According to WKB approximation $|M|^2 \propto e^{-2\gamma}$ where

$$\begin{aligned} \gamma &= \int_0^z \sqrt{\frac{2m\phi}{\hbar^2}} dz \\ &= \sqrt{\frac{2m\phi}{\hbar^2}} s \end{aligned} \tag{2.11}$$

Hence the tunneling current depends on the tip-sample separation z as

$$I \propto e^{-2z\sqrt{\frac{2m\phi}{\hbar^2}}} \tag{2.12}$$

Hence the tunneling current decays exponentially with the tip-sample separation z and the work-function ϕ of the material under study. Typical values for work-function is ~ 3-5 eV and typical values of tip-separation distance are 5-8Å.

2.2 SI-STM Observables

STM, as the name suggests, involves scanning a sharp tip across a sample with distance small enough so that the tunneling current is measurable. The tip movement is controlled by a piezo tube which can move up and down and scan in the 2D plane by application of voltage to the tube. A bias can be applied between the tip and the sample and the tunneling current acquired by the tip can be measured. We will discuss how this is achieved via the electronics in section 2.3.2. In this section, we describe the various measurements we can

make using an SI-STM and what are the steps involved in performing these measurements. We will also mention what are some error-correction techniques required to interpret these measurements to make physical deductions.

2.2.1 Topography

For our STM, we perform topographic scanning in constant current mode. From the expression for tunneling current in (2.9) and the the WKB approximation of matrix element as discussed in (2.12), the expression for tunneling current at a location $\mathbf{r}$ and bias voltage V can be written as [32]:

$$I(\mathbf{r}, V) = Ce^{-\frac{T(\mathbf{r})}{T_0}} \int_0^{eV} N(\mathbf{r}, E)dE \tag{2.13}$$

Where $N(\mathbf{r})$ is the local density of states of the sample, C is a constant which includes matrix element and $T(\mathbf{r})$ is the tip-surface distance, the so called *topograph*. If we set the current $I = I_S$, a constant setup current at a chosen setup voltage V_S, then the topograph $T(\mathbf{r})$, at a given junction at $\mathbf{r}$ is fixed by relations:

$$\begin{aligned} I_S &= Ce^{-\frac{T(\mathbf{r})}{T_0}} \int_0^{eV_S} N(\mathbf{r}, E)dE \\ \implies T(\mathbf{r}) &= T_0 \ln\left[\int_0^{eV_s} N(\mathbf{r}, E)\right] + \text{ const.} \end{aligned} \tag{2.14}$$

As the tip scans and starts to encounter variation in the tunneling current as a function of position (see eq. (2.13)), a feedback mechanism (as described in section 2.3.2) applies a suitable voltage to the scanning piezo-tube so that $T(\mathbf{r})$ is adjusted with the aim of keeping the tunneling current constant at $I = I_S$. $T(\mathbf{r})$ is recorded at each location and constitutes the topograph as shown in figure 2.4 recorded on Sr_2RuO_4.

One important caveat to note in the expression for topograph $T(\mathbf{r})$, is that

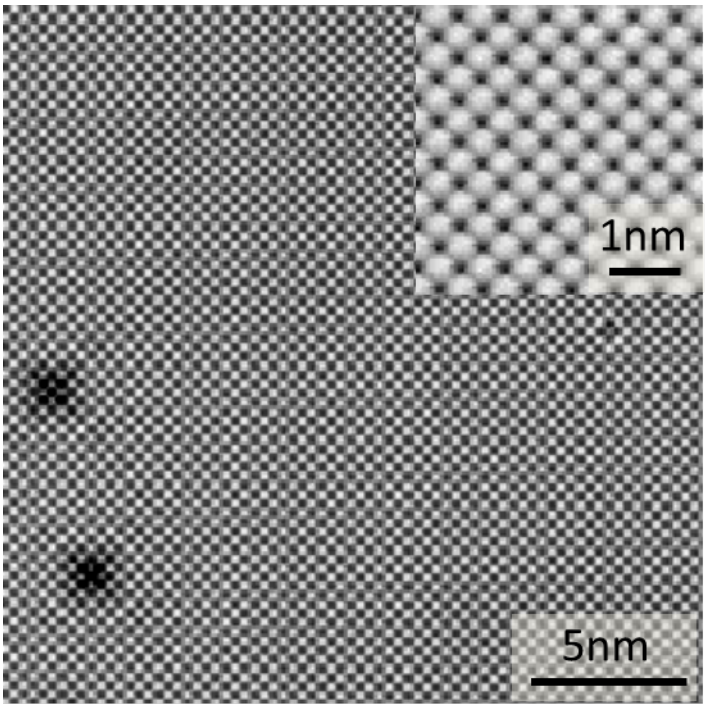

Figure 2.4: Topographic image recorded as explained in section 2.2.1 on Sr_2RuO_4. It clearly resolves the atoms and the point defects. The inset zooms in on the atoms. We believe that the cleaved layer is SrO as the crystal cleaves along the natural mirror symmetry plane.

it is a logarithmic measure of the integrated local density of states $N(\mathbf{r})$ up to the setup voltage V_S. Hence the bright spots seen in topographs need not always represent the atoms, as some other techniques like transmission electron microscopy (TEM) would as they are sensitive to the nuclei. But this is where the power of STM lies in being able to investigate exotic electronic phases of matter [32].

2.2.2 Spectroscopy

As equation (2.10) shows, the differential conductance $g = dI/dV$ is proportional to the density of states N, at a given height where the matrix element can be

taken to be constant (eq. (2.12)). The differential conductance can be measured accurately using a Lock-In technique where a particular frequency component in a signal can be *locked-in* and measured with high precision. We park our tip at a set height determined by the junction resistance between the tip and the sample which we set by choosing setup current I_S and setup voltage V_S and turn the feedback off so that the height does not change. Then we apply a small sinusoidal bias modulation $v(\omega) = v_0 \cos(\omega t + \phi)$ to the tip from the Lock-In and the current response is measured. The current response for a small bias modulation added on top of a setup voltage can be written using Taylor's expansion as:

$$I(V + v(\omega)) = I(V_S) + \left.\frac{dI}{dV}\right|_{V_S} \cdot v_0 \cos(\omega t + \phi) + \left.\frac{d^2I}{dV^2}\right|_{V_S} \cdot v_0 \cos^2(\omega t + \phi) \tag{2.15}$$

Hence the response at the bias modulation frequency ω is the first-order response which the Lock-In locks at and measures. This gives us dI/dV by direct measurement. These measurements can be done at a grid of desired V points $V_1, V_2, \ldots$ yielding $dI/dV(E = eV_1), dI/dV(E = eV_2), \ldots$ which is essentially the spectrum of density of states at the location of the tip (local density of states or LDOS). Figure 2.5 shows a spectrum obtained on superconducting Sr_2RuO_4 at $T = 90$mK. This shows the coherence peaks and suppression of the density of states in the superconducting gap.

2.2.3 Spectroscopic Imaging

The power offered by SI-STMs at Cornell arises from combining the scanning capabilities with spectroscopic capabilities, enabled by a design which is stable enough to perform these tasks as we will discuss in further sections in this chapter. This enables us to acquire $g(\mathbf{r}, E) = dI/dV(\mathbf{r}, E)$, a three-dimensional

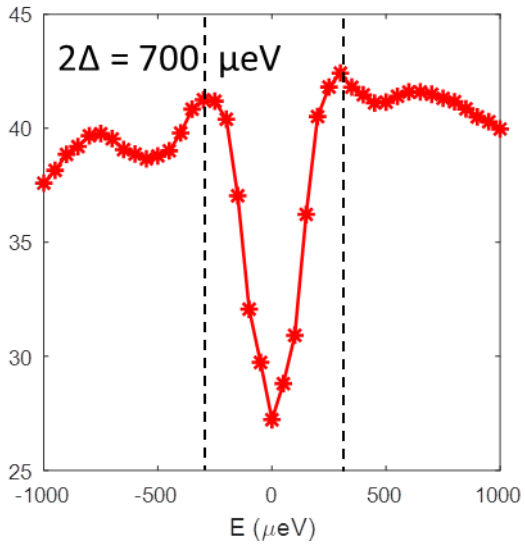

Figure 2.5: Spectrum recorded as explained in section 2.2.2 on superconducting Sr_2RuO_4 at T=90mK. It shows the suppression of density of states inside the superconducting gap of Sr_2RuO_4

dataset which contains immense amount of information and is analyzed in numerous ways to reveal various aspects [32]. To perform spectroscopic imaging, we choose the region of sample (spatial grid points) and the energy grid points at which we want spectrum $g(x_i, y_i, E_i) = dI/dV(x_i, y_i, E_i = eV_i)$ to be recorded. We define topographic setup by I_S^{topo} and V_S^{topo} at which we perform the scanning and spectroscopic setup by I_S^{spec} and V_S^{spec} at which we want to perform spectroscopy (see section 2.2.2). These values are chosen to fit the needs of the experiment and guided from earlier point spectroscopy and topography measurements. Then the SI-STM follows the following steps:

1. The tip moves to the point (x_1, y_1) scanning using the topographic setup (I_S^{topo}, V_S^{topo}).
2. After being located at (x_1, y_1), the setup changes to the spectroscopic setup (I_S^{spec}, V_S^{spec}).
3. The feedback is turned off to maintain the same height (see eq. (2.9) and

(2.12))

4. The bias voltage moves to the first desired Energy grid $E_1 = eV_1$.
5. The response current $I_1(x_1, y_1, E = eV_1)$ is recorded.
6. The small bias modulation is applied to the tip.
7. The response at the frequency of bias modulation $dI/dV(x_1, y_1, E = eV_1)$ is recorded. (as detailed in section 2.2.2)
8. Steps 3-7 are repeated for each $E_i = eV_i$
9. The feedback is turned on.
10. The tip moves back to the topographic setup
11. The tip moves to the next point in the desired spatial grid (x_2, y_2) and the process repeats for all (x_i, y_i), yielding the three-dimensional datasets $I(x_i, y_i, E_i = eV_i)$ and $g(x_i, y_i, E_i) = dI/dV(x_i, y_i, E_i = eV_i)$

2.2.4 Relevant Error Correction Techniques for SI-STM

The procedure for establishing the tunneling junctions as described in section 2.2.3 can lead to a systematic error called *setup effect*. The tunneling current $I(\mathbf{r}, z, V)$ and differential conductance $g(\mathbf{r}, z, V)$ at tip-sample separation z, at a point $\mathbf{r}$ on 2D sample surface and at a bias voltage V can be written as:

$$\begin{aligned} I(\mathbf{r}, z, V) &= C(\mathbf{r}, z) \int_0^{eV} n(\mathbf{r}, E) dE \\ g(\mathbf{r}, z, V) &= C(\mathbf{r}, z) n(\mathbf{r}, E) \end{aligned} \tag{2.16}$$

where $C(\mathbf{r}, z, V)$ captures the surface corrugation, matrix element and current decay due to tip-sample separation (see eq. (2.9) and (2.12)). As explained in section 2.2.3, spectroscopic imaging requires establishing a tunnel junction at

spectroscopic setup I_S^{spec} and V_S^{spec} at each point (which we will denote in following discussion as just I_S and V_S for brevity) $\mathbf{r}$. Hence we have:

$$\begin{aligned} I_S(\mathbf{r}, z, V_S) &= C(\mathbf{r}, z) \int_0^{eV_S} n(\mathbf{r}, E) dE \\ \implies C(\mathbf{r}, z) &= \frac{I_S(\mathbf{r}, z, V_S)}{\int_0^{eV_S} n(\mathbf{r}, E) dE} \end{aligned} \tag{2.17}$$

Using eq. (2.16)

$$\begin{aligned} I(\mathbf{r}, z, V) &= \frac{I_S(\mathbf{r}, z, V_S)}{\int_0^{eV_S} n(\mathbf{r}, E) dE} \int_0^{eV} n(\mathbf{r}, E) dE \\ g(\mathbf{r}, z, V) &= \frac{I_S(\mathbf{r}, z, V_S)}{\int_0^{eV_S} n(\mathbf{r}, E) dE} n(\mathbf{r}, E) \end{aligned} \tag{2.18}$$

Hence the measured current and differential conductance at $E = eV$ will contain the modulations in density of states at energies $E < V_S$ via the factor $\int_0^{eV_S} n(\mathbf{r}, E) dE$. This imprint will depend on chosen setup voltage V_S. Also note that as eq. (2.16) contains a prefactor $C(\mathbf{r}, z)$ which has an exponential dependence on z and can obscure the study of changes with respect to only energy $E = eV$ which is what we are usually interested in [36]. These effects are collectively known as the *setup effect*. There are multiple ways to counter this effect for specific conditions and requirements [30, 32, 36]. We employ a technique we call *setup correction* to our acquired $g(\mathbf{r}, E) = dI/dV(\mathbf{r}, \mathbf{E})$ images to get rid of the exponential prefactor $C(\mathbf{r}, z)$. We perform a pixelwise division of $g(\mathbf{r}, E_i = eV_i) = dI/dV(\mathbf{r}, E_i = eV_i)$ images at each energy layer $E_i = eV_i$ with the current image recorded at the setup voltage (see section 2.2.3) $I_S(\mathbf{r}, E_s = eV_s)$. This operation yields:

$$\begin{aligned} \frac{I(\mathbf{r}, z, V)}{I_S(\mathbf{r}, z, V_S)} &= \frac{\int_0^{eV} n(\mathbf{r}, E) dE}{\int_0^{eV_S} n(\mathbf{r}, E) dE} \\ \frac{g(\mathbf{r}, z, V)}{I_S(\mathbf{r}, z, V_S)} &= \frac{\int_0^{eV} n(\mathbf{r}, E) dE}{\int_0^{eV_S} n(\mathbf{r}, E) dE} \end{aligned} \tag{2.19}$$

Hence these quantities are now free of exponential pre-factor $C(\mathbf{r}, z)$ and enable study physical phenomena caused by change in density of states with respect to energy. This also has advantage of removal of bit noise. Bit noise is caused because a setup in our software I_S leads to an actual setup current only with the precision of least significant bit (LSB) of the digital to analog converter (DAC) which has a finite number of bits. Hence the setup current I_S at each pixel $\mathbf{r}$ can differ by LSB. This will lead to different tip-sample separation z and exponentially sensitive pre-factor $C(\mathbf{r}, z)$ might lead to random noise at each $\mathbf{r}$. Hence getting rid of $C(\mathbf{r}, z)$ by pixelwise division using the setup-correction helps with bit noise.

2.3 BOREAS: Dilution Fridge SI-STM at Cornell

Performing cryogenic SI-STM is a challenging task as measurements with sub-angstrom spatial and microelectronvolt energy resolutions are to be made with enough signal to noise ratio such that the averaging time for an accurate measurement is small enough so that the dewar does not run out of the cryogen. There are various techniques pioneered in this group which has made this possible. In this section I briefly mention some salient features of SI-STM which enabled the collection of data presented in this thesis. For more details please refer to the Ph.D. thesis of Curry Taylor [37].

2.3.1 STM Head

The STM head is a homemade design detailed in [38]. Figure 2.6 shows different parts of the STM-head. The STM tip is mounted inside a piezo tube which performs the scanning in x-y and provides the fine z-motion while scanning. The piezo tube is held in a sapphire prism with shear piezo stacks which provide coarse z-motion required to move large distances towards or away from the sample during insertion/removal of samples. The piezo stacks use a *slip-stick* motion: they extend(shrink) slowly and static friction keeps them stuck to the sapphire prism and the whole sapphire prism moves up(down). Then they shrink (extend) fast to neutral shape and kinetic friction which is lower than static friction is small enough such that the sapphire prism doesn't stick and move back. Hence a net up (down) displacement is achieved in this fashion. The pressure on sapphire prism against the piezo stacks determines the total frictional force hence the extent of this slip-stick motion or step size. This pressure is controlled by a ruby ball with screws on a Be-Cu plates which presses the prism against the piezo stacks. Hence the step-size can be tuned by using those screws. The body is made of macor which offers high thermal conductivity and is an excellent insulator. It is also a material with high rigidity which makes the resonant frequency of the head very high and discourages the coupling of noise. For measuring the location of the sapphire prism with respect to the macor body, two conducting tubes: one attached to the macor body and the other to the sapphire prism form a cylindrical capacitor and the capacitance is measured using a lock-in amplifier in the balanced condition of an electronic resonance bridge (for more details, please refer to [37]). The sample is glued onto a brass a sample stud using a silver epoxy which maintains good thermal and electrical contact and inserted using an insertion rod from the top of the

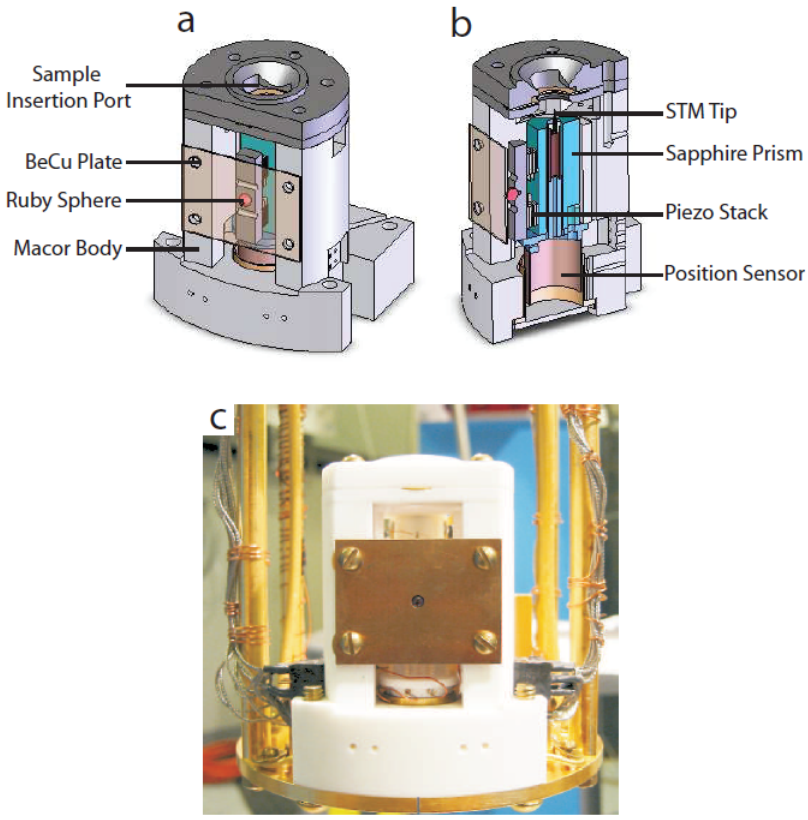

Figure 2.6: STM head. a) Front View b) Sectioned view c) Photograph of STM Head

cryostat. The sample stud is pressed in the STM head with Be-Cu plates which hold it rigidly.

2.3.2 Feedback and Control Electronics

In this section we describe the electronics which are used to control and perform the experiments. Figure 2.7 shows a schematic of our feedback and control electronics. The tip current is passed through a pre-amplifier which amplifies and converts the current into voltage. This is recorded in an electronic control unit (ECU). The ECU is controlled by a computer software (Topometrix) which

allows control over operations and parameters. The topographic scanning is determined by software parameters and corresponding voltages are output by ECU which are applied to the piezo-tube to perform scanning. The z-voltage is determined by PID control with the aim of keeping the tunneling current constant and recorded as the topograph (as described in section 2.2.1). The sample bias is set by software and output by ECU and passed through a D:1 divider (typical D=10). The voltage divider is used for a finer control of bias voltage. For spectroscopy measurements, we connect the Lock-in via a spectra switch. The Lock-In amplifier applies a bias modulation (after passing through a 100:1 voltage divider and the D:1 divider, to get small energy resolution from a Lock-In output of 0-5V), takes the response current as input and performs the dI/dV measurement as described in section 2.2.2 which is finally output to the ECU for recording via the software. All the coaxes going in the cryostat to the STM are equipped with π-filters to filter the ambient electromagnetic radiation which can be a source of noise/heating for ultra-low temperature measurements.

2.3.3 Dilution Fridge

The SI-STM I used for the data collection is aptly named BOREAS, the winged Greek god of Northern winds and winter. It is equipped with a Kelvinox dilution fridge from Oxford Instruments which could go down to 50mK in our experiments. A schematic diagram of a dilution fridge is shown in figure 2.9. The mixture ^{3}He/^{4}He is condensed by 1K pot. The temperature of the mixture needs to be brought down to 860mK where phase separation between lighter concentrated ^{3}He rich phase and heavier dilute ^{3}He poor phase occurs (see figure 2.8). The cooldown up to 860 mK from a temperature of 1.2K at the 1K Pot

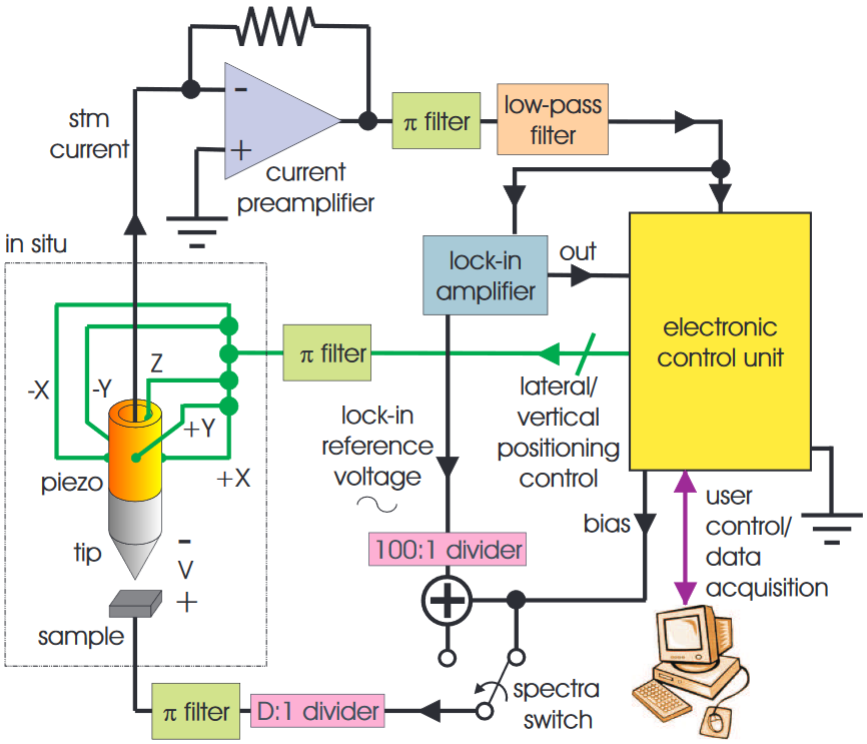

Figure 2.7: STM feedback and control schematic showing various components and interconnections to enable topography and spectroscopy measurements. Figure reproduced from [37]

is achieved by evaporative cooling by pumping on the mixture via still with a powerful circulation-pump (combined with a turbo-pump in some cases). Once the phase separation occurs, since the enthalpy of ^{3}He in concentrated and dilute phases is different, cooling can be obtained by removing ^{3}He from the concentrated phase and sending it to the dilute phase, hence the term *dilution* fridge.

For continuous operation dilution has to occur in a dynamic cycle and ^{3}He must be removed from the dilute phase to prevent over-saturation and returned to the concentrated phase to continue the dilution cycle in a dynamic equilibrium. Still is maintained at a temperature of 600mK to 700mK at which the

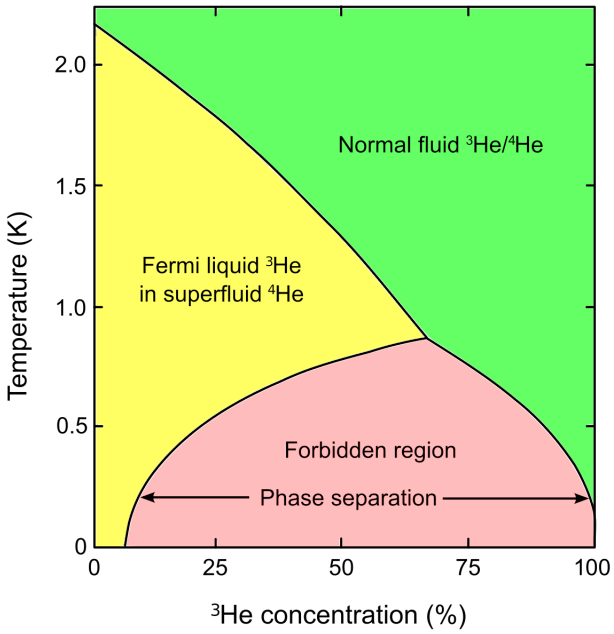

Figure 2.8: Phase diagram of the ^{3}He/^{4}He mixture. The phase separation occurs starting at T=860mK. Figure from dilution refrigerator article Wikipedia under creative commons license.

partial pressure of ^{3}He is 1000 times that of ^{4}He. Hence pumping on still causes ^{3}He to evaporate preferentially leaving the mixture in still more dilute than in mixing chamber, creating an osmotic pressure which pulls ^{3}He from the mixing chamber to the still. The ^{3}He leaving from the mixing chamber is cold and is used to cool down the returning ^{3}He to concentrated phase via a series of heat exchangers. At temperatures above 50mK, conventional coiled heat exchangers work fine. At lower temperatures the Kapitza resistance, the resistance between the liquid and solid walls increases as $1/T^3$ and hence surface contact must be increased as much as possible. This is achieved by sintered silver heat exchangers. The mixture flowing in the cycle is filtered of impurities by freezing them using a liquid nitrogen (oil from pump and other organics) and a liquid helium trap (hydrogen and others) in series. The STM head is mounted on the mixing chamber and all incoming cables are thermalized at various points in the

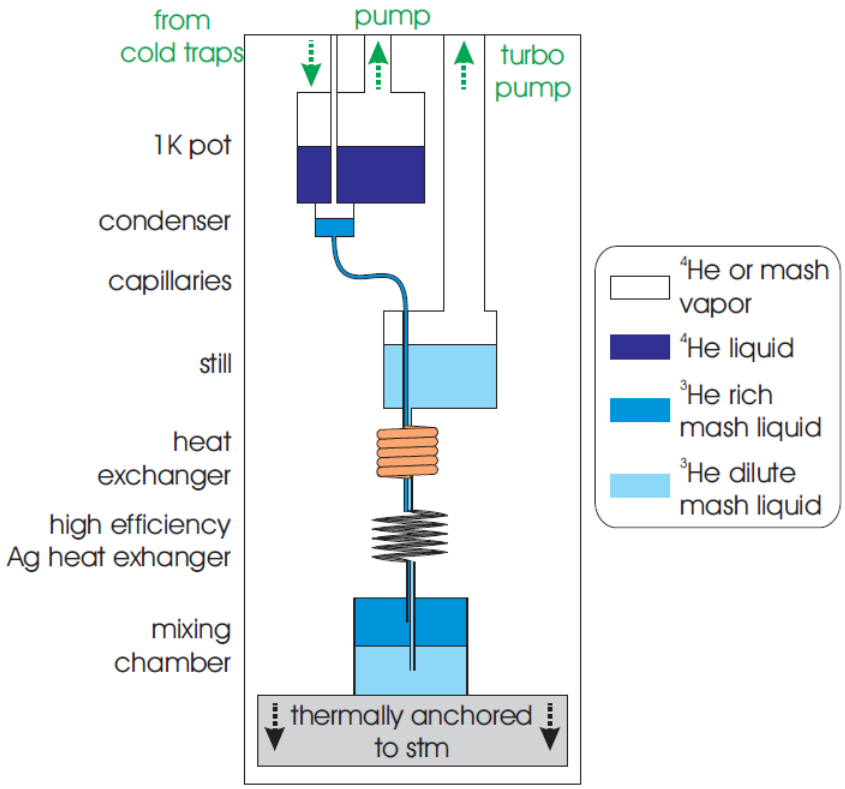

Figure 2.9: Schematic of a dilution refrigerator showing various stages. Notice the phase separated mixture in the mixing chamber where the ^{3}He is removed from lighter ^{3}He rich phase and returned via circulation to the heavier ^{4}He phase, thus producing cooling by dilution. Mash is a slang for ^{3}He/^{4}He mixture. Figure reproduced from [37]

fridge to ensure excellent thermal contact. We have a thermometer mounted at the STM-head to monitor the temperature of the sample, which is thermalized very well due to the choice of BeCu, macor and brass in construction of the STM head and careful thermal anchorization of all the Nb-Ti coaxes used to carry the signal.

2.3.4 Vibration isolation

The tunneling current depends exponentially on the tip-sample distance as shown in eq.(2.12). Hence to perform a complicated technique as spectroscopic imaging, we need to maintain the tip-sample distance as constant as possible to ensure high signal to noise ratio and smaller averaging times, otherwise the cryostat will warm up before one can finish a measurement. The SI-STM at Cornell has a dedicated structure to achieve this as shown in figure 2.10. The key in the design of this architecture is to provide a successive stage of resonant frequencies which are very different and hence minimal noise couples to the STM head eventually. The foundation on which the room rests is separate from the building for vibrational impedance mismatch. There is an acoustic outer room which has sand-filled walls and acoustic padding which absorbs sound. The inner acoustic room is supported on a 30-ton concrete slab (resonant frequency below 1Hz) which is floated on air-springs for measurements. The dewar containing the experiment is mounted on a 1.5-ton table (resonant frequency ~ 1.2 Hz) which is supported by air-springs via three 0.5-ton lead-filled legs. Finally as we mentioned in section 2.3.1, the STM Head has a resonant frequency ~ 3kHz, so this series of vibration isolation structures ensure that almost no vibrations couple the STM head causing a tip-sample distance variations.

2.3.5 RF isolation

For dilution fridge experiments at millikelvin temperatures, RF energy present in ambient due to phone signals and transmission cables etc. usually at high frequencies 100MHz-GHz can cause heating. They also contribute to current

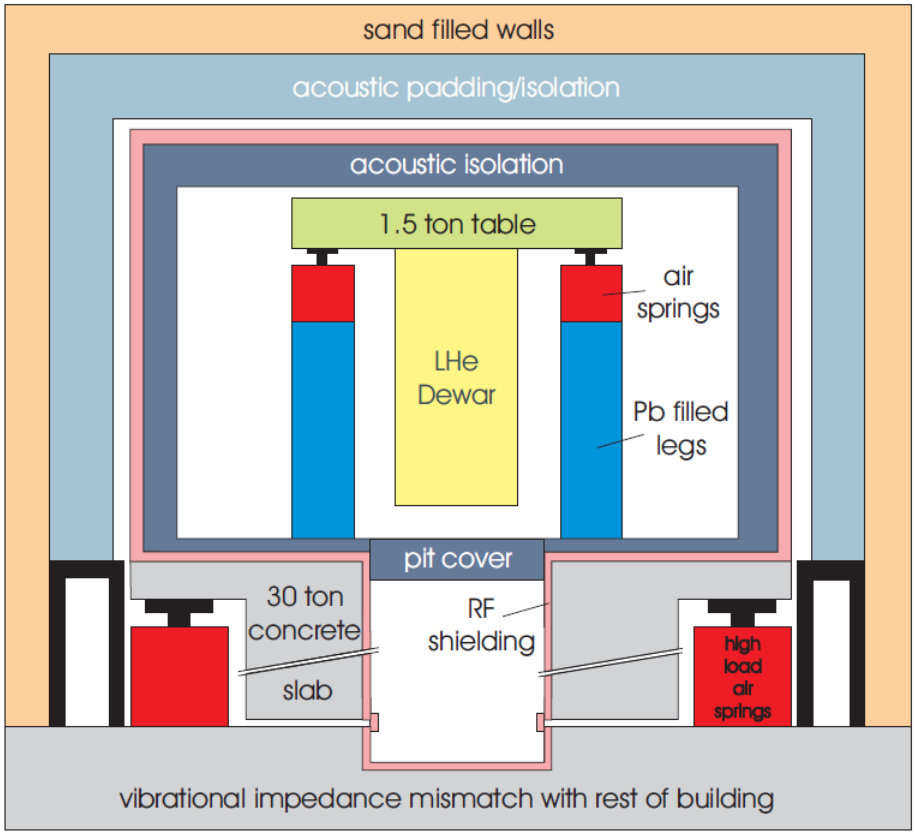

Figure 2.10: Schematic of SI-STM vibration and RF isolated room. Figure is not to scale. Reproduced from [37]

noise by EMF coupling. To isolate this, the inner acoustic room for our experiments is lined with a Cu sheet which creates a Faraday cage, shielding the SI-STM from RF noise. The wall need not be very thick as the penetration depth ($\delta = 1/(\pi\mu\sigma f)$) for Cu at f=100MHz is $\sim 6\mu$m. We employ a 2mm thick Cu sheet around our inner acoustic room as shown in figure 2.10.

CHAPTER 3

ADVANCED QUASIPARTICLE INTERFERENCE TECHNIQUES

It was really awe-inspiring when I first learned about the wave-particle duality and matter waves. One of the most striking moments in my life was to actually see a matter-wave with my own eyes! SI-STM makes this possible and one such image recorded for Sr_2RuO_4 is shown in Fig.3.1.

Before we get into mathematical details, let us have an intuitive idea in colloquial terms. A metal is a sea of electrons. More generally, a solid-state system described by a Hamiltonian $H_0(\mathbf{k})$ has eigenstates: quasiparticles which have wavefunctions $\psi(\mathbf{k}, E)$. Small disorder in potentials due to impurities or crystal defects will cause interference of the quasiparticle waves, creating standing wave modulations in this quasiparticle sea. As we saw in section 2.2.3, SI-STM can reveal local density of states (LDOS) by imaging conductance $g(\mathbf{r}, E) \propto N(\mathbf{r}, E)$ (Chapter 2). As we shall see in this chapter, this provides a direct visualization of these modulations in $N(\mathbf{r}, E)$ (as can be seen strikingly in Fig. 3.1) and provides a wealth of information about the waves $\psi(k)$ and hence about the system Hamiltonian $H_0(k)$ itself.

I start by explaining the fundamentals of QPI. Then I will describe how to calculate quasiparticle interference patterns using a T-matrix formalism. We look at how to do such calculations for Bogoliubov quasiparticles in a superconducting state (also called Bogoliubov quasiparticle interference or BQPI) for both single and multi-band superconductors. We used these techniques in this thesis for comparison to experiments on Sr_2RuO_4 presented in the next chapter.

I will describe a recent advanced analysis technique developed in our

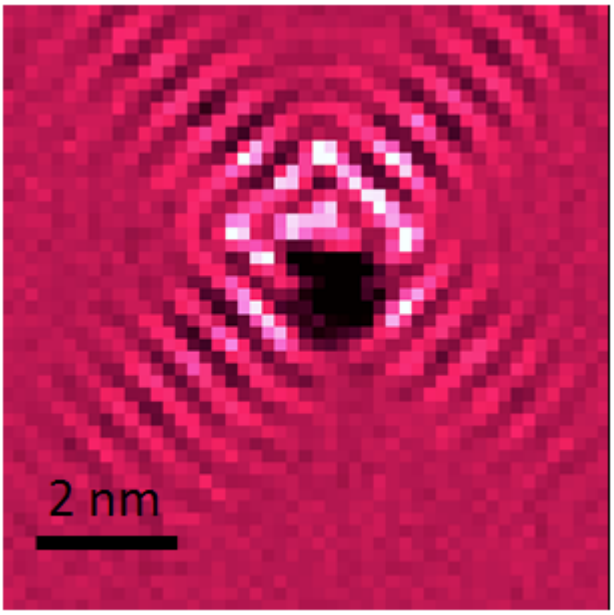

Figure 3.1: QPI pattern for Sr_2RuO_4 at T=2K

group [39] to get the information about the sign of superconducting gap out of the QPI patterns, a technique we dubbed HAEM after the theorists who proposed it [40] (P. J. Hirschfeld, D. Altenfeld, I. Eremin and I. Mazin). For retaining the phase information of a QPI pattern (a wave), one requires the origin of the QPI pattern (the defect) to be centered in the field of view (FOV). In a novel work in this thesis, we have extended this technique to work for multiple defects present in a FOV. I will describe the details of this novel technique here and show its application to LiFeAs in a later chapter.

3.1 Fundamentals of QPI

A periodic potential in a crystal H_0 leads to Bloch eigenstates $\psi_{\mathbf{k}}(\mathbf{r}) = e^{i\mathbf{k}\cdot\mathbf{r}}u_{\mathbf{k}}(\mathbf{r})$ [41]. Where $u_{\mathbf{k}}(\mathbf{r})$ is a periodic function with the period of the potential (crystal lattice). Bloch eigenstates are characterized by well defined quantum numbers,

momentum $\mathbf{k}$ and energy $\epsilon(\mathbf{k})$ given by $H_0\psi_{\mathbf{k}}(\mathbf{r}) = \epsilon(\mathbf{k})\psi_{\mathbf{k}}(\mathbf{r})$. The dispersion $\epsilon(\mathbf{k})$ is the important sought after quantity which characterizes the system and probes like ARPES can measure it directly [42]. SI-STM measures $LDOS(E, \mathbf{r})$, which is given as:

$$LDOS(E, \mathbf{r}) = \sum_n |\Psi_n(\mathbf{r})|^2 \, \delta(E - \epsilon_n) \tag{3.1}$$

where n denotes quantum numbers for eigenstates with energy ϵ_n. Substituting the Bloch wavefunction, one can see that the $\mathbf{k}$ information is lost because the expression involves absolute value squared of the factor $e^{i\mathbf{k}\cdot\mathbf{r}}$. Hence in a perfect crystal, SI-STM will not be able to see any dispersion in the form of a QPI but will only see $|u_{\mathbf{k}}(\mathbf{r})|^2$ which will just be a periodic function.

However, any real material will have disorder in the perfectly periodic potential in the form of missing atoms, impurity atoms etc. This can cause scattering of the Bloch eigenstates (which are no longer true eigenstates), leading to mixing of states with different momenta $\mathbf{k}$ but same energy $\epsilon(\mathbf{k})$ in the case of elastic scattering. This is what gives birth to *quasiparticle interference* or QPI patterns. Consider SI-STM LDOS measurement for a simple case of mixing of two Bloch eigenstates with $\mathbf{k_1}$ and $\mathbf{k_2}$ with the same energy E. From eq. (3.1), we see that we will measure at energy E:

$$\begin{aligned} |\Psi(\mathbf{r})|^2 &= \left| e^{i\mathbf{k}_1\cdot\mathbf{r}} a_1 u_{\mathbf{k}_1}(\mathbf{r}) + e^{i\mathbf{k}_2\cdot\mathbf{r}} a_2 u_{\mathbf{k}_2}(\mathbf{r}) \right|^2 \\ &= \left| a_1 u_{\mathbf{k}_1}(\mathbf{r}) \right|^2 + \left| a_2 u_{\mathbf{k}_2}(\mathbf{r}) \right|^2 + \left(a_1 u_{\mathbf{k}_1}(\mathbf{r}) a_2^* u_{\mathbf{k}_2}^*(\mathbf{r}) e^{i(\mathbf{k}_1 - \mathbf{k}_2)\cdot\mathbf{r}} + c.c \right) \end{aligned} \tag{3.2}$$

Hence we see that we get modulations in LDOS at $\mathbf{q} = \mathbf{k}_1 - \mathbf{k}_2$, which will be observed in the recorded images at a wavelength $\lambda = 2\pi/q$. This is the QPI pattern.

3.2 A Simple QPI Example Study: Determining the Dispersion of The Quasiparticles

The ability to directly image the quasiparticles in a system gives us a wealth of information about the underlying Hamiltonian. One key information is the dispersion relation (the band structure for a conventional metal), the energy-momentum states which the quasiparticles live in. We illustrate how this is done practically using a simple case of a free electron gas, an ideal metal.

Consider the Hamiltonian for a free electron gas:

$$H(\mathbf{k}) = \frac{\hbar^2|\mathbf{k}|^1}{2m^*} \tag{3.3}$$

where m^* denotes the quasiparticle effective mass. The scattering will mix eigenstates of different $\mathbf{k}$. The kinematic constraint $q(E) = \mathbf{k_1} - \mathbf{k_2}$, which is an "'on-shell"' approximation, ensures that the scattering intensity response at these q are distinct from the rest of the q-space. Moreover, for any $E > 0$ such a kinematically constrained q, defines the interior of a constant energy contour (CEC), which in the case of an ideal metal will be given by:

$$4E = \frac{\hbar^2(k_x^2 + k_y^2)}{2m^*} \tag{3.4}$$

If we hold the direction of the scattering $\mathbf{q} = \hat{\mathbf{q}}$ fixed, the on-shell processes are allowed for $0 < |\mathbf{q}| < 2k_F(\hat{\mathbf{q}})$. This is denoted by blue arrows on a CCE in Fig. 3.2. However, it turns out [**?**] that the response is singular at extremal points of this construction. Hence we get a high intensity at $\mathbf{k}(E) - (-\mathbf{k}(E)) = 2\mathbf{k}(E)$ which is denoted by a red arrow on the CCE in Fig. 3.2. [1]

[1] This is a very simplistic interpretation. The type and strength of impurity can strongly affect the magnitude and phase of scattering and cause a non-trivial response in q.

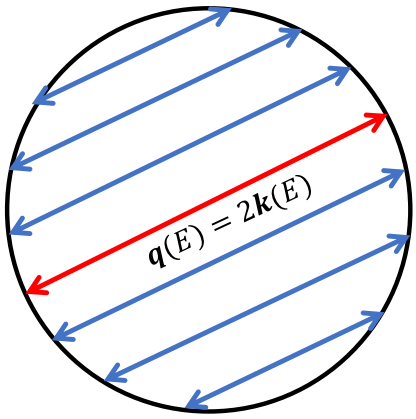

Figure 3.2: QPI wavevectors for a constant energy contour at E for an ideal metal. Blue arrows indicate the allowed wavevectors $\mathbf{q}$. The red arrow indicates the extremal $\mathbf{q}(E) = 2\mathbf{k}(E)$

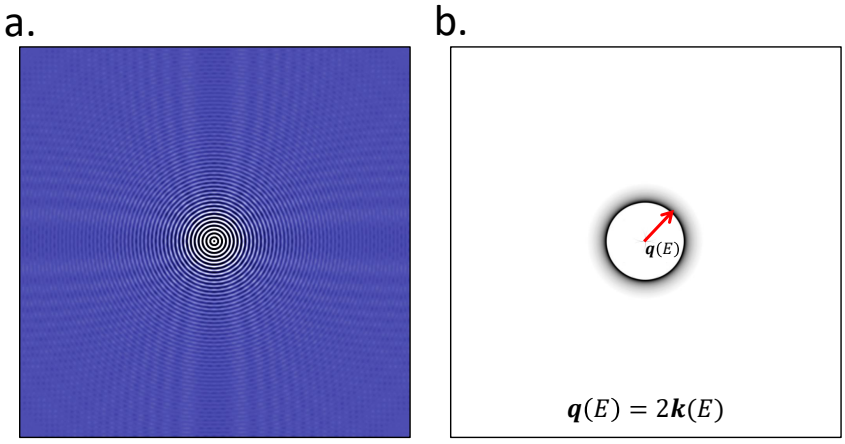

Figure 3.3: Simulated QPI response in an ideal metal. a) The real space QPI in an ideal metal. b) The Fourier transform of the real space BQPI pattern showing the response at $q(E) = k(E) - (-k(E)) = 2k(E)$

Fig. 3.3a shows a simulation (we will discuss how to do a QPI calculation in 3.3) of QPI in real space for an ideal metal with a single impurity in the center of the FOV. The Fourier transform as shown in Fig. 3.3b shows that the response is singular at $\mathbf{q}(E) = 2\mathbf{k}(E)$. From these constraints on the intensity of QPI, we can figure out the dispersion of quasiparticles. Fig. 3.4 shows this procedure.

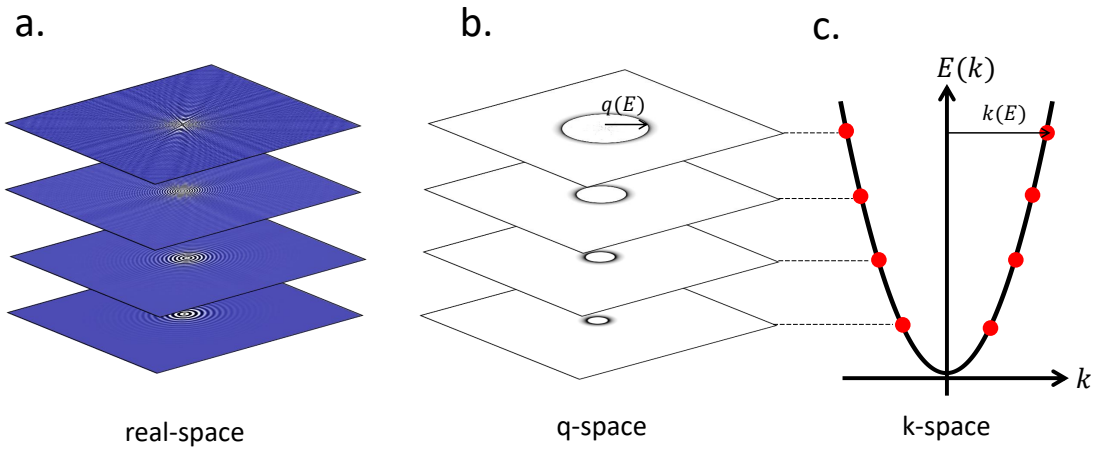

Figure 3.4: Extracting the dispersion of quasiparticles using QPI. a) The real-space $g(\mathbf{r}, E)$ measured with SI-STM.(For demonstration here, we show simulations for an ideal metal.) b) The Fourier transform of the real space images revealing wavevectors $\mathbf{q}(E)$ at each E. c) $\mathbf{k}(E)$ inferred from set of images in b). Here for an ideal metal, $\mathbf{k}(E) = \mathbf{q}(E)/2$, but c) is evidently not to scale but zoomed to show the parabolic dispersion for demonstration purposes.

We first image the QPI by recording $g(\mathbf{r}, E)$ using the procedure described in the section. 2.2.3 at the desired energies. This leads to the real-space images (simulated here using methods described in section 3.3 for a single impurity in the center of a FOV.) shown in Fig. 3.4a. Then we take the Fourier transform of all the images which shows the q-vectors $\mathbf{q}(E)$ present in the QPI pattern at each energy E as shown in Fig. 3.4b. From this information, the $\mathbf{k}$ can be inferred at each energy wherever possible. For the case of an ideal metal, as we discussed and as shown in Fig. 3.3, $\mathbf{q}(E) = 2\mathbf{k}(E)$. Hence $\mathbf{k}(E) = \mathbf{q}(E)/2$. This relationship can be used to construct the band dispersion, as shown for the case of ideal metal in Fig. 3.4c. (Note that the Dif. 3.4c is not to scale, but zoomed to show the parabolic dispersion clearly.)

This is a very powerful tool to determine quasiparticle dispersion in a variety of important condensed matter systems to reveal the physics of the underlying Hamiltonian [32, 31]. Some notable examples are topological insulators [43], Kondo systems [44], cuprate superconductors [45], iron-based Superconductors [46, 39], heavy-fermion superconductors [47], candidate topological superconductors [48]. ARPES also reveals this information in a more direct way by measuring the momenta $\mathbf{k}(E)$ of photoexcited electrons directly [42] (as opposed to SI-STM which reveals $\mathbf{q}(E)$ and getting to $\mathbf{k}(E)$ from $\mathbf{q}(E)$ is a matter of solving a puzzle and it might get complicated for certain systems.). However, the STM has the advantage that it can reach really low temperature of operation (this thesis reports QPI at 90mK for Bogoliubov quasiparticles in Sr_2RuO_4 in Ch. 4) which leads to a much higher energy resolution going as high as microelectronvolts (as compared to millielectronvolts for an ARPES operating at few K. This limitation in temperature occurs because ARPES needs an optical access to the sample to excite the electrons.). Also, ARPES can measure the dispersion only below the Fermi level, as it needs to excite the electrons in the sample from the filled states. However, since tunneling can occur into the empty states as well as out of the filled states, SI-STM can measure the dispersion both below and above the Fermi level.

3.3 T-matrix Formalism for Calculating QPI

In this section, we describe how to calculate the scattering pattern resulting from QPI. Let us consider a tight binding Hamiltonian in the real-space

$$H_0(\mathbf{k}) = \sum_{\alpha,\beta,\mathbf{k}} \epsilon_{\alpha\beta,\mathbf{k}} c^{\dagger}_{\alpha\mathbf{k}} c_{\beta\mathbf{k}} \tag{3.5}$$

where α, β denote the orbitals. The Green's function for this unperturbed system, also called the bare Green's function can be written as

$$G_0(\mathbf{k}, E) = (E + i\delta - H_0(\mathbf{k}))^{-1} \tag{3.6}$$

where δ is the energy broadening parameter inherent in any real probe. In SI-STM, we take it to be energy resolution/bias modulation (see sec. 2.2.3).

Now let us consider elastic scattering due to an impurity potential. The impurity potential interacts via Coulomb potential to the rest of the electronic states in the system. For good metals, the Coulomb interaction is screened at a length scale of the order of lattice spacing, hence impurity potential is usually taken to be localized in space and represented by a delta function such as $U(\mathbf{r}) = U_0\delta(\mathbf{r} - \mathbf{r_0})$ for an impurity located at $\mathbf{r_0}$ [49]. Since the impurity potential breaks translational symmetry, in momentum space, $U_{\mathbf{kk'}}$ mixes two different momentum eigenstates $\mathbf{k}$ and $\mathbf{k'}$ by scattering one eigenstate into another at the same energy. Multiple scatterings from this impurity can be taken into account exactly using a T-matrix which is best explained by a Feynman diagram [49] as shown in Fig. 3.5:

From the Feynman diagram 3.5, we can write the full Green's function for the system including the scattering process in terms of the bare Green's functions using T-matrix T as:

$$\begin{aligned} G(\mathbf{k}, \mathbf{k}', E) &= G_0(\mathbf{k}, E) + G_0(\mathbf{k}, E)U_{\mathbf{k},\mathbf{k}'}G_0(\mathbf{k}') + \sum_{k''} G_0(\mathbf{k}, E)U_{\mathbf{k},\mathbf{k}''}G_0(\mathbf{k}'')U_{\mathbf{k}'',\mathbf{k}'}G_0(\mathbf{k}') + \dots \\ &= G_0(\mathbf{k}, E) + G_0(\mathbf{k}, E)T(\mathbf{k}, \mathbf{k}', E)G_0(\mathbf{k}', E) \end{aligned} \tag{3.7}$$

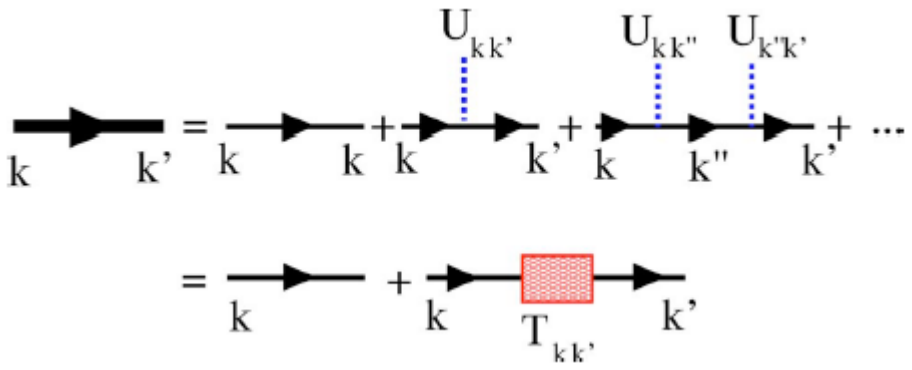

Figure 3.5: Feynman diagram for T-matrix treatment of the QPI process. The thick line represents the full Green's function while the thin lines represent the bare Green's function. The dashed lines represent the scattering process. Figure reproduced from [49]

Where by definition, T-matrix is given by an infinite series

$$\begin{aligned} T(\mathbf{k},\mathbf{k}',E) &= U_{\mathbf{k}\mathbf{k}'} + \sum_{\mathbf{k}''} U_{\mathbf{k}\mathbf{k}''} G_0(\mathbf{k}'',E) U_{\mathbf{k}''\mathbf{k}'} \\ &= U_{\mathbf{k}\mathbf{k}'} + \sum_{\mathbf{k}''} U_{\mathbf{k}\mathbf{k}''} G_0(\mathbf{k}'',E) T(\mathbf{k}'',\mathbf{k}',E) \end{aligned} \tag{3.8}$$

Imagine a scattering process at a given difference wavevector $\mathbf{k}' - \mathbf{k} = \mathbf{q}$. The number of particles per unit energy, the density of states is given as:

$$\begin{aligned} \delta N(\mathbf{q},E) &= -\frac{1}{\pi}\mathrm{Im} \sum_{\mathbf{k}} G(\mathbf{k},\mathbf{k}+\mathbf{q},E) \\ &= -\frac{1}{\pi}\mathrm{Im} \sum_{\mathbf{k}} G(\mathbf{k},E) - \frac{1}{\pi}\mathrm{Im} \sum_{\mathbf{k}} G_0(\mathbf{k},E) T(\mathbf{k},\mathbf{k}+\mathbf{q},E) G_0(\mathbf{k}+\mathbf{q},E) \\ &= N_0 + \delta N(\mathbf{q},E) \end{aligned} \tag{3.9}$$

where $-\frac{1}{\pi}\mathrm{Im} \sum_{\mathbf{k}} G_0(\mathbf{k}) = N_0$ is the unperturbed density of states. Thus the modulation in the density of states, the QPI pattern in q-space is given as:

$$\delta N(\mathbf{q},E) = -\frac{1}{\pi}\mathrm{Im} \sum_{\mathbf{k}} G_0(\mathbf{k},E) T(\mathbf{k},\mathbf{k}+\mathbf{q},E) G_0(\mathbf{k}+\mathbf{q},E) \tag{3.10}$$

Since energy is conserved in elastic scattering, only the directions of the momenta of eigenstates are changed by the scattering. If scattering is considered isotropic, then the k-dependence of potential is lost as $U_{\mathbf{k}\mathbf{k}'} = U$ which leads to a much-simplified expression for the T-matrix in a closed form in terms of potential U and bare Green's function G as:

$$\begin{aligned} T(E) &= U + U \sum_{\mathbf{k}} G_0(\mathbf{k}, E) T(E) \\ T(E) - U \sum_{\mathbf{k}} G_0(\mathbf{k}, E) T(E) &= U \\ (I - U \sum_{\mathbf{k}} G_0(\mathbf{k}, E)) T(E) &= U \\ T(E) &= \left(I - U \sum_{\mathbf{k}} G_0(\mathbf{k}, E) \right)^{-1} U \end{aligned} \tag{3.11}$$

3.4 Calculating Bogoliubov QPI

As discussed in section 3.1, QPI pattern results from elastic scattering from the defects and encodes the k-space structure of the states at a given energy. Hence k-space structure of constant contours of energy or CCEs can be inferred from QPI experiments. In a superconductor, we are interested in the momentum-space structure of the superconducting gap $\Delta(\mathbf{k})$. The canonical excitations in a superconducting ground state are Bogoliubov quasiparticles as mentioned in section 1.1.3. CCEs for Bogoliubov quasiparticles follow the dispersion relation:

$$E(\mathbf{k}) = \sqrt{\epsilon(\mathbf{k})^2 + \Delta(\mathbf{k})^2} \tag{3.12}$$

where $\epsilon(\mathbf{k})$ is the normal state dispersion.

Therefore, the CCEs for Bogoliubov quasiparticles encode the k-space structure of superconducting gap $\Delta(\mathbf{k})$ which can be revealed by Bogoliubov quasi-

particle interference (BQPI).

In a spinor basis $(c^{\dagger}_{\mathbf{k}\uparrow}, c_{-\mathbf{k}\downarrow})$ The Bogoliubov de Gennes Hamiltonian is given by (section 1.1):

$$H_{\mathrm{BdG}}(\mathbf{k}) = \begin{pmatrix} \epsilon(\mathbf{k}) & \Delta(\mathbf{k}) \\ \Delta^{*}(\mathbf{k}) & -\epsilon(\mathbf{k}) \end{pmatrix} \tag{3.13}$$

Where $\epsilon(\mathbf{k}) = \sum_{\mathbf{k}\sigma} t c^{\dagger}_{k\sigma}, c_{k\sigma}$ is the normal state dispersion (usually in tight binding parametrization) and $\Delta(\mathbf{k})$ is the superconducting gap.

The Green's function is given as:

$$G_0(\mathbf{k}, E) = (E + i\delta - H_{\mathrm{BdG}}(\mathbf{k}))^{-1} \tag{3.14}$$

where we take the energy broadening parameter to be the thermal energy resolution $3.5k_BT$ or bias modulation for SI-STM experiments (see section 2.2.3). Bare Green's functions can be used to calculate the spectral density function $A_0(\mathbf{k}, E)$, which is useful to visualize how the local density of states of quasiparticles is affected by the superconducting gap (though it should be kept in mind that they are not CCEs). $A_0(\mathbf{k}, E)$ is given as:

$$A_0(\mathbf{k}, E) = -\frac{1}{\pi}\mathrm{Im}G_0(\mathbf{k}, E) \tag{3.15}$$

The leftmost column of Fig. 3.6 shows the $A_0(\mathbf{k}, E)$ calculated for $Bi_2Sr_2CaCu_2O_{8+\delta}$ for multiple subgap energies. It can be seen how a $d_{x^2-y^2}$-wave gap of the form $\Delta(\mathbf{k}, E) = \Delta(\cos k_x - \cos k_y)$ with nodes along $[1, 1]$ leaves quasiparticles along [1,1] as we go inside the gap and gaps out the other states.

We perform the Fourier transform to get Green's functions in real-space as

they are useful in saving computations as we shall see.

$$\mathcal{F}G_0(\mathbf{k}, E) = \mathcal{G}_0(\mathbf{r}, E) \tag{3.16}$$

where $\mathcal{F}$ denotes the Fourier transform.

We assume isotropic scattering and hence the T-matrix is momentum-independent and is given using (3.11) as:

$$T(E) = \left(I - U_s \sum_{\mathbf{k}} G_0(\mathbf{k}, E) \right)^{-1} U_s \tag{3.17}$$

where U_s is the scattering potential strength, we choose it to be usually t, the tight binding parameter. This expression for T-matrix can be simplified in terms of the real-space Green's function because $\sum_{\mathbf{k}} G_0(\mathbf{k}, E) = \mathcal{G}_0(0, E)$. Thus

$$T(E) = (I - U_s \mathcal{G}_0(0, E), E))^{-1} U_s \tag{3.18}$$

Finally, the perturbation in the density of states can be calculated using eq. (3.10) as:

$$\delta N(\mathbf{q}, E) = -\mathrm{Im} \left[\sum_{\mathbf{k}} G_0(\mathbf{k}, E) T(E) G_0(\mathbf{k} + \mathbf{q}, E) \right]_{11} \tag{3.19}$$

Where $[\dots]_{ij}$ denotes the spinor index for the basis used in BdG Hamiltonian. We are, hereby counting only one spin, but the other spin is trivially related as the number of spin-up and spin-down species will be equal in the absence of magnetic scattering.

Let us try to write the expression in eq. (3.19) as a convolution.

$$\begin{aligned} \delta N(\mathbf{q}, E) &= -\mathrm{Im} \sum_{\mathbf{k}} G_0(\mathbf{k}, E) T(E) G_0(\mathbf{q} + \mathbf{k}, E) \\ &= -\mathrm{Im}\, T(E) \sum_{\mathbf{k}} G_0(\mathbf{k}, E) G_0(\mathbf{q} - (-\mathbf{k}), E) \end{aligned} \tag{3.20}$$

The sum is over whole of k-space. Hence the summing variable $\mathbf{k}$ can be replaced by $-\mathbf{k}$. Also, let us define $G_1(\mathbf{k}) = G_0(-\mathbf{k})$. Then, in terms of $\kappa = -\mathbf{k}$, $d\mathbf{k} = d\kappa$ and $G_0(\mathbf{k}) = G_1(\kappa)$. The expression for δN then clearly can be written as a convolution using these definitions as:

$$\delta N(\mathbf{q}) = -\mathrm{Im}\left[\sum_{\kappa} G_1(\kappa, E)T(E)G_0(\mathbf{q}-\kappa, E)\right]_{11} \tag{3.21}$$

Now we can use convolution theorem of Fourier Transforms:

$$\mathcal{F}[f * g] = \mathcal{F}[f] \cdot \mathcal{F}[g] \tag{3.22}$$

Hence we can express the convolution in k-space in eq. (3.21) with their Fourier transforms counterparts using the convolution theorem mentioned in eq. (3.22) to get $\delta N(\mathbf{r})$ as:

$$\begin{aligned} \delta N(\mathbf{r}, E) &= -\mathrm{Im}\ \left[T(E)\mathcal{G}_1(\mathbf{r}) \cdot \mathcal{G}_0(\mathbf{r})\right]_{11} \\ &= -\mathrm{Im}\ \left[T(E)\mathcal{G}_0(-\mathbf{r}) \cdot \mathcal{G}_0(\mathbf{r})\right]_{11} \end{aligned} \tag{3.23}$$

where $\mathcal{G}$ denotes the real-space Fourier counterparts of momentum-space G_0 and $\cdot$ denotes element-wise multiplication (as opposed to matrix product). Using this expression, we can get $\delta N(\mathbf{r}, E)$ and performing a Fourier transform, we can get $\delta N(\mathbf{k}, E)$.

The middle column of Fig. 3.6 shows the real-space BQPI pattern $\delta N(\mathbf{r}, E)$ calculated for $Bi_2Sr_2CaCu_2O_{8+\delta}$ for multiple subgap energies. The rightmost column shows the Fourier Transform of these images, the $\delta N(\mathbf{q}, E)$, which was originally calculated by Wang and Lee [50] to show that the experimental scattering pattern visualized by Hoffman et.al [45] in a pioneering first of its kind experiment, indeed comes from BQPI.

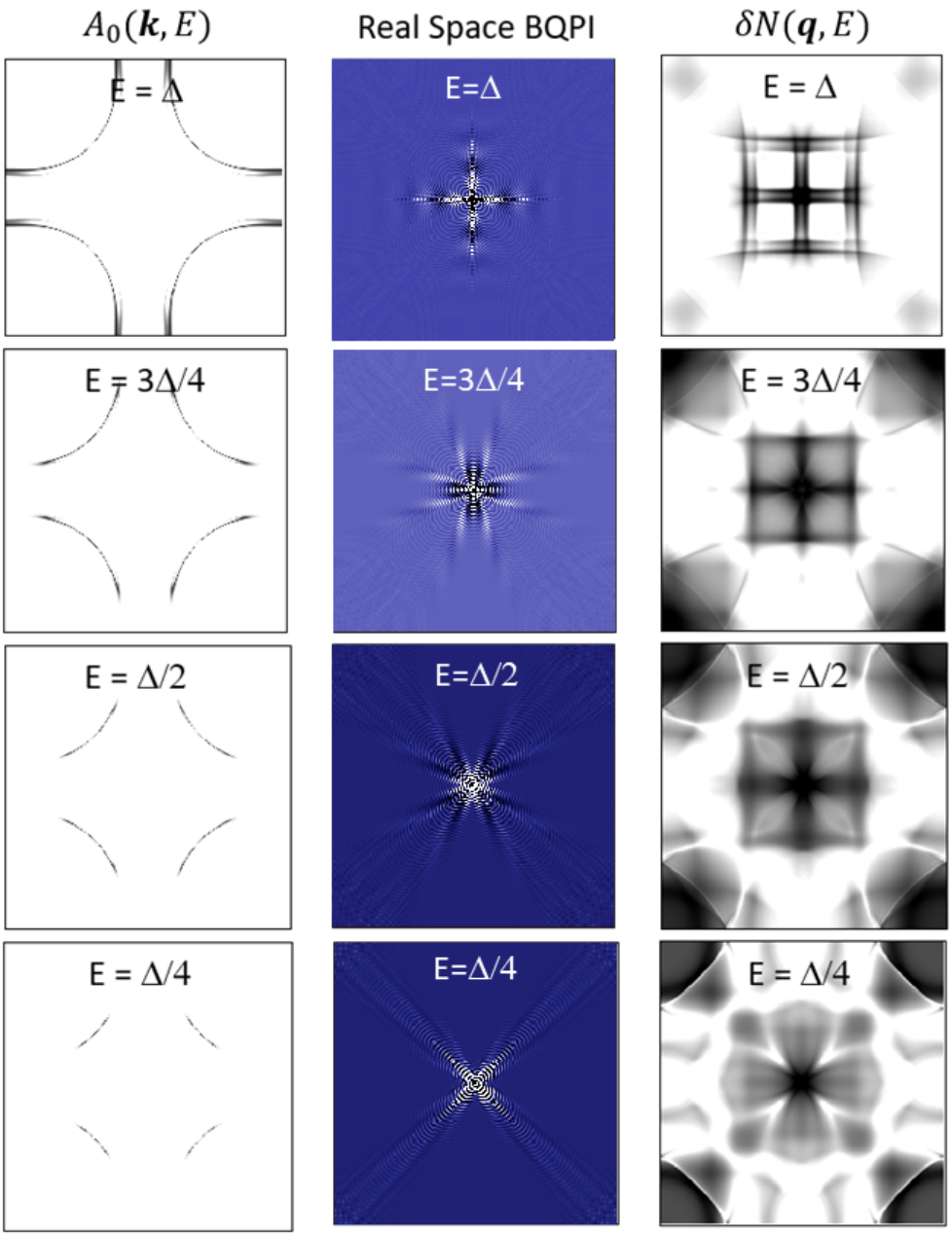

Figure 3.6: Example of T-matrix calculations of BQPI in $Bi_2Sr_2CaCu_2O_{8+\delta}$. Left column shows $A_0(\mathbf{k}, E)$ calculated using eq. (3.15). As we cautioned, it is not exactly the constant contours of energy, but it is good indication to see how electron bands are gapped as we move within the superconducting gap. Middle column shows the real-space BQPI pattern $\delta N(\mathbf{r}, E)$ in local density of states (LDOS). The right column shows $\delta N(\mathbf{q}, E)$, the Fourier transform of BQPI $\delta N(\mathbf{r}, E)$ which helps us visualize the subgap momentum-space structure [45, 50]

3.4.1 Calculating Multi Band BQPI

The main subject of this thesis, Sr_2RuO_4 is a multiband system. In this section we discuss how to deal with a multiband system. For multiband systems, apart from usual intraband scattering, interband scattering also needs to be taken into account. We will present a two-band model for bands x and y. For more bands, a similar approach can be followed. We first choose a spinor basis for writing down the BdG Hamiltonian: $\psi^\dagger = (c^\dagger_{x,\mathbf{k}\uparrow}, c_{x,-\mathbf{k}\downarrow}, c^\dagger_{y,\mathbf{k}\uparrow}, c_{y,-\mathbf{k}\downarrow})$ we get a Bogoliubov de Gennes Hamiltonian $\sum_{\mathbf{k}} \psi^\dagger(\mathbf{k})\hat{H}(\mathbf{k})\psi(\mathbf{k})$ where:

$$\hat{H}(\mathbf{k}) = \begin{pmatrix} \epsilon_x(\mathbf{k}) & \Delta_x(\mathbf{k}) & \epsilon^h_{xy}(\mathbf{k}) & 0 \\ \Delta^*_x(\mathbf{k}) & -\epsilon_x(\mathbf{k}) & 0 & -\epsilon^h_{xy}(\mathbf{k}) \\ \epsilon^h_{xy}(\mathbf{k}) & 0 & \epsilon_y(\mathbf{k}) & \Delta_y(\mathbf{k}) \\ 0 & -\epsilon^h_{xy}(\mathbf{k}) & \Delta^*_y(\mathbf{k}) & -\epsilon_y(\mathbf{k}) \end{pmatrix} \tag{3.24}$$

where ϵ_x, ϵ_y are the normal state dispersion of x and y, ϵ^h_{xy} is the hybridization term between x and y and Δ_x, Δ_y are the gap functions for bands x and y.

The overall scattering potential, taking both the interband and the intraband scattering into account can be expressed in the same basis as:

$$\begin{aligned} U_s &= \begin{pmatrix} U_{intra} & 0 & U_{inter} & 0 \\ 0 & -U_{intra} & 0 & -U_{inter} \\ U_{inter} & 0 & U_{intra} & 0 \\ 0 & -U_{inter} & 0 & -U_{intra} \end{pmatrix} \\ &= (U_{intra} I + U_{inter}\sigma_x) \otimes \sigma_z \end{aligned} \tag{3.25}$$

With this U, the T-matrix for all scattering processes is given as:

$$T(E) = \left(I - \sum_{\mathbf{k}} G_0(\mathbf{k}, E) U_s \right)^{-1} U_s \tag{3.26}$$

Finally the change in the density of states is given as:

$$\delta N(\mathbf{q}) = -\mathrm{Im} \sum_{i=1,3} \left[\sum_{\mathbf{k}} G_0(\mathbf{k}+\mathbf{q}, E) T(E) G_0(\mathbf{k}, E) \right]_{ii} \tag{3.27}$$

Where, we are summing over Bogoliubons (Bogoliubov quasiparticles) spin indices 1, for x band and 3 for y band for a single spin species, as explained in the previous section. Similar to the previous section, for practical ease we Fourier Transform the k-space Green's functions to r-space. And the simplified final expression becomes:

$$\delta N(\mathbf{q}, E) = -\mathrm{Im} \sum_{i=1,3} [T(E) \mathcal{G}_0(-\mathbf{r}) \cdot \mathcal{G}_0(\mathbf{r})]_{ii} \tag{3.28}$$

For examples of such calculations, please see our work on Sr_2RuO_4 in chapter4 of this thesis.

3.5 HAEM Scheme for Phase Information

As we saw in previous sections, Bogoliubov quasiparticle interference encodes the information about $\Delta(\mathbf{k})$. While there are many techniques to measure $|\Delta(\mathbf{k})|$, there are few techniques for measuring the phase of the superconducting gap

$\Delta(\mathbf{k})$. P. J. Hirschfeld, D. Altenfeld, I. Eremin and I. Mazin (HAEM) proposed a scheme [40] where the sign of superconducting gap can be determined with the help of BQPI. Let us consider the scattering of Bogoliubov quasiparticles between two bands μ and ν. The BQPI scattering intensity is given by eq. (3.27) :

$$\begin{aligned}\delta N(\mathbf{q}, E) &= -\mathrm{Im} \sum_{\alpha=\mu,\nu} \left[\sum_{\mathbf{k}} G_0(\mathbf{k}+\mathbf{q}, E) T(E) G_0(\mathbf{k}, E) \right]_{\alpha\alpha} \\ &= -\mathrm{Im} \sum_{\mathbf{k},\mu,\nu} G_0^{\mu}(\mathbf{k}+\mathbf{q}, E) T^{\mu\nu}(E) G_0^{\nu}(\mathbf{k}, E) \\ &= -\frac{1}{2}\mathrm{Im} \sum_{\mathbf{k},\mu,\nu} \mathrm{Tr}(\tau_0+\tau_3) G_0^{\mu}(\mathbf{k}+\mathbf{q}, E) T^{\mu\nu}(E) G_0^{\nu}(\mathbf{k}, E)\end{aligned} \tag{3.29}$$

Where Pauli matrices τ_i represent Nambu space. As in our BQPI calculations, we take the T-matrix to be independent of momentum(assuming point-like potential scatterer). This allows us to take it outside the summation and use the approximate expression for integrated Green's function [40] for an ideal free 2D electron gas (ideal metal) having a flat DOS near Fermi level.

$$\sum_{\mathbf{k}} G_0^{\nu}(\mathbf{k}, \omega) \simeq i\pi\rho_{\nu} \frac{\omega\tau_0 + \Delta_{\nu}\tau_1}{\sqrt{\omega^2 - \Delta_{\nu}^2}} \tag{3.30}$$

Under Born approximation for weak scatterers, the T-matrix can have constant components in different Nambu channels, depending on the scattering mechanism. Magnetic scattering is in the τ_1 channel, where spins are required to be flipped; while non-magnetic spin preserving potential scattering is in τ_3 channel. Since we will be considering non-magnetic potential scattering only, we take the T-matrix to be $T = t_3\tau_3$. Using these simplifications and the integrated Green's function in eq. (3.30), the interband scattering between the bands

μ and ν can be written as:

$$\begin{aligned}\delta N_{\text{inter}}(\omega) &\simeq -2\pi^2 t_3 \rho_\mu \rho_\nu \text{Im}\ \frac{\text{Tr}(\tau_0+\tau_3)(\omega\tau_0+\Delta_\mu\tau_1)\tau_3(\omega\tau_0+\Delta_\nu\tau_1)}{\sqrt{\omega^2-\Delta_\mu^2}\sqrt{\omega^2-\Delta_\nu^2}} \\ &= -2\pi^2 t_3 \rho_\mu \rho_\nu \text{Im}\ \frac{\omega^2-\Delta_\mu\Delta_\nu}{\sqrt{\omega^2-\Delta_\mu^2}\sqrt{\omega^2-\Delta_\nu^2}}\end{aligned} \tag{3.31}$$

Where we don't have the $\mathbf{q}$-dependence as we sum the δN around $\mathbf{q} = \mathbf{q_0}$ where $\mathbf{q_0}$ is the scattering vector where the in-gap scattering between the bands μ and ν occurs in q-space in BQPI.

From this expression, it can now clearly be seen that the imaginary part will be non zero for energies between the two gaps Δ_μ and Δ_ν. For analysis of this expression analytically, limit $\Delta_\mu \to \Delta_\nu$ helps. Under this limit

$$\delta N_{\text{inter}}(\omega) = \begin{cases} -2\pi^2 t_3 \rho_\mu \rho_\nu \delta(\omega - |\Delta_\mu|) & \text{for sgn } \Delta_\mu\Delta_\nu < 0 \\ 0 & \text{for sgn } \Delta_\mu\Delta_\nu > 0 \end{cases} \tag{3.32}$$

Hence, this establishes a quantity which is clearly different depending upon whether the sign of the gap on the two bands are the same or opposite. In reality, without all out simplifying assumptions, we look at the particle hole symmetric BQPI which we define as:

$$\rho^-(E) = \text{Re}\ \delta N(E) - \text{Re}\ \delta N(-E) \tag{3.33}$$

The realistic calculations not in the limits mentioned in our derivation of expression, do not actually lead to $\rho^-(E)$ being singular for sgn$\Delta_\mu\Delta_\nu < 0$ like delta function but it peaks at $\omega \approx \Delta_\mu, \Delta_\nu$ and does not change sign between them. Similarly deviating from the analytical expression in realistic case, $\rho^-(E)$ is not exactly 0 for sgn$\Delta_\mu\Delta_\nu > 0$ for all energies, but now has a significantly smaller peaks at $\omega \approx \Delta_\mu, \Delta_\nu$ than the case with sgn$\Delta_\mu\Delta_\nu < 0$ and changes sign between them. Hence measurement of $\rho^-(E)$ in the region around $\mathbf{q} = \mathbf{q_0}$ for interband

scattering between two pockets, can tell us whether the sign of superconducting gap is the same on both of them or does the sign change from one pocket to another.

3.5.1 Applied HAEM For Single Impurities

This idea was applied for the first time in our group by Sprau et al. [39] on FeSe to determine that the superconducting gap changed sign between electron and hole bands and establish that the gap symmetry is $s_{\pm}$ in FeSe. In this section below, we briefly mention how this technique was applied practically on real data. This also serves as a motivation as to why the improvement we propose for this technique is important.

FeSe is an iron-based superconductor with a lattice shown in Fig. 3.7a. Se atoms are either above Fe plane or below Fe plane, forming a square lattice. The Fermi surface can be represented in so-called 1Fe or 2Fe-zone, represented by dashed and solid lines in Fig. 3.7b. It consists of a hole pocket α around Γ-point and electron pockets ϵ/δ around X/Y points.

Sprau et al. analyzed the scattering between the α and ϵ pockets [39]. This scattering vector is shown in Fig. 3.8a labeled as p_1. G_1 and G_2 denote the Bragg scattering vector. Since HAEM is a phase-sensitive technique, the interference pattern in BQPI needed to be recorded for a single impurity which is centered in the FOV as shown in Fig. 3.8b. This was a key part of realizing the HAEM scheme. The $\rho^{-}(E)$ calculated from BQPI for the single atomic defect from FeSe is shown in Fig. 3.8c, where the feature for scattering which was under study (Fig. 3.8) is circled. The $\rho^{-}(E)$ calculated from $\rho^{-}(\mathbf{q}, E)$ summed over the circle

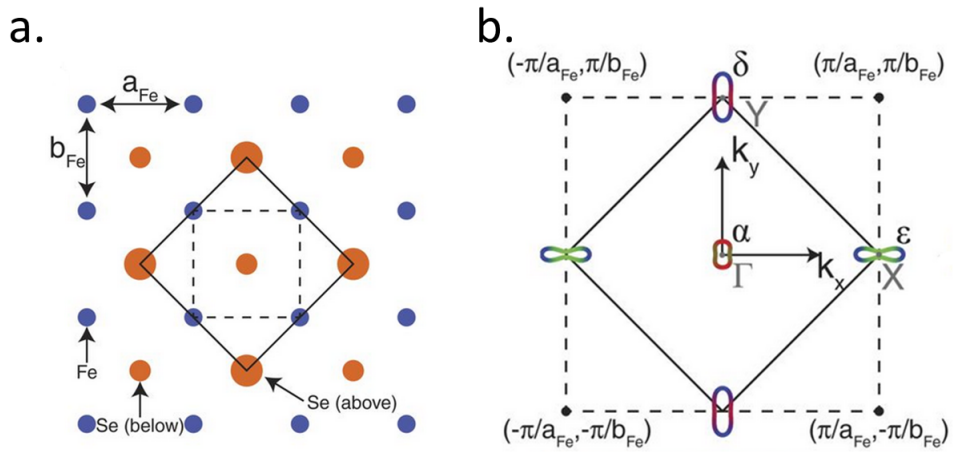

Figure 3.7: FeSe lattice and Fermi Surface. a) shows the lattice structure of FeSe with 2-Fe unit cell shown with solid lines and 1-Fe unit cell shown with dashed lines. b) shows the Fermi surface with hole pocket α around Γ-point and electron pockets ϵ/δ around X/Y points. Figures reproduced from [39]

shown in Fig. 3.8c in Fig. 3.8 as black data points. As mentioned in the previous section outlining the scheme, $\rho^{-}(E)$ does not change sign and peaks within the gap values. The theoretical calculations were performed for both sign-changing $s_{\pm}$ and sign-preserving (s_{++}) gaps and the curves are overlaid on the data and it can be seen that sign-preserving $\rho^{-}(E)$ is much smaller than sign-changing $\rho^{-}(E)$ as expected with $s_{\pm}$ case tracking the data much closely. This established that FeSe has s_{pm} gap symmetry [39], which was the first use of HAEM scheme for gap sign determination.

3.5.2 HAEM Scheme for Multiple Atom

Centering the FOV to a single atomic defect was key to realize the HAEM scheme as a phase-sensitive technique. However this also imposes certain limi-

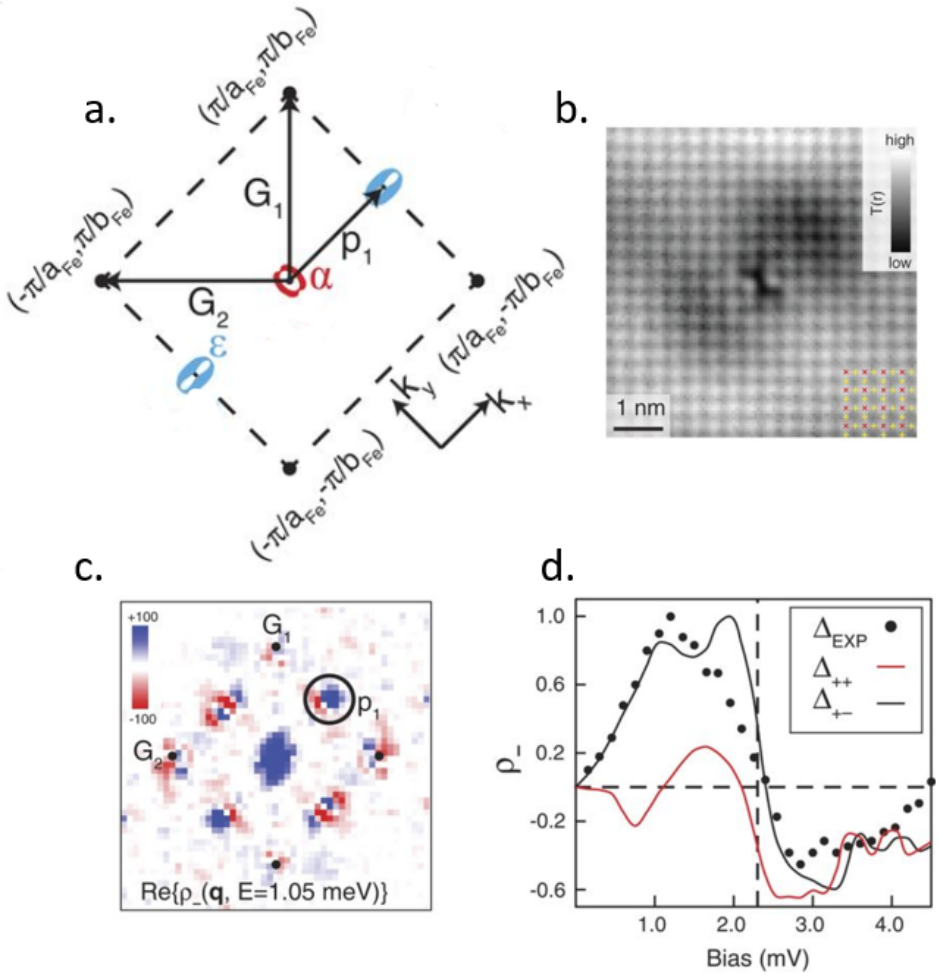

Figure 3.8: BQPI experiment on FeSe for implementing HAEM scheme. a) The scattering vector between α and ϵ band which was studied for superconducting gap sign. b) the FOV with a single atomic defect where BQPI was recorded. Red crosses denote the Se above atoms which are seen as bright atomic features in topograph. The yellow pluses denote the Fe which lie between Se sites as shown. c) The $\rho^{-}(\mathbf{q}, E)$ calculated from the BQPI pattern recorded in FOV shown in b), the scattering feature expected from a) is circled. d) The experimental data points for $\rho^{-}(E)$ obtained by summing $\rho^{-}(\mathbf{q}, E)$ over the region circled in c) for the scattering under study as shown in a) and the theoretically predicted $\rho^{-}(E)$ curves for s_{++} and $s_{\pm}$ overlaid. Figures reproduced from [39].

tations on this technique. It can be used only on materials where a) the disorder intensity was low enough that a single atomic defect can be isolated b) the BQPI signal from a single atomic defect is strong enough. We remedy these limitations in the new multi-atom scheme we propose in this thesis. It can be seen that the q-resolution is limited because of the FOV size restrictions which arise because single atomic defect centered FOV is required. Our new scheme also removes this issue. Please see chapter 5 for the details of this technique where we reproduce the results for FeSe and apply it on LiFeAs to find the gap symmetry.

CHAPTER 4

Sr_2RuO_4: MILLIKELVIN MULTIBAND QPI

When I first joined the Davis group, I was very excited to work on topological systems. Sr_2RuO_4 was a primary candidate for bulk topological superconductivity at the time and this formed the motivation for our studies. We have one of the few milliKelvin SI-STMs in the world which are capable of performing Bogoliubov quasiparticle interference (BQPI) hence this was an ideal albeit a very challenging problem for us to tackle. In this chapter, I first describe why the superconductivity in Sr_2RuO_4 has been a mystery for 25 years. Then I detail our experimental work aimed at understanding the superconducting state of Sr_2RuO_4. I describe the BQPI calculation which was instrumental for us to test our experimental results against different models. Finally, I put our results in the context of recent remarkable developments based on our experimental studies, I discuss what conclusions can be made about the superconducting state of Sr_2RuO_4.

4.1 Sr_2RuO_4: Mystery for 25 years

This section presents important developments in the saga of Sr_2RuO_4 which are important to put our work into perspective. For such an intensively investigated material, it is difficult to cite all the relevant work. Any omissions are results of my ignorance and I apologize for that. I owe immense gratitude to the researchers who have worked tirelessly on this challenging problem over the years and our work presented in this thesis is indeed *standing on the shoulder of giants*.

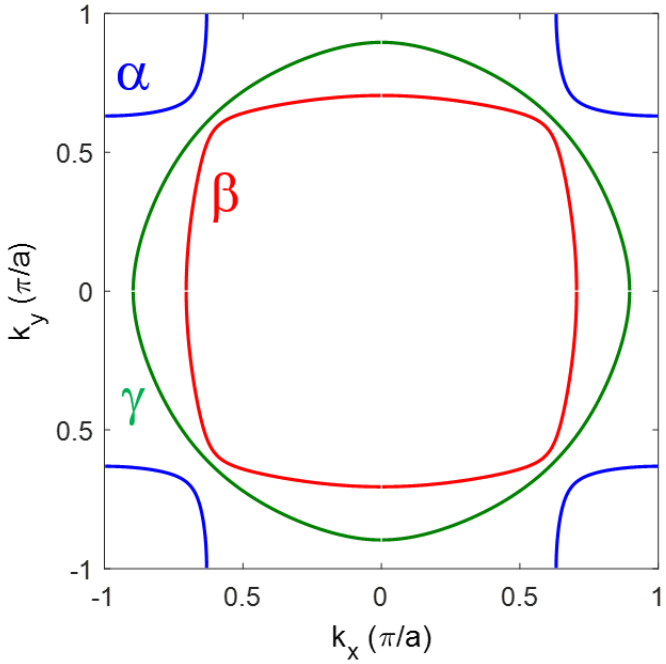

Figure 4.1: The Fermi surface of Sr_2RuO_4

Discovered in 1994 [51], the year this thesis is being written (2019) completes 25 years of mysterious superconductivity [52] in Sr_2RuO_4. The discovery of cuprates spurred a search for superconductivity in other transition metal oxides. Success was achieved with Sr_2RuO_4. However, the properties of Sr_2RuO_4 are very different from cuprates. The superconductivity appears at a very low temperature and is very sensitive to impurities [53] as compared to high temperature and robust superconductivity of cuprates. The normal state is a well defined and well understood Landau-Fermi liquid [54, 55, 56] as compared to highly anomalous normal state of cuprates. The Fermi surface of Sr_2RuO_4 consists of three bands derived from Ru t_{2g} orbitals as shown in Fig. 4.1. Quasi-1D d_{xz} and d_{yz} orbitals hybridize to yield an electron like pocket around Γ-point, called β band and a hole like pocket around X point, called α band. Quasi 2-D d_{xy} orbital leads to an electron like pocket around Γ-point, called γ band.

Sr_2RuO_4 started garnering attraction for being an exotic superconductor very early. Just after a year of its discovery, based on the similarity of effective masses to ^{3}He and strong Hund's rule coupling, Rice and Sigrist proposed that Sr_2RuO_4 can be an electronic analog of ^{3}He [57]. A triplet pairing was proposed to be arising from ferromagnetic fluctuations on γ band leading to an odd parity superconductor which is topological in nature [58]. Knight shift [59] experiments are an important tool to probe triplet pairing. In simple terms, Knight shift is the shift in NMR frequency of an atomic nucleus when the atom is in a magnetic vs. non-magnetic environment. In the case of superconductivity, as a material enters superconductivity, Cooper pair form from the individual metallic electrons. If pairing is singlet, the magnetic environment caused by metallic free electrons gets weaker as 2 spin-1/2 electrons combine into a Cooper pair of spin-0. Hence a drop in Knight shift is expected. However, if the pairing is triplet, 2 spin-1/2 electrons combine into a Cooper pair of spin-1 and the magnetic environment at the probed nucleus remains unchanged. Hence Knight shift remains unchanged as a result. First Knight shift experiment for Sr_2RuO_4 using ^{17}O NMR showed no change in Knight shift causing much excitement [60]. Early μSR [61] and Kerr effect experiments [62] showed time-reversal symmetry breaking. All this evidence pointed towards a gap of the form $k_x + ik_y$, on the gamma band originating from Ferromagnetic fluctuations.

However, the story was far from complete. A $k_x + ik_y$ order parameter leads to a full gap around the Fermi surface: $|\Delta(\mathbf{k})^2| = {k_x}^2 + {k_y}^2$. But linear dependence of electronic specific heat capacity in the gap [63], temperature dependence of London penetration depth [64], attenuation rate of ultrasound [65] and field-oriented specific heat measurements [66] all pointed towards gap nodes or deep minima in the gap. A lot of development in the theory followed to rec-

oncile these observations without changing the main idea of a gap on γ band due to ferromagnetic fluctuations. Orbital dependent superconductivity was proposed with γ band harboring the major gap or active gap, while induced gap occurs on $\alpha : \beta$ bands which might have deep minima to explain residual quasiparticles at low temperatures [67]. Though very unlikely for a 2D material like Sr_2RuO_4, an accidental horizontal node may occur if inter-planar hopping is taken into account [68] which may also explain some of the observed effects in experiments. Orbital dependent calculations were done showing deep minima on $\alpha : \beta$ bands exist but the major gap of the form $sin(k_x) + isin(k_y)$ gap on γ band was still considered the mainstay [69, 70, 71, 72].

Despite these important developments, this picture still had multiple unresolved issues. An important one is the absence of spontaneous magnetic fields and edge currents which a $k_x + ik_y$ gap should possess as a result of topology [58]. Very sensitive SQUID and scanning hall probe measurements have not found such fields/currents within 1mG [73, 74, 75] which stand in contrast with the time-reversal symmetry observations in μSR and polar Kerr effect experiments. An alternative view for the mechanism of superconductivity Sr_2RuO_4 was born out of neutron scattering revelations that ferromagnetic fluctuations on the γ band are quite weak but strong antiferromagnetic fluctuations existed at nesting wavevectors $(\pm 0.6\pi, \pm 0.6\pi, 0)$ for $\alpha : \beta$ bands. This led to the development of a picture that $\alpha : \beta$ bands are major bands instead of γ band and the gap has minima lying along [1,1]. It turned out that this picture could also explain many experimental results [76] including the important absence of edge currents in SQUID experiments [77, 78]. These fascinating developments in the study of Sr_2RuO_4 have been reviewed in Ref. [17] and [18].

In recent years, the landscape of Sr_2RuO_4 research has been changed radically by multiple experiments and this is where our studies of Sr_2RuO_4 enter the scene. In the following sections we will describe our experimental effort in detail and discuss the results and conclusions in the light of the latest status in the fascinating story of Sr_2RuO_4 in the last section.

4.2 Experimental Details for QPI and BQPI studies

It is clear from the discussion in the previous section that the gap on Sr_2RuO_4 possesses deep-minima/nodes. An important part of the problem is then, to probe the quasiparticle excitations at ultra-low energies: which bands and what k-space locations they come from; so as to finally figure out the gap structure which is a big experimental lead to figure out the pairing mechanism (1.2). We employed our dilution-fridge equipped SI-STM (chapter 2) to address this issue. High purity samples were grown using the floating zone technique [79] by Maeno group at the University of Tokyo. In this section we describe the methods and procedures for data acquisition and analysis for Sr_2RuO_4 BQPI studies.

4.2.1 Normal State of Sr_2RuO_4

We first studied Sr_2RuO_4 at 2.1K, with the aim to study the normal state to form the basis for our superconducting state studies later. We performed the scanning dI/dV spectroscopy acquire a map (as explained in section 2.2.3) on a grid of 256x256 pixels in a 50 nm field of view (FOV) with V_s = 20mV and I_s = 40pA and an energy range of E = +20meV to E = −20meV. The resulting $g(r, E)$ images

reveal vivid beautiful quasiparticle interference (QPI) in real space. A representative image is shown in Fig.4.2a. These images are setup-corrected as described in section 2.2.4. I must add, this was one of the biggest moments of awe in my physics journey to see electrons (quasiparticles) behave so clearly as waves. We take the power spectral density of the real space images to reveal the scattering wavevectors present at each energy, which encode the information about the electron spectral density, the normal state bands in this case. Fig.4.2b shows the corresponding power spectral density image in q-space . The major scattering vectors are shown with color-coded arrows. The same arrows are overlaid on the bands of Sr_2RuO_4 in Fig.4.2c to show what scattering in the k-space leads to the features in the measured q-space. This analysis shows that the tunneling occurs preferentially to $\alpha : \beta$ bands in Sr_2RuO_4 rather than γ band, a fact consistent with other STM experiments on Sr_2RuO_4 [76, 80]. This perhaps happens because the 2-D character of d_{xy}-band allows for a negligible overlap with the orbital at the end of the STM-tip. To get k-vectors from q-vectors, we can use the following equations which result from identification as shown in Fig.4.2c.

$$\begin{aligned} k_\alpha &= \frac{\pi}{a} - \frac{q_\alpha}{2} \\ k_\beta &= \frac{q_\beta}{2} \end{aligned} \tag{4.1}$$

We extract q-vectors from each energy and extract k-vectors using eq.(4.1). We overlay (k_x, k_y) extracted from our QPI on the ARPES Fermi surface [56] in Fig.4.2d, which shows very good agreement with bulk bands and hence establishes that we can identify $\alpha : \beta$ bands with great accuracy regardless of surface state contributions. Moreover we extract Fermi surface parameters and compare it with quantum oscillation experiments [54] in Table 4.1. For such comparison it should be kept in mind that we derive our k-vectors from measured

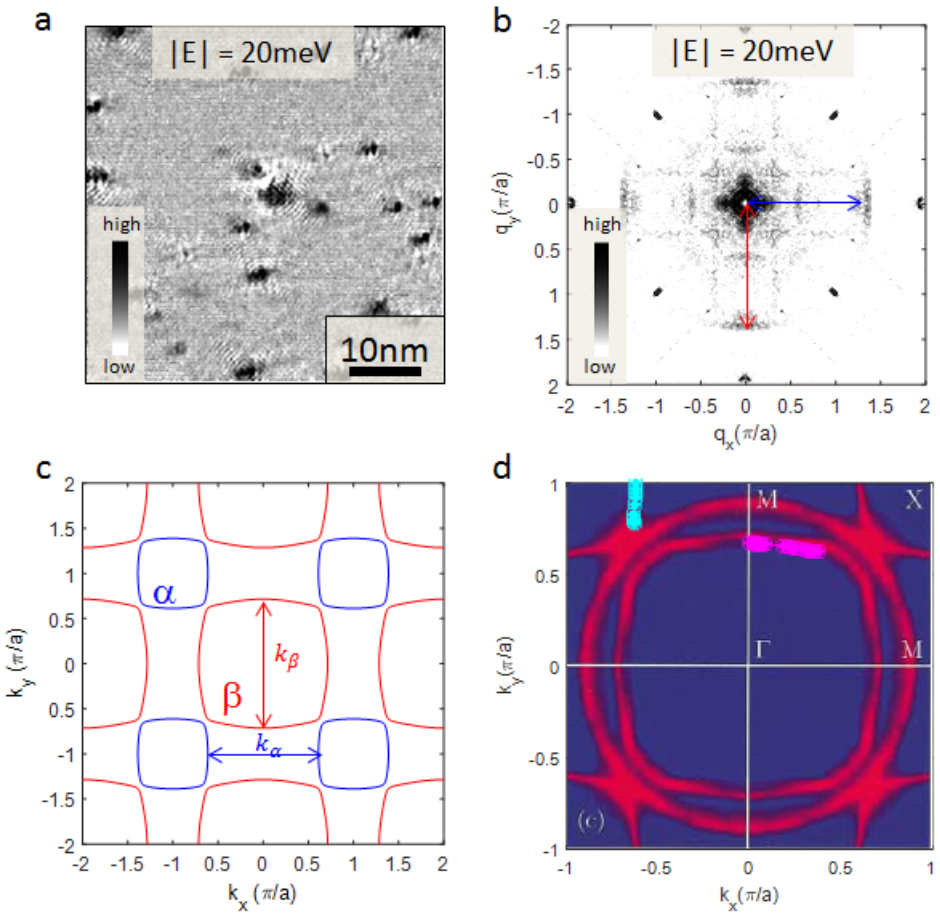

Figure 4.2: The normal state studies of Sr_2RuO_4. a) Vivid QPI oscillations as seen in setup corrected $g(r, E = 20meV)$ image at recorded at T=2.1K. b) Fourier Transform of the image in a. Arrows indicate the major scattering features. Red (Blue) arrow indicates intra (inter) beta (alpha) band scattering as shown in c. c) Fermi Surface of Sr_2RuO_4 with major scattering vectors as identified in b. overlaid. d) The (k_x, k_y) points for β (pink) and α (cyan) bands calculated using eq. (4.1) from the q-vectors identified from $E = 0$ layer overlaid on ARPES Fermi Surface [56]

.

q-vectors along maximum intensity directions [1,0] (Fig.4.2b) while quantum oscillation averages the quantities along the whole Fermi surface.

Quantity	Our Experiment	Mackenzie et al. [54]
$k_{F,\alpha}$ measured at $E = 0$ (1/A)	0.30 ± 0.02	0.30 ± 0.0006
$k_{F,\beta}$ measured at $E = 0$ (1/A)	0.55 ± 0.02	0.621 ± 0.008

Table 4.1: Comparison of FS parameters determined by our experiment and by Quantum Oscillation experiments by Mackenzie et al. [54]

In conclusion, the normal state studies establish:

- The tunneling occurs preferentially to $\alpha : \beta$ bands.
- We can identify the $\alpha : \beta$ bands accurately.

These observations are key to what follows in our quest to study the superconducting state of Sr_2RuO_4

4.2.2 Superconducting State of Sr_2RuO_4

To study the superconducting state of Sr_2RuO_4, we cool down to 90mK using our dilution fridge. We do that with the same sample we used during our normal state studies. Measurements at such low temperatures to achieve high energy resolution are challenging because one has to use a very small bias modulation (75μeV). In Sr_2RuO_4, this is especially challenging because the superconductivity is quite fragile in this material [53]. Since we want to probe superconductivity deep within the gap, the T_c needs to as high as possible which allows for a very small impurity density. And the fewer impurity scatterers means smaller BQPI signals. Our SI-STM as described in detail in chapter 2, is one of

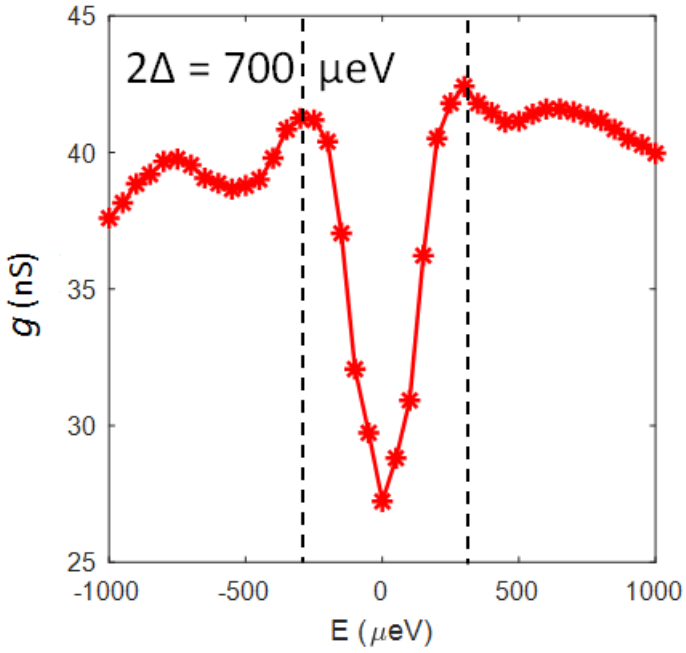

Figure 4.3: The tunneling spectrum on the superconducting Sr_2RuO_4

the few in the world which could have achieved this feat and I am fortunate to work with it and I feel grateful to all collaborators in having this opportunity.

Fig.4.3 shows a typical tunneling spectrum on the surface of Sr_2RuO_4 which shows a well-developed superconducting gap of size $\Delta = 350\mu$eV. The gap is V-shaped which indicates that the gap is anisotropic and possesses minima [76]. We perform dI/dV spectroscopy as mentioned in section 2.2.3 on a 128x128 pixel grid in a 20nm FOV with $V_s = 1$mV and $I_s = 40$pA. Fig.4.4a shows the topograph recorded while recording the map (see section 2.2.3). the impurities are circled with a red dashed line. Fig. 4.4b shows real space $g(r, E)$ image which are setup corrected (as mentioned in section 2.2.4). It can be seen that the quasiparticle density diminishes inside the gap. However it stays finite and even at $E = 0$, a finite density of Bogoliubov quasiparticles exists. This immediately tells us that the gap is anisotropic in this material and the gap minima has to be

greater than the bias modulation (75μ)eV. Fig.4.4c shows the $g(r, E)$ images with a self-normalized color scale. This reveals the Bogoliubov quasiparticle density modulations at the sites of impurities and encodes the information about the superconducting gap we want to reveal.

4.3 Data Analysis

With almost 25 years of conflicting literature [52], it was very challenging to understand the data to come up with valid conclusions for the superconducting state of Sr_2RuO_4. In this section we describe our analysis techniques for the superconducting state of Sr_2RuO_4.

4.3.1 Modeling the Superconducting State of Sr_2RuO_4

To aid in understanding of the Fourier transform of the BQPI images which encode the gap information, we present a pedagogical superconductivity model for Sr_2RuO_4. We start with the tight binding model which has been shown to fit superconducting STM spectra in previous work [76]:

$$\begin{aligned}
\epsilon_{xz} &= -\mu_0 - 2t\cos(k_x) - 2t_\perp\cos(k_y) \\
\epsilon_{yz} &= -\mu_0 - 2t\cos(k_y) - 2t_\perp\cos(k_x) \\
V_{hyb} &= -2V_m\sin(k_x)\sin(k_y) \\
\epsilon_\alpha &= \frac{1}{2}\left[(E_{xz}+E_{yz}) - \sqrt{(E_{xz}-E_{yz})^2 + 4V_{hyb}^2}\right] \\
\epsilon_\beta &= \frac{1}{2}\left[(E_{xz}+E_{yz}) + \sqrt{(E_{xz}-E_{yz})^2 + 4V_{hyb}^2}\right] \\
\epsilon_\gamma &= -\mu_z - 2t_z\Big(\cos(k_x)+\cos(k_y)\Big) - 4t_z'\cos(k_x)\cos(k_y)
\end{aligned} \tag{4.2}$$

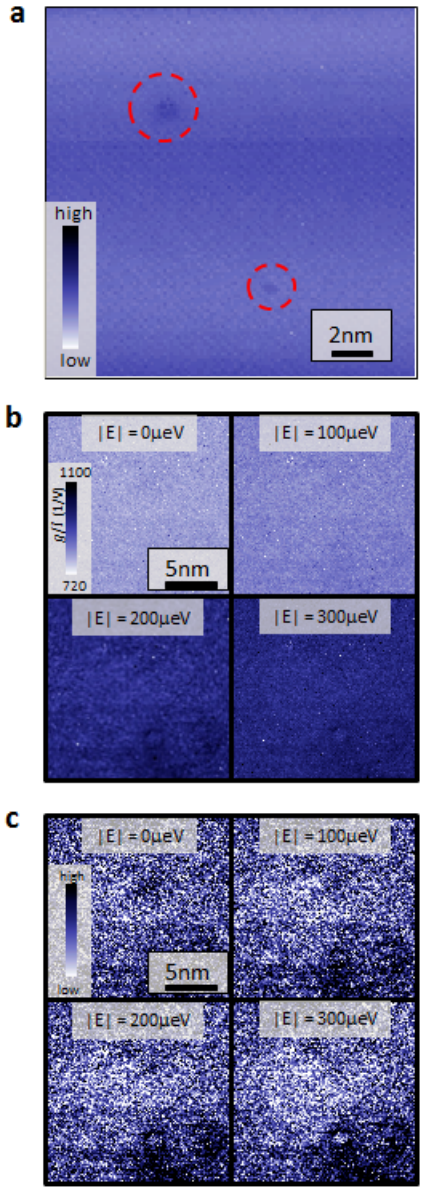

Figure 4.4: The real-space BQPI in Sr_2RuO_4. a) The topograph recorded at T=90mK simultaneously with the $g(r, E) = dI/dV(r, E)$ measurements. Red dashed circles denote the impurity atoms. b)The setup corrected g(r,E) images. Spectroscopic setup conditions were I=40pA and V=1mV. Notice how the overall quasiparticle intensity decreases as we enter the gap, but stays finite even at $E = 0$. Just looking at this picture tells us that we are dealing with minima deeper than our bias modulation. c) The images presented in b. with a self-normalized color scale for each image. the scattering interference can be seen as intensity modulation at the locations of impurities as marked in a.

where the parameters in the unit of t are given as $(\mu_0, t_\perp, V_m, \mu_z, t_z, t'_z) = (1.0, 0.1, 0.1, 0.55, 0.2, 0.7)$ and we take $t = 100m$eV as in [76]. We explore a gap with nodes along $(\pm1, \pm1)$ on $\alpha : \beta$-bands: $\Delta_{\alpha/\beta}(\mathbf{k}) = \Delta_0 \left(\cos(k_x) - \cos(k_y)\right)$ We set the gap size as measured in our experiments $\Delta_0 = 350\mu eV$. Fig.4.5a indicates the relative gap sizes $|\Delta_\alpha(\mathbf{k})|$,$|\Delta_\beta(\mathbf{k})|$ on the bands with the thickness of curve overlaid on $\alpha : \beta$ Fermi surface. Following the formalism described in section 3.4.1, in the basis $\psi^\dagger = (c^\dagger_{\alpha,\mathbf{k}\uparrow}, c_{\alpha,-\mathbf{k}\downarrow}, c^\dagger_{\beta,\mathbf{k}\uparrow}, c_{\beta,-\mathbf{k}\downarrow})$ we get a Bogoliubov de Gennes Hamiltonian $\sum_k \psi^\dagger(\mathbf{k})\hat{H}(\mathbf{k})\psi(\mathbf{k})$ where:

$$\hat{H}(\mathbf{k}) = \begin{pmatrix} \epsilon_\alpha(\mathbf{k}) & \Delta_\alpha(\mathbf{k}) & 0 & 0 \\ \Delta^*_\alpha(\mathbf{k}) & -\epsilon_\alpha(\mathbf{k}) & 0 & 0 \\ 0 & 0 & \epsilon_\beta(\mathbf{k}) & \Delta_\beta(\mathbf{k}) \\ 0 & 0 & \Delta^*_\beta(\mathbf{k}) & -\epsilon_\beta(\mathbf{k}) \end{pmatrix} \tag{4.3}$$

where $\epsilon_\alpha(\mathbf{k})$,$\epsilon_\beta(\mathbf{k})$ are the band dispersion of $\alpha : \beta$-bands as given in (4.2). The unperturbed Green's function is given by $G^0(\mathbf{k}, \epsilon) = [(\epsilon + i\delta)I - \hat{H}(\mathbf{k})]^{-1}$ where I is identity matrix and δ is the energy width broadening parameter. We use the experimental parameters by setting $\delta = 150\mu$eV which is $\approx$ our bias modulation. Both interband and intraband scattering within $\alpha : \beta$ bands is considered using the scattering potential:

$$V_s = \begin{pmatrix} V_{intra} & 0 & V_{inter} & 0 \\ 0 & -V_{intra} & 0 & -V_{inter} \\ V_{inter} & 0 & V_{intra} & 0 \\ 0 & -V_{inter} & 0 & -V_{intra} \end{pmatrix} \tag{4.4}$$

$$= (V_{intra} I + V_{inter}\sigma_x) \otimes \sigma_z$$

T-matrix for all scattering process can be written as:

$$T(E) = \left(I - \sum_{\mathbf{k}} G_0(\mathbf{k}, E) V_s \right)^{-1} V_s \tag{4.5}$$

Finally, the Bogoliubov quasiparticle density due to the scattering is given by

$$\delta N(\mathbf{q}, E) = -\mathrm{Im} \left[\sum_{i=1,3} \left(\sum_{\mathbf{k}} G^0(\mathbf{k}+\mathbf{q}, E) T(\epsilon) G^0(\mathbf{k}, E) \right) \right]_{ii} \tag{4.6}$$

We take $(V_{intra}, V_{inter}) = (1.0, 0.1)$. Fig.4.5b shows the resulting spectral density $A(\mathbf{k}, E) = -\frac{1}{\pi}\mathrm{Im}\left(G^0(\mathbf{k}, E)\right)$ of Bogoliubov density of states calculated with the $\alpha : \beta$-bands with our pedagogical gap. The scattering between Bogoliubov quasiparticles is dominated by scattering between the banana-tips [50], which we indicate with color-coded arrows. Fig.4.5c shows the Bogoliubov quasiparticle interference calculated via (4.6) (for detailed theory, technical procedures and codes, please refer to chapter 3). The major scattering arrows expected as in Fig4.5b are seen clearly as shown by the overlaying of the same arrows on Fig.4.5c. This internal consistency validates our simulations and parameters.

We have not included γ-band in this model as we did not see tunneling into the γ-band. The interband-scattering from γ-band to $\alpha : \beta$-bands is also not considered as they are different in character ($\gamma : d_{xy}$ and $\alpha, \beta : d_{xz}, d_{yz}$) and theoretical models till date have not considered it [81, 82, 83]. We however, present what the BQPI patterns, if γ bands were present would look like. We follow the single band BQPI model as we discussed in section 3.4 and use a common gap model from literature [72, 70, 71] $\Delta_\gamma = \Delta_0(sin(k_x) + isin(k_y))$. The Hamiltonian in the basis

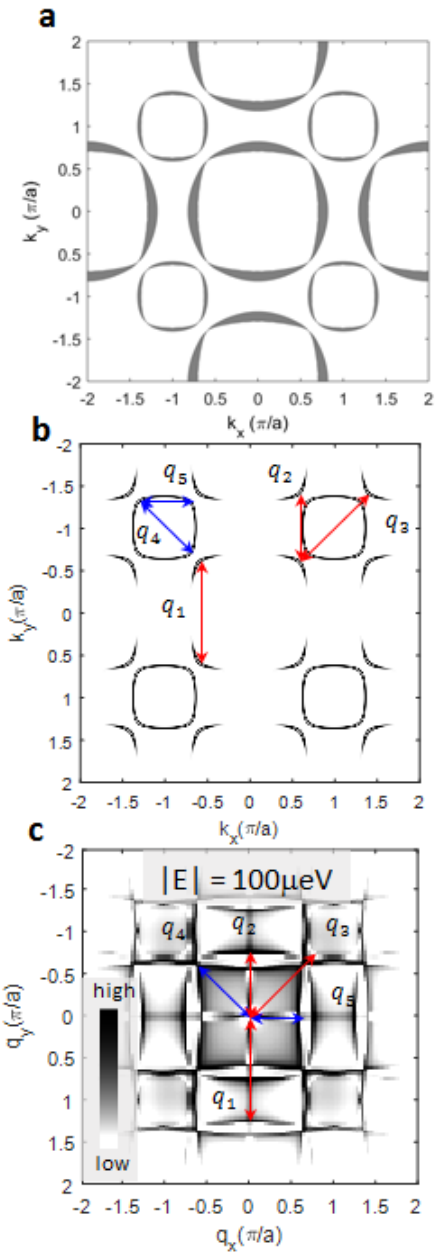

Figure 4.5: Model for the superconducting state of Sr_2RuO_4. a) Gap magnitude on the Fermi surface for α : β-bands and with gap minima along $(\pm 1, \pm 1)$. b) Regions of significant quasiparticle density $E \to 0$ for α : β-bands when gapped as shown in a). c) Major scattering vectors are labeled as $q_j; j = 1, 2, 3, 4, 5$. d) Calculated $g(q, E)$ pattern as described in section 4.3.1 for α : β-bands from the model in a) at $E = 100\mu eV$. Key scattering wavevectors are indicated by $q_j; j = 1, 2, 3, 4, 5$.

$(c^{\dagger}_{\gamma\mathbf{k}\uparrow}, c_{\gamma-\mathbf{k}\downarrow})$ is given by

$$\hat{H}(\mathbf{k}) = \begin{pmatrix} \epsilon_{\gamma}(\mathbf{k}) & \Delta_{\gamma}\mathbf{k} \\ \Delta^{*}_{\gamma}\mathbf{k} & \epsilon_{\gamma}(\mathbf{k}) \end{pmatrix} \tag{4.7}$$

Unperturbed Green's function is $G^0(\mathbf{k}, E) = \left[(E + i\delta) - \hat{H}(\mathbf{k})\right]^{-1}$ and the T-matrix is given as $T(E) = (I - V_s \sum_{\mathbf{k}} G_0(\mathbf{k}, E))^{-1} V_s$ and finally the BQPI pattern can be calculated as $\delta N(\mathbf{q}, E) = -\text{Im}\left[\left(\sum_{\mathbf{k}} G^0(\mathbf{k}+\mathbf{q}, E) T(E) G^0(\mathbf{k}, E)\right)\right]_{11}$. We present the results of these calculations in Fig.4.6a-d. For comparison we show the results of same calculations for $\alpha : \beta$ bands at corresponding energies. A comparison to the data and simulations presented in the Fig.4.7 makes it clear that we see no γ-band BQPI features. We put the arrows expected from our pedagogical model for superconducting Sr_2RuO_4 as shown in Fig.4.5b and c. on Fig.4.6d and l. to show that the features we expect are not likely to come from γ-band BQPI Fig.4.6d.

4.3.2 Discussion of BQPI results

Fig.4.7a-d show the power spectral density obtained by Fourier Transforming the recorded $g(\mathbf{r}, E)$ images as shown in Fig. 4.4. The signal to noise ratio in these images reflects the challenge of this experiment as the density of scatterers has to be low to maintain a high T_c, leading to low signal and then the probing bias modulation also has to be small for high energy resolution which leads to much larger averaging time and one needs to optimize greatly. The activity at low-$\mathbf{q}$ is usually from long-range disorder/drift rather than any specific low-$\mathbf{q}$ scattering hence we usually ignore the region $-\pi/2a < q < \pi/2a$. There are a few things immediately obvious from looking at the images. The images change from one to another in 100μeV steps, this means that our energy resolution is

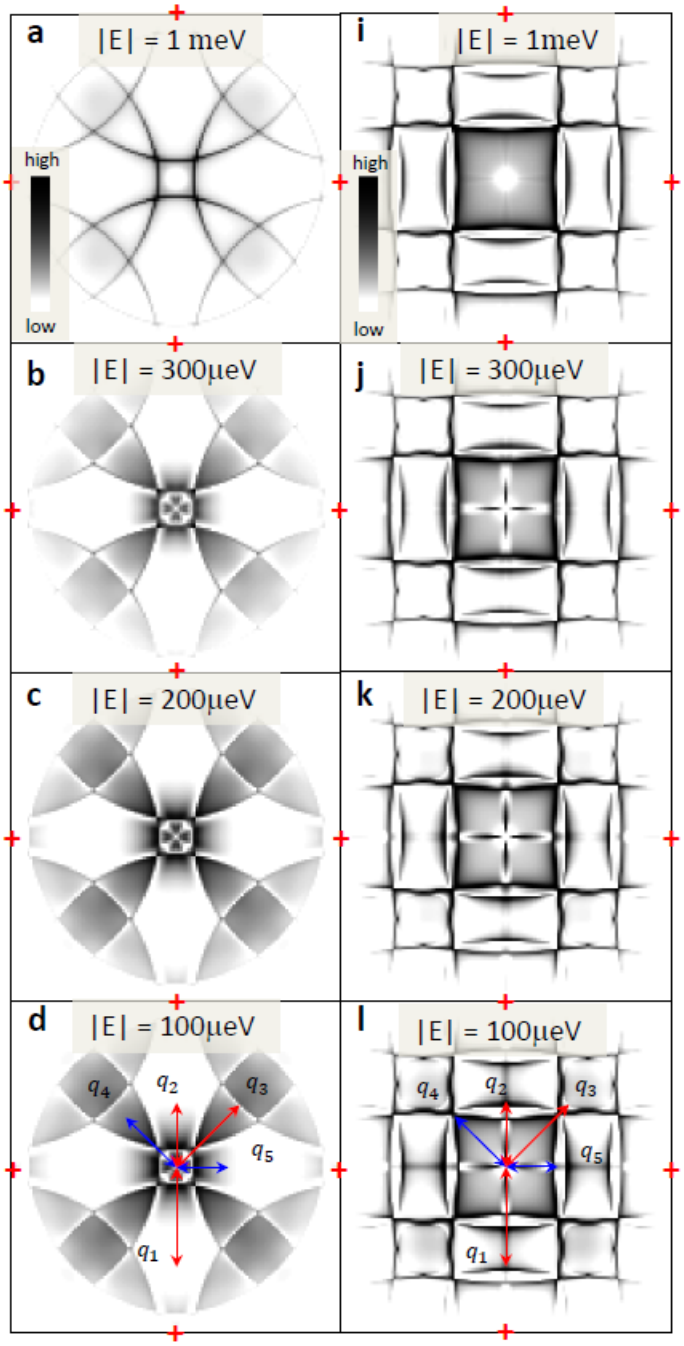

Figure 4.6: Gamma band BQPI patterns.a)-d) show the result of BQPI calculations done using only γ-band. For comparison e)-h) show the BQPI calculations done with $\alpha : \beta$-bands. The arrows in d) and l) are the five principle q-wavevectors we expect from scattering within our pedagogical model as shown in Fig.4.3.1b and c. which show that they are not likely to result from γ-band BQPI.

manifestly less than 100μeV and we are not averaging over energies larger than 100μeV. The BQPI image at $E = 0$ in Fig. 4.9b shows significant signal, hence the gap has to be anisotropic with minima deeper than our bias modulation: $\Delta^{min}_{\alpha,\beta}(\mathbf{k}) < 75\mu$eV. Fig.4.7a shows energy layer at $E = 1m$eV which we can compare with normal state QPI image shown in Fig.4.2b to immediately see that the tunneling is occurring preferentially in $\alpha : \beta$ bands. With the simultaneous tunneling spectrum as shown in Fig.4.3 showing a gap maximum $\Delta^{max} = 350\mu$eV, it can be concluded that this superconducting gap is hosted by $\alpha : \beta$-bands. Moreover, since the observed $\Delta^{max} = 350\mu$eV is a consistent gap maximum for bulk superconducting critical temperature $T_c = 1.45$K, this indicates that $\alpha : \beta$ bands host the major gap in the superconducting state of Sr_2RuO_4 which we probe in our experiments.

The BQPI for $E < \Delta^{max}$ (Fig.4.7b-d) exhibit a new distinctive pattern for $g(\mathbf{q}, E)$ when compared with $E > \Delta^{max}$ (Fig.4.7a). The patterns show clear maxima which evolve but do not disappear as $E \to 0$. To understand these results, Fig. 4.7e-h show theoretical simulations performed using our pedagogical gap model with nodes along $(\pm 1, \pm 1)$ as shown in Fig.4.5 and discussed in section 4.3.1. The dispersion in main features is weak within the gap. This fact is in agreement with our simulations and also with other theoretical studies of the BQPI patterns in Sr_2RuO_4. The pattern in Fig.4.7d. is quite representative and agrees well with the modeling presented in Fig.4.7h. To compare the main q-wavevectors expected from the model as shown in Fig.4.5b and c, we put circles on these wavevector locations in Fig.4.8 showing both the simulations of our model and the measured BQPI. The good agreement between the measured and the simulated model shows that the superconducting gap in Sr_2RuO_4 has nodes/minima in the are along the $(\pm 1, \pm 1)$ directions on $\alpha : \beta$ bands.

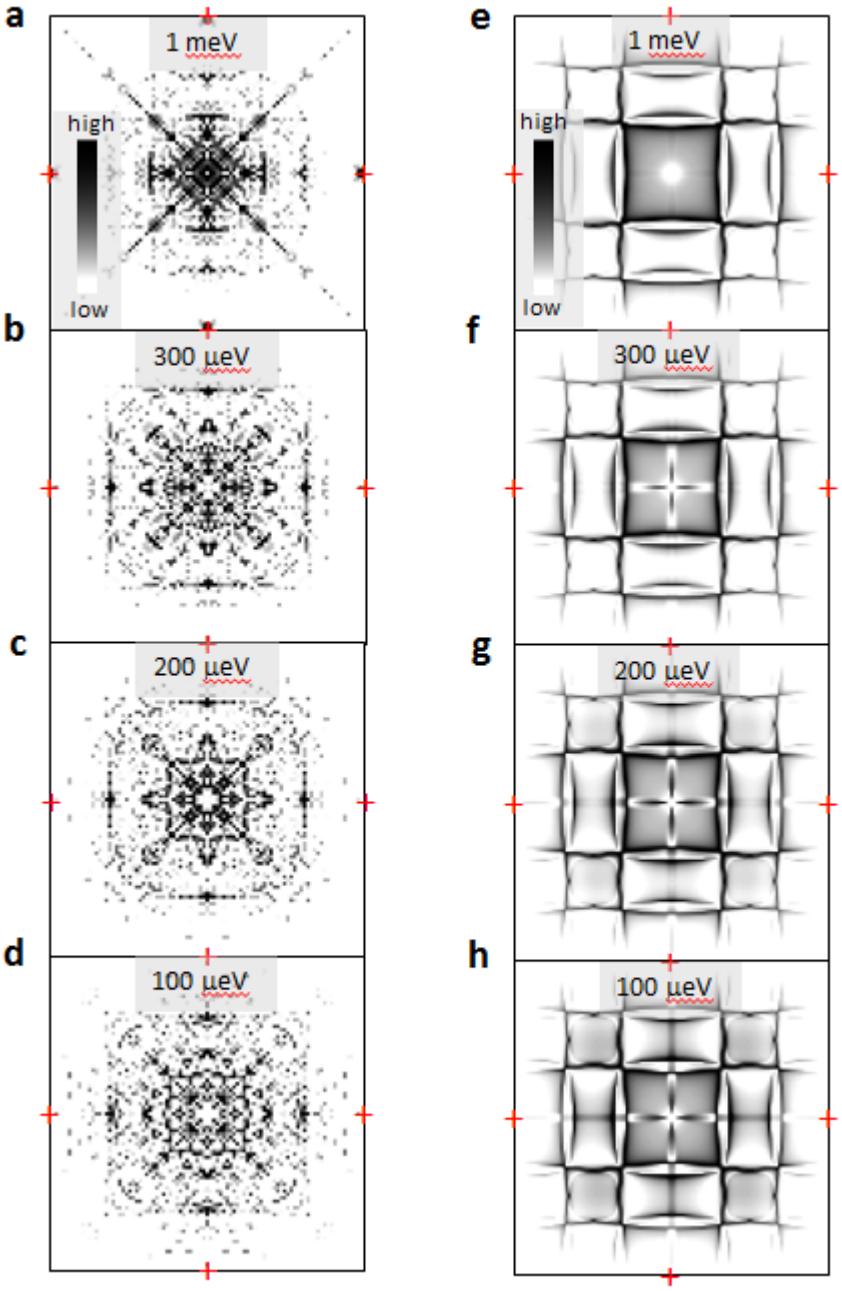

Figure 4.7: Comparison of the BQPI images and simulations for superconducting state of Sr_2RuO_4 at T=90mK. a) to d) Measured $g(\mathbf{q}, E)$ images at T=90mK. in superconducting state of Sr_2RuO_4 at E = 1eV, 300μeV, 200μeV and 100μeV. Red crosses denote Bragg peaks. e) to h) Predicted $\delta N(\mathbf{q}, E)$ for α : β-bands with minima along $(\pm 1, \pm 1)$ as calculated as described in section 4.3.1 at E = 1meV, 300μeV, 200μeV and 100μeV. Red crosses denote Bragg peaks

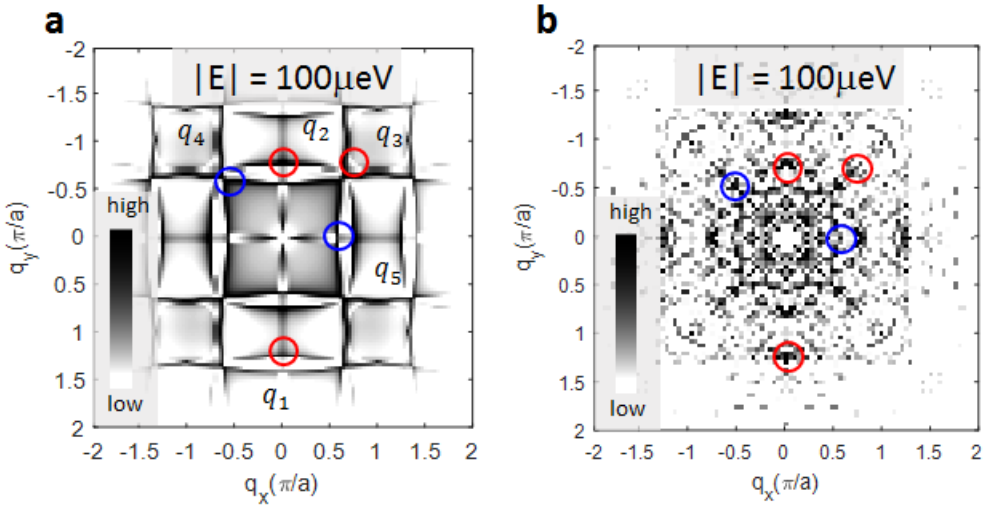

Figure 4.8: Key wavevectors in the BQPI images. a) Predicted BQPI scattering pattern with red (blue) circles at the locations of wavevectors expected as shown in Fig.4.3.1b and c. b) Measured BQPI pattern with circles at similar locations as in a.

We analyze the nature of nodes further by constraining the maximum angle they can subtend with the $(0,0) \rightarrow (\pm 1, \pm 1)$ or ΓX-direction. Fig.4.9a shows the scattering wavevector range for q_3 and q_4, which leads to a finite width in the features as can be seen in the $E = 0\mu eV$ image shown in Fig.4.9. This width w and the length of scattering wavevector d can be used to estimate the farthest angle the nodes can be from ΓX-direction as shown in Fig.4.9a. Fig.4.9c and d show zoomed in view of q_3 and q_4 and indicates the w and d. Using $\theta_X = atan(w/d)$, we find the angle subtended about X-point by the nodes is $\theta_X = 0.18$ and $\theta_X = 0.22$ for q_3 and q_4 respectively. About Gamma point then, the angle subtended is approximately $\theta_\Gamma = 0.1$ radians. Hence, the gap minima/nodes in Sr_2RuO_4 along $(\pm 1, \pm 1)$ are at a maximum angular distance of 0.05 radians away from ΓX-direction measured about Γ-point.

This analysis is important because there are two main candidates for the gap-nodes along ΓX-direction: accidental nodes as predicted in helical p-wave

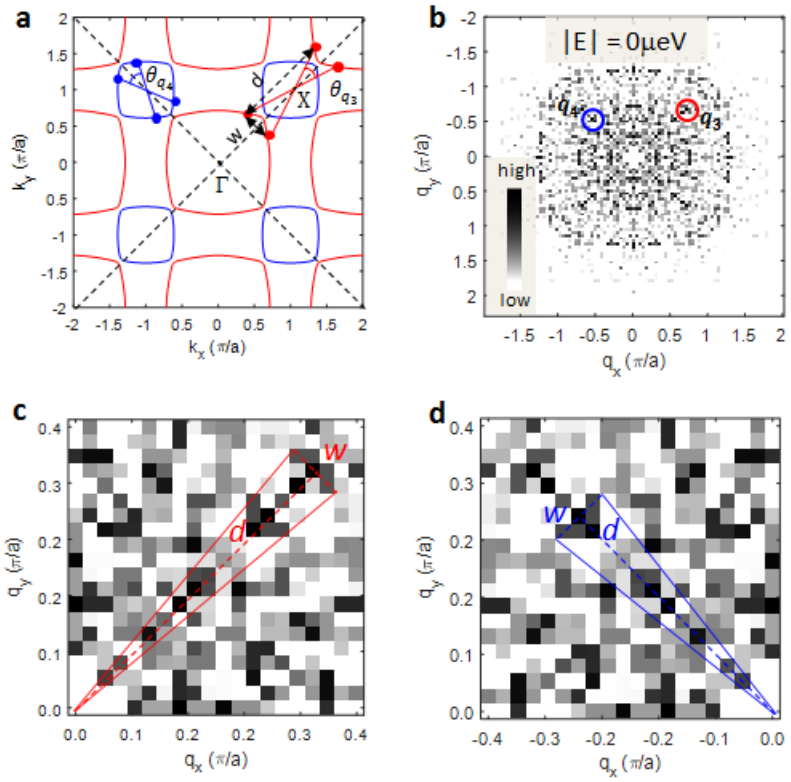

Figure 4.9: Angular distance of gap minima/nodes from Γ*X*-direction. a) Schematic of the scattering in k-space which leads to scattering features q_3 and q_4 in BQPI. b) Experimental g(q,E) measured at $0\mu eV$ showing q_3 and q_4. c) Zoomed view of q_3 showing w and d to determine θ. d) Zoomed view of q_4 showing w and d to determine θ

gap [84] or symmetry imposed nodes resulting from a $d_{x^2-y^2}$-wave gap. There is no strict criterion for accidental nodes in helical p-wave gap to be pinned o Γ*X*-direction while obviously, the $d_{x^2-y^2}$-wave gap must be along Γ*X*-direction. This analysis indicates that $d_{x^2-y^2}$-wave gap seems a more natural conclusion from our data because for this observation to be consistent with helical p-wave gap, fine-tuning and coincidence is required.

4.4 Discussion

Since a lot of experimental data exists and multiple recent experiments have raised new questions, in this section, we put our results presented in this thesis into context here and reflect on the overall picture of the problem of superconductivity in Sr_2RuO_4.

4.4.1 Recent Experimental Context

For the last 25 years, the intense research in Sr_2RuO_4 has gone through many ebbs and flows. Please refer to section 4.1 and references therein for a historical overview. Recently, lots of experiments have challenged the *ancien regime* in Sr_2RuO_4. We list some important ones to put our experiments in the recent context. One of the most important recent evidence comes from the NMR experiments [85] which shows that there is a significant drop (50%) in the Knight shift in the superconducting state of Sr_2RuO_4. This immediately rules out the chiral odd-parity parameters which has an out of plane d-vector [18] (see section 1.2.1 for a discussion of d-vector), which predicts no drop in the Knight shift for probing magnetic fields along the *ab*-plane. This is because the chiral d-vector is out of plane and hence all the triplets are in the plane and contribute to the magnetic susceptibility with no drop. The results in [85], which show a drop in Knight shift are in contrast with earlier Knight shift results [60] which showed no drop. The earlier results actually were a result of sample heating which brought the sample to the normal state, leading to pair breaking and effectively normal state leading to no Knight shift as the temperature was lowered below T_c. A comprehensive study of the magnetic field and temperature dependence of thermal

conductivity was performed by Hassinger et al. [86] which revealed a lot of important facts about the superconducting state of Sr_2RuO_4. Values of thermal conductivity along the c-axis in the superconductivity show that the quasiparticles have non-zero velocity along the c-axis, and they are excited at a much smaller magnetic field in the superconducting state which is a strong evidence that the nodes have to be vertical. A recent Josephson experiment [87] shows that reversing both the bias current and magnetic field across a Nb-Sr_2RuO_4 corner Josephson junction leads to the same I_c vs. H curve, implying that the time-reversal symmetry is actually preserved, which is strong evidence against chiral order parameters which will break time-reversal symmetry.

4.4.2 Results and Conclusions

Despite multiple recent experiments providing pieces of the puzzle, the key questions for this enigmatic multiband superconductor still remained:

- Which bands contain major superconducting gap?
- What is the k-space structure of the superconducting gap on these bands?

  Direct visualization with techniques which can distinguish bands and k-space structure were needed.

  Our work in this thesis answers these two important experimental questions by direct visualization as we have mentioned in this chapter. The presence of full bulk superconducting gap ($\Delta = 1.73 k_B T_c$) while our tip was demonstrably sensitive to $\alpha : \beta$-bands shows that $\alpha : \beta$ bands possess the major gap. The BQPI pattern we observe is consistent with nodes along $(\pm 1, \pm 1)$ directions and exist within 0.05 radians of the ΓX-line. These

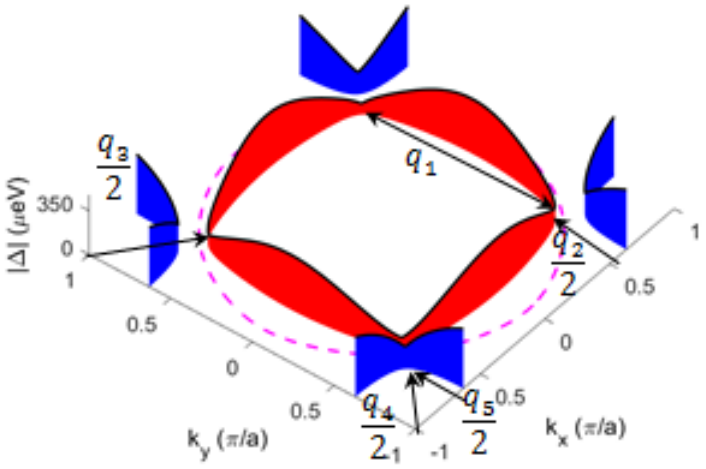

Figure 4.10: Superconducting gap structure of Sr_2RuO_4 determined by BQPI. The arrows show the major scattering vectors we observe in our experiment, consistent with this picture.

findings are most consistent with a $d_{x^2-y^2}$ symmetry gap structure on both α and β bands as shown in Fig. 4.10.

What does this tell us about the origin and nature of superconductivity in Sr_2RuO_4? Inelastic neutron scattering [88] has shown strong incommensurate antiferromagnetic (AFM) fluctuations at $(\pm 0.6\pi/a, \pm 0.6\pi/a, 0)$. This indicates that the superconductivity in Sr_2RuO_4 may emerge out of AFM fluctuations acting as the pairing glue. Indeed recent first-principles calculations [89, 84, 90] taking into account the orbital weights, spin fluctuations and charge fluctuations show that close to this magnetic instability, a d-wave singlet state is favored. Most importantly, our experiments indicate that Sr_2RuO_4 maybe a singlet-even parity superconductor, hence not a topological superconductor. This is a revolutionary conclusion for the field, as Sr_2RuO_4 has been touted as a topological superconductor for

many years and much work has also been done in touting it as a platform for topological quantum computing. Our work guides the field in the right direction by providing more direct evidence for non-topological nature of Sr_2RuO_4 and encouraging the search for topological superconductivity in other candidate systems.

CHAPTER 5

LiFeAs: MULTI-ATOM HAEM

As most students of superconductivity, I was first introduced to the standard BCS kind, where the superconducting order parameter is a constant. When I first heard of unconventional superconductors, I was quite fascinated to learn about cuprates which have an order parameter having a d-wave symmetry, which changes sign every $\pi/2$ rotation on Fermi surface! There are multiple techniques to measure the magnitude of the superconducting order parameter, but very few to measure the phase or the sign of the superconducting order parameter. While working on my research in Davis group, Peter Sprau, Andrey Kostin and colleagues developed a technique to measure the sign of the superconducting gap for iron-based superconductor FeSe [39] which was based on a theoretical proposal dubbed HAEM based on the last names of theorists who proposed it (please see section 3.5). This chapter describes a novel scheme which extends the applicability of HAEM in important ways.

I start with an intuitive discussion of why the superconducting order parameter might change sign and why this information might be important to learn. (For more mathematical treatment, please see section 1.2) Then I describe the multi-atom analysis technique we developed. We show that the technique works by applying it to previously studied material FeSe [39] and comparing our results with the original work. Equipped with our new technique, we address an important standing problem of gap symmetry in LiFeAs. I give a brief overview of why studying the superconducting order parameter sign for LiFeAs is an important step in the overall understanding of superconductivity and iron-based superconductivity in particular. Then we finally present the

results of our multi-atom analysis on LiFeAs which show that LiFeAs superconducting gap has a $s_{\pm}$ symmetry.

5.1 Sign of a Superconducting Gap

For BCS superconductors, the reason for electrons to come together and form a Cooper-pair is electron-phonon interaction [2]. A hand waving picture is that the electron attracts the lattice of positive ions around it when it passes through and that generates a momentary positive charge at that location that attracts another electron. This works because lattice dynamics are much slower than electrons because of their enormous mass difference. The Cooper-pair wavefunction has a maximum at zero separation and its magnitude is constant all around the Fermi surface in the most standard picture as shown in Fig.5.1a. This is known as the s-wave symmetry (recall spherically symmetric s-orbitals, this nomenclature derives from angular momentum harmonics. See section 1.2.2 for details)

However, there might be cases where the interactions causing the pairing of electrons into Cooper-pairs is different from standard BCS superconductors. For other interactions than electron-phonon interactions, it might cost energy to have wavefunction peaked at zero separation, but favorable to have node at 0 separation. This might lead to Cooper pair formation in higher angular momentum channels [91]. For example, Fig. 5.1b shows an order parameter with d-wave symmetry, which has 4 nodes and changes sign every $\pi/2$ rotation. Such superconductors are usually known as unconventional superconductors. Unconventional superconductors pose a lot of questions: What interactions act as a glue to form the Cooper-pairs? What are the properties of the superconduct-

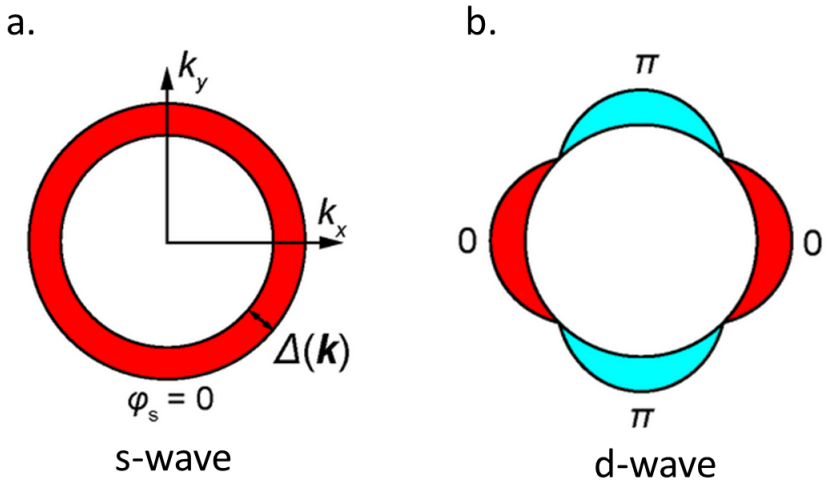

Figure 5.1: Order parameter symmetries for superconductors. a) A s-wave order parameter with phase $\varphi = 0$ for all momenta $\mathbf{k}$. b) A d-wave order parameter showing nodes and varying phase (sign) with each $\pi/2$ rotation in k-space from $\varphi = 0$ to $\varphi = \pi$. Figure reproduced from S. Yonezawa, Condens. Matter, 4(1), 2 (2019)

ing state itself? In what respects are they similar/different to well known BCS superconductors? To attempt to answer all these questions and have a complete understanding of a superconductor, it is essential to understand the symmetry of the order parameter [15]. This involves understanding the phase or the sign of the order parameter as well, along with the magnitude. BQPI measurements using SI-STM can address both these issues (please see Chapter 2). The HAEM scheme which uses BQPI for gap sign determination is thus an important advance in our toolbox to study these fascinating states of matter.

5.2 Phase Recovery with Multi-Atom Fourier Transform

The HAEM technique established by Sprau et. al [39] required that the atomic defect be centered precisely at the origin of coordinates, with respect to which

Re δN and Im δN are then properly defined. This requirement is critical because, on the scale of a crystal unit-cell, a small error in the coordinate of the origin (at the impurity atom) produces major errors in Re δN and Im δN as they oscillate rapidly and their sign cannot be determined accurately which is required to make interpretation regarding sign of the gap (eq. (3.33)). In this section, we will discuss how this error occurs mathematically and how it can be corrected using a *multi-atom Fourier transform*.

5.2.1 Pathology in Fourier Transform due to the Shift in The Origin

For a perfectly centered atomic defect, the BQPI $\psi(\mathbf{r})$ would be even with respect to the origin and the Fourier transform (we denote the operation of Fourier transforming by $\mathcal{F}$) would be completely real (a well-known theorem of Fourier transform).

$$\begin{aligned} \mathcal{F}\delta N(\mathbf{r}) &= \int \delta N(\mathbf{r}) e^{i\mathbf{q}\cdot\mathbf{r}} d\mathbf{r} \\ &= \delta N(\mathbf{q}) \in \mathbb{R} \end{aligned} \tag{5.1}$$

Hence

$$\text{Re}\,\mathcal{F}\delta N(\mathbf{r}) = \delta N(\mathbf{q}); \quad \text{Im}\,\mathcal{F}\delta N(\mathbf{r}) = 0 \tag{5.2}$$

Now if we shift the impurity by $\boldsymbol{\delta}$, we have

$$\begin{aligned} \mathcal{F}\delta N(\mathbf{r}+\boldsymbol{\delta}) &= \int \delta N(\mathbf{r}+\boldsymbol{\delta}) e^{i\mathbf{q}\cdot\mathbf{r}} d\mathbf{r} \\ &= e^{-i\mathbf{q}\cdot\boldsymbol{\delta}} \int \delta N(\mathbf{r}+\boldsymbol{\delta}) e^{i\mathbf{q}\cdot(\mathbf{r}+\boldsymbol{\delta})} d(\mathbf{r}+\boldsymbol{\delta}) \\ &= e^{-i\mathbf{q}\cdot\boldsymbol{\delta}} \delta N(\mathbf{q}) \end{aligned} \tag{5.3}$$

Hence

$$\text{Re}\,\mathcal{F}\delta N(\mathbf{r}+\boldsymbol{\delta}) = \cos(\mathbf{q}\cdot\boldsymbol{\delta})\delta N(\mathbf{q}); \quad \text{Im}\,\mathcal{F}\delta N(\mathbf{r}+\boldsymbol{\delta}) = -\sin(\mathbf{q}\cdot\boldsymbol{\delta})\delta N(\mathbf{q}) \tag{5.4}$$

Now the Fourier transform has a real and an imaginary part which oscillates with a spatial frequency of q, which can be quite high.

The effect of shift of the origin is illustrated in Fig. 5.2. We have simulated Friedel oscillations with a functional form $\frac{\cos(\mathbf{k_0}\cdot\mathbf{r}+\vartheta)}{k_0 r}e^{-\kappa r}$. The exponentially decaying factor simulates the real situation in experimental BQPI where the BQPI decays away from the origin of the defect. Fig. 5.2a shows Friedel oscillations emanating from an atomic defect centered at the origin. As eq. (5.2) predicts, the imaginary part is almost zero, as shown in Fig. 5.2c and the real part is strong as shown in Fig. 5.2b. The azimuthally integrated real part of the Fourier transform shows the peak in the Fourier transform at $q = k_0$ as expected and the sign is clear. Setting the phase $\vartheta = 0$ to $\vartheta = \pi$ in the Friedel oscillations, the sign of the real part of the Fourier transform changes as expected. In Fig. 5.2e, we show a Friedel oscillation with origin shifted by $\boldsymbol{\delta}$ and the Fourier transform now has rapidly oscillating real (Fig. 5.2f) and imaginary (Fig. 5.2g) parts as predicted by eq. 5.4. The azimuthally integrated real part as shown in Fig. 5.2h now contains these rapid oscillations and they make determining the sign of real part impossible and hence no distinction can be made in the case of Freidel oscillations with phase $\vartheta = 0$ and $\vartheta = \pi$.

Hence we can see clearly that with multiple atomic defects with random locations, there is no hope to recover the sign of the real part of Fourier transform and make any conclusions, which are key to the HAEM technique(eq.(3.33)). We discuss how we can recover the sign information scrambled by the issue of randomized origins of BQPI.

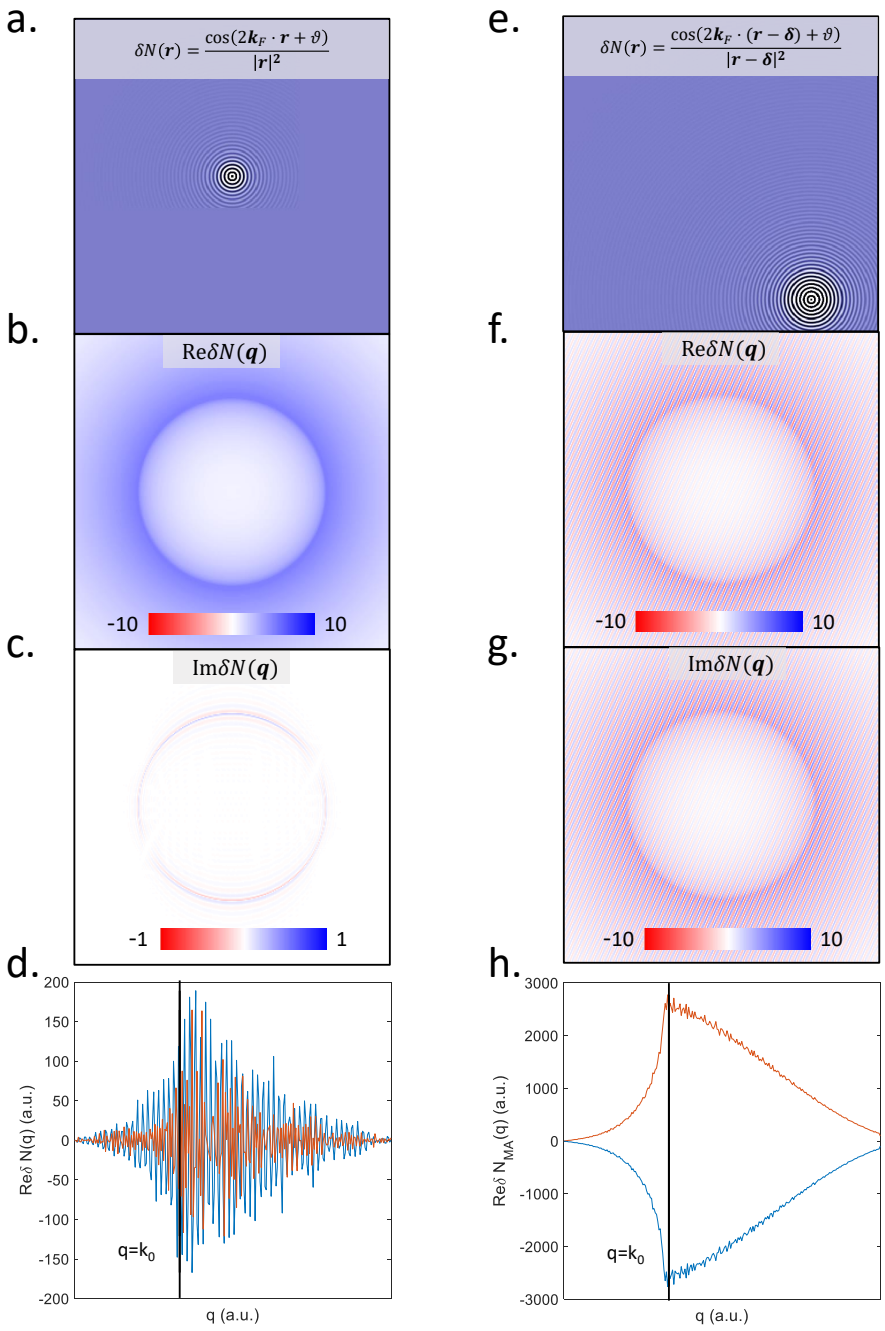

Figure 5.2: Effect of a shift of the origin on Fourier transform. a) Simulated Friedel oscillations from an atomic defect at the origin. b) The real part of Fourier transform of a) c) The imaginary part of Fourier transform of a) d)The azimuthally integrated real part plotted for $\vartheta = 0, \pi$ and $\vartheta = \pi$. e) Simulated Friedel oscillations from an atomic defect with a shift $\boldsymbol{\delta}$ from origin. f) The real part of Fourier transform of e) g) The imaginary part of Fourier transform of e) h) The azimuthally integrated real part of Fourier transform of e)

5.2.2 Treating the Pathology using Multi-Atom Fourier Transform

In the problem, lies the cure as some wise person would have said! We look at the eq. (5.3) describing the pathology we discussed in the previous section.

$$\mathcal{F}\psi(\mathbf{r}+\boldsymbol{\delta}) = e^{-i\mathbf{q}\cdot\boldsymbol{\delta}}\psi(\mathbf{q})$$

If we know $\boldsymbol{\delta}$ with enough precision and accuracy (this is where our SI-STM technology described in Ch. 2 at Cornell are crucial! Lawler-Fujita algorithm, wherever possible, can also help a great deal to register the locations of the defects with picometer precision [92, 32, 93] as described in sec. 5.3.1), Fourier transform of the BQPI with atomic defect centered at $\boldsymbol{\delta}$, $\mathcal{F}\delta N(\mathbf{r}+\boldsymbol{\delta})$ can yield the Fourier transform of the BQPI with the atomic defect shifted to be centered at origin $\delta N^S(\mathbf{q})$ using accurately recorded $\boldsymbol{\delta}$ as

$$\delta N^S(\mathbf{q}) = e^{i\mathbf{q}\cdot\boldsymbol{\delta}}\mathcal{F}\delta N(\mathbf{r}+\boldsymbol{\delta}) \tag{5.5}$$

This equation essentially performs a shift of origin by $-\boldsymbol{\delta}$ using periodic boundary conditions and is known as *shift theorem* of the Fourier transform. We demonstrate the effect of shift theorem in Fig. 5.3. Fig. 5.3a shows a topograph recorded on FeSe. We are interested in the dumb-bell shaped atomic defects, which are vacancies due to missing Fe atoms. We denote the center of one of them by a red cross. We apply shift theorem as outlined in eq. (5.5) to this topograph, taking $\boldsymbol{\delta}$ as the coordinates of this atomic defect which gives the topograph in q-space. Then we inverse Fourier Transform this back to real-space and the resulting topograph is shown in Fig. 5.3b. It can be seen that the impurity denoted by the red cross in Fig. 5.3a has moved to the center with periodic boundary conditions. This is what the shift theorem achieves.

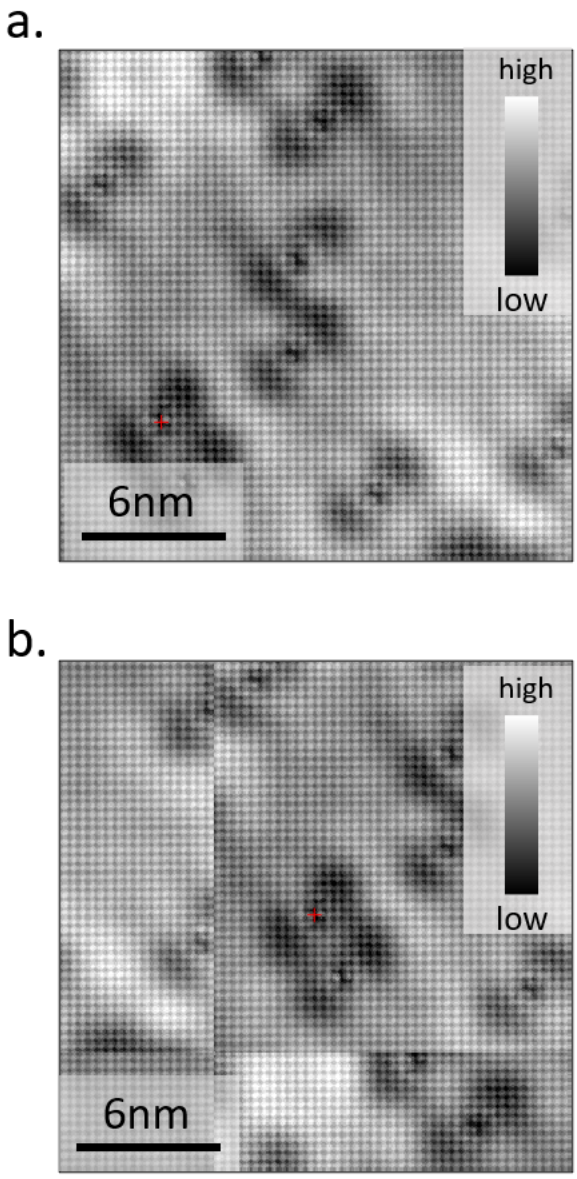

Figure 5.3: Centering the impurity in FOV with shift theorem of Fourier transform. a) The topograph showing an impurity with a red cross. b) Inverse Fourier transform showing the topograph after applying the shift theorem to a) using the impurity coordinate shown by a red cross in a). It can be seen that the impurity denoted by red-cross is moved to the center now with periodic boundary conditions.

Now for a density of states map $\delta N(\mathbf{r})$ with multiple defects at $\mathbf{R_1}, \mathbf{R_2}, \ldots, \mathbf{R_N}$, with a Fourier transform $\delta N(\mathbf{q})$, we define a quantity we call a multi-atom Fourier transform $\delta N_{\mathrm{MA}}(\mathbf{q})$, where we apply the shift theorem to each atomic defect and then add them up.

$$\delta N_{\mathrm{MA}}(\mathbf{q}) = \sum_{i=1}^{N} e^{i\mathbf{q}\cdot\mathbf{R_i}} \delta N(\mathbf{q}) \tag{5.6}$$

This essentially ensures that the Fourier transform of BQPI at the origin, with no rapid oscillations (eq.(5.2)) gets added in phase, while oscillations due to the other atomic defects being random, are severely suppressed. The success of this technique is demonstrated in Fig. 5.4. A simulation of Friedel oscillations from N=50 atomic defects, $\delta N(\mathbf{r}) = \sum_{i=1}^{50} \frac{\cos(\mathbf{k_0}\cdot(\mathbf{r}-\mathbf{R_i})+\vartheta)}{k_0|\mathbf{r}-\mathbf{R_i}|} e^{-\kappa|\mathbf{r}-\mathbf{R_i}|}$ is shown in Fig. 5.4a. The real and imaginary part of the Fourier transform $\delta N(\mathbf{q})$ show rapid oscillations eq. (5.4) as can be seen in top half of Fig. 5.4b. The azimuthally integrated Re $\delta N(\mathbf{q})$ shows a peak at $q = k_0$, but the oscillations are so dominating that determining the sign of Re $\delta N(\mathbf{q})$ is hopeless and this is reflected in the plots with $\vartheta = 0, \pi$ which cannot be clearly distinguished. This problem is remedied by calculating the multi-atom Fourier transform $\delta N_{\mathrm{MA}}(\mathbf{q})$ (eq. (5.6)) whose real and imaginary parts are shown in the bottom half of Fig. 5.4. It can be seen that with this technique, the real part has a higher and deterministic sign in the signal and the imaginary part, which is noise, is much reduced. This can be compared with the real and imaginary parts of the Fourier transform of the ideal case of a single origin-centered atomic defect shown in Fig. 5.3b and c. The azimuthally integrated Re $\delta N_{\mathrm{MA}}(\mathbf{q})$ shows peak at $q = k_0$ as expected and a deterministic sign which enables distinction in $\vartheta = 0, \pi$. Comparing this to the ideal case of the single origin-centered atomic defect results in Fig. 5.3d, we can see that this definition of multi-atom Fourier transform in eq. (5.6) indeed treats the pathology of the origin shifts and enables the recovery of the sign of the real part of

the Fourier transform which is essential to apply HAEM scheme (eq. (3.33)). A MATLAB script to demonstrate this process is provided in the Appendix F.2.

5.3 Multi-Atom HAEM analysis

We have described the formalism of the HAEM scheme and how to use it for a single atomic defect in Chapter 2 of this thesis. Here, we describe the new technique we developed to apply HAEM to multiple atomic defects which is based on the concepts discussed in the previous section. This extends the applicability of HAEM for a broader range of materials and also increases signal and -space resolution as one can have multiple impurities contributing to the BQPI signal in-phase and a larger FOV. Since the choice of origin affects the Fourier transform greatly (as described in sec. 5.2.1), we first need to start with a way to make sure that the atomic impurity coordinates are perfect. This is achieved by a state-of-art STM (Ch.2) and if possible, by applying a technique developed in our research group for picometer scale registration [92, 32, 93] of recorded atoms in a topograph to a perfect crystal lattice. We call this technique Lawler-Fujita (LF) correction based on its inventors and our colleagues. In this section, we first describe the LF correction and then we describe the steps involved in a MAHAEM analysis procedure.

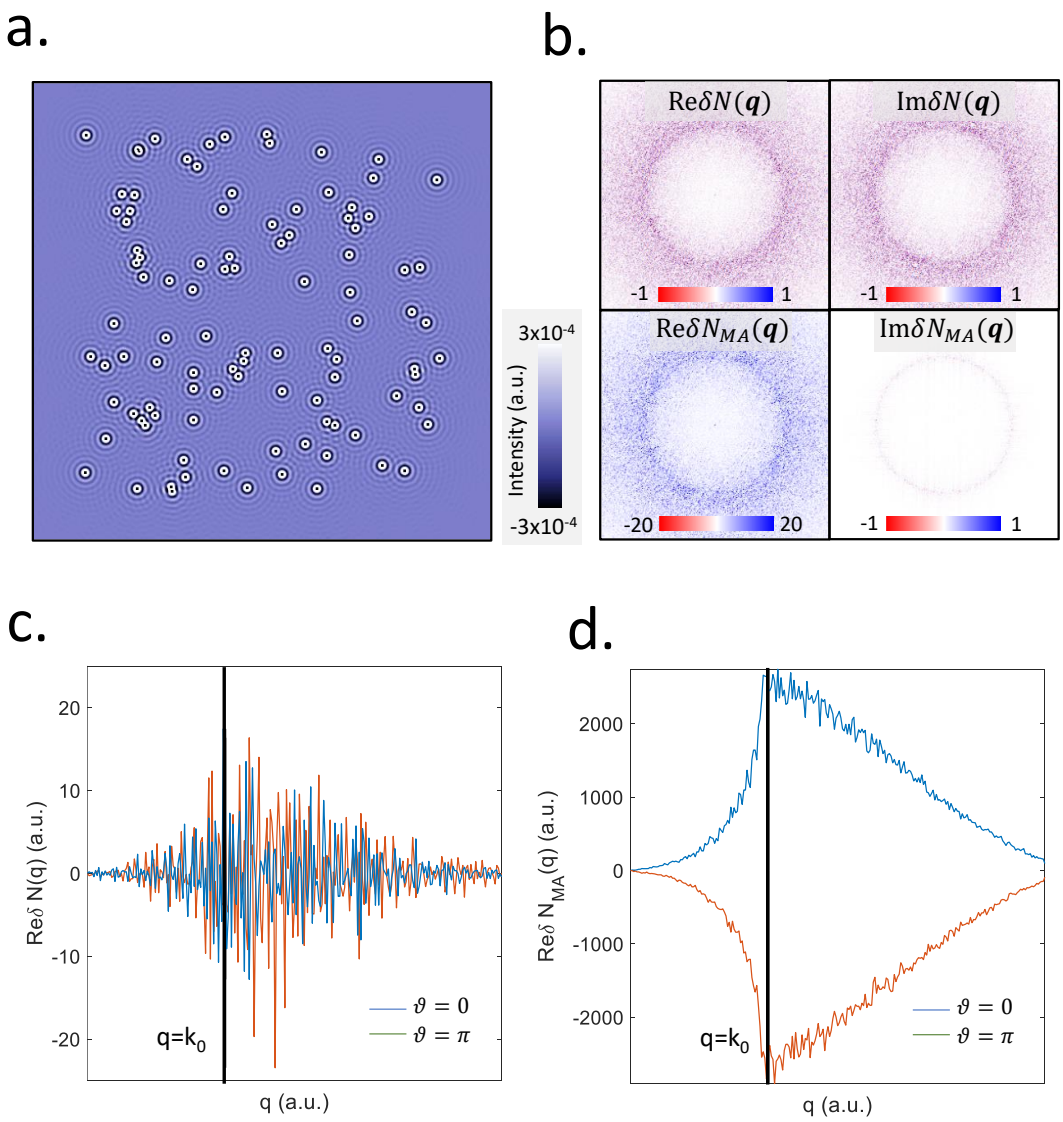

Figure 5.4: Recovering the phase of the BQPI using multi-atom Fourier transform. a) Simulated Friedel oscillations from N=50 atomic defects in real space. b) Top left: Real part of Fourier Transform Re $\delta N((q))$. Top right: Imaginary part of Fourier Transforms Im $\delta N((q))$. Bottom left: Real part of multi-atom Fourier transform Re $\delta N_{\mathrm{MA}}((q))$ calculated using eq. (5.6). Bottom right: Imaginary part of multi-atom Fourier transform "Im $\delta N_{\mathrm{MA}}((q))$. c) Re $\delta N((q))$ for $\vartheta = 0, \pi$, integrated azimuthally from top left in b. d) Re $\delta N_{\mathrm{MA}}((q))$ for $\vartheta = 0, \pi$, integrated azimuthally from bottom left in b.

5.3.1 LF Correction: Atomic Scale Registration to a Perfect Crystal Lattice

An atomic scale perfect topograph with orthogonal unit cell vectors **a** and **b** recorded by STM can be represented as:

$$T(\mathbf{r}) = T_0 \left[\cos\left(\mathbf{Q_a} \cdot \mathbf{r}\right) + \cos\left(\mathbf{Q_b} \cdot \mathbf{r}\right)\right] \tag{5.7}$$

where $\mathbf{Q_a} = (Q_{ax}, Q_{ay})$ and $\mathbf{Q_b} = (Q_{bx}, Q_{by})$ are the two Bragg wavevectors at which the atomic modulation occurs. In a real experiment, the ideal $T(\mathbf{r})$ may suffer from a slowly varying distortion [92, 32, 93] $\mathbf{u}(\mathbf{r})$. Hence the topographic image recorded in a real experiment can be written as:

$$\tilde{T}(\mathbf{r}) = T_0 \left[\cos\left(\mathbf{Q_a} \cdot \mathbf{r} + \mathbf{u}(\mathbf{r})\right) + \cos\left(\mathbf{Q_b} \cdot \mathbf{r} + \mathbf{u}(\mathbf{r})\right)\right] \tag{5.8}$$

It can be seen that this distortion has led to an additional phase at location **r** given by:

$$\begin{pmatrix} \theta_a(\mathbf{r}) \\ \theta_b(\mathbf{r}) \end{pmatrix} = \begin{pmatrix} Q_{ax} & Q_{ay} \\ Q_{bx} & Q_{by} \end{pmatrix} \begin{pmatrix} u_x(\mathbf{r}) \\ u_y(\mathbf{r}) \end{pmatrix} = \mathbf{Q}\mathbf{u}(\mathbf{r}) \tag{5.9}$$

This allows us to solve for the displacement field $\mathbf{u}(\mathbf{r})$ as:

$$\mathbf{u}(\mathbf{r}) = \mathbf{Q}^{-1} \begin{pmatrix} \theta_a(\mathbf{r}) \\ \theta_b(\mathbf{r}) \end{pmatrix} \tag{5.10}$$

To find θ_i, we employ a computational lock-in technique in which the topograph, $T(\mathbf{r})$ is multiplied by reference sine and cosine functions with period $\mathbf{Q_a}$ and $\mathbf{Q_b}$. The resulting four images are filtered to retain only the **q**-space regions within the radius $\delta q = \frac{1}{\lambda}$ of the four Bragg peaks. The magnitude of λ is chosen to capture only the relevant image distortions. This procedure results in retaining the local phase information $\theta_a(\mathbf{r}), \theta_b(\mathbf{r})$ that quantifies the local displacement

from perfect periodicity:

$$X_i(\mathbf{r}) = \cos\theta_i(\mathbf{r}), \quad Y_i(\mathbf{r}) = \sin\theta_i(\mathbf{r}) \tag{5.11}$$

Dividing the appropriate pair of images leads allows one to extract $\theta_i(\mathbf{r})$

$$\theta_i(\mathbf{r}) = \tan^{-1}\frac{Y_i(\mathbf{r})}{X_i(\mathbf{r})} \tag{5.12}$$

Once we have $\theta_i(\mathbf{r})$, we get the displacement field $\mathbf{u}(\mathbf{r})$ using eq. (5.10). The value of recorded topograph $\tilde{T}(\mathbf{r})$ as given by eq. (5.8) can now be registered to a perfect ideal lattice as given by eq. (5.7) using:

$$T(\mathbf{r}) = \tilde{T}(\mathbf{r} - \mathbf{u}(\mathbf{r})) \tag{5.13}$$

5.3.2 Steps Involved in MAHAEM Analysis

We start by recording the coordinates $\mathbf{R}_i = (x_i, y_i)$ of all the impurities from the topograph or the G-map. If resolution permits, this should be done on an LF-corrected map following the procedures described in the previous section 5.3.1. One must be careful to check if there is a relative shift of coordinates from topograph to G-map. This can occur is the tip is not well-rested and the spectroscopic measurements take relatively larger time than recording the coordinates. In case of a relative shift, the coordinates from the G-map(LF corrected, if possible) must be used as it contains the BQPI scattering information we want to analyze. From the recorded and corrected $g((r), E)$, we get the Fourier transform $g(\mathbf{q}, E)$ We then calculate the shifted Fourier transforms $g_i^S(\mathbf{q}, E)$ for each impurity i as described in eq. (5.5).

$$g_i^S(\mathbf{q}, E) = \sum_{i=1}^{N} e^{i\mathbf{q}\cdot\mathbf{R_i}} g(\mathbf{q}, E) \tag{5.14}$$

These shifted Fourier transforms are shifted with periodic boundary conditions. If we look at Fig. 5.3, we notice that this leads to discontinuous boundaries in the image. This can lead to spurious features in Fourier transforms. To get rid of these edge discontinuities, we perform the inverse Fourier transform of the shifted Fourier transform $g_i^S(\mathbf{q}, E)$ and multiply it by a sinusoidal window, which makes the values go smoothly to zero on edges under a sinusoidal envelop. For this purpose, if we have a $n_x \times n_y$ image, we define linearly spaced vectors $\theta_{x/y} = [0, \pi]$ with $n_{x/y}$ points. The sinusoidal window is defined as:

$$\text{sinw} = \sin(\theta_x)^T \sin(\theta_y) \tag{5.15}$$

Using this sinusoidal window to smoothen edge discontinuities in the inverse Fourier transform $g_i^S(\mathbf{r}, E)$ of the shifted Fourier transform $g_i^S(\mathbf{q}, E)$, we get windowed and shifted data $g_i^{WS}(\mathbf{r}, E)$as:

$$g_i^{WS}(\mathbf{r}, E) = \text{sinw} \cdot g_i^S(\mathbf{r}, E) \tag{5.16}$$

where $\cdot$ denotes the elementwise multiplication. The Fourier transform of this quantity finally, gives us the clean Fourier transform $g_i(\mathbf{q}, E)$ for a single impurity. This whole sequence of operations to get $g_i(\mathbf{q}, E)$ from the recorded data $g(\mathbf{r}, E)$ can be described in a single equation as:

$$g_i(\mathbf{q}, E) = \mathcal{F}\left(\text{sinw} \cdot \mathcal{F}^{-1}\left(e^{i\mathbf{q}\cdot\mathbf{R_i}}\mathcal{F}\, g(\mathbf{r}, E)\right)\right) \tag{5.17}$$

From these clean shift corrected single impurity Fourier transforms $g_i(\mathbf{q}, E)$, we can now define the multi-atom Fourier transforms as defined in eq. (5.6):

$$g_{MA}(\mathbf{q}, E) = \sum_{i=1}^{N} g_i(\mathbf{q}, E) \tag{5.18}$$

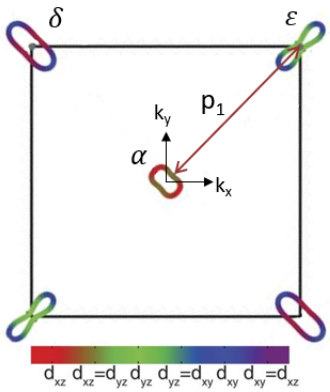

Figure 5.5: The inter-pocket scattering in FeSe to be studied for sign using HAEM.$\mathbf{q} = \mathbf{p_1}$ is the scattering vector which we will integrate over to get the sign from HAEM.

From these multi-atom Fourier transforms, which we have shown to be equivalent to a single origin-centered atomic-defect, we are now in a position to calculate the key HAEM indicator quantity $\rho^{-}(\mathbf{q}, E)$ in terms of $g_{\mathrm{MA}}(\mathbf{q}, E)$

$$\rho^{-}(\mathbf{q}, E) = \mathrm{Re}\; g_{\mathrm{MA}}(\mathbf{q}, E) - \mathrm{Re}\; g_{\mathrm{MA}}(\mathbf{q}, -E) \tag{5.19}$$

5.4 Results on FeSe

To test whether this scheme for $\rho^{-}(\mathbf{q}, E)$ works, we apply it to FeSe, where a single impurity calculated $\rho^{-}(\mathbf{q}, E)$ was studied earlier [39]. For details of the problem itself, please refer to [39] or refer to section 3.5.1 for a quick overview. In Fig. 5.5, we show the scattering vector between the hole pocket α and the electron pocket ϵ in the k-space labeled as p_1.

To test the validity of our technique, we compare the results obtained from our analysis of this scattering using multiple atomic defects with the results

obtained from the single atomic defect HAEM analysis performed in [39]. The scattering under study appears as a feature in BQPI which is denoted by a circle at $\mathbf{q} = \mathbf{p_1}$ in Fig. 5.6b and d. G_1 and G_2 denote the Bragg scattering vectors. Single impurity $\rho^-(\mathbf{q}, E)$ integrated over the circle is plotted in Fig. 5.6c (black dots) along with theoretical predictions for $s_\pm$(black curve) and s_{++} (red curve). The data agrees with the $s_\pm$ predictions and satisfies the two characteristics which a sign-changing gap possesses from HAEM theory i) the $\rho^-(\mathbf{q}, E)$ does not change sign within the superconducting gap and ii) there is a peak at approximately $\approx \sqrt{\Delta_e \Delta_h} \approx 2$ meV. We set out to test our algorithm to reproduce these results by recording $\delta N(\mathbf{q}, E)$ in larger FOV with multiple atomic defects. Fig. 5.6d shows the topograph of the FOV we used for the application of our multiple impurity algorithm. The measurement parameters for the topographs and the BQPI maps were the same as in [39]. We calculate the multi-atom HAEM signal $\rho^-_{\mathrm{MA}}(\mathbf{q}, E)$ as described in section 5.3 for all the impurities visible in the FOV and integrate it in a circle as shown in a representative $\rho^-(\mathbf{q}, E)$ layer at E=1.05 meV in Fig. 5.6e. We plot $\rho^-(\mathbf{q}, E)$ using our algorithm in Fig. 5.6f. We can see that our scheme, despite having not chosen a FOV centered on a single atomic defect, leads to a very good match with the $\rho^-(\mathbf{q}, E)$ calculated using single impurity FOV as shown in Fig. 5.6c and also the theoretical curve for $s_\pm$, which is overlaid on the plot. Our multi-atom HAEM signal $\rho^-_{\mathrm{MA}}(E)$ shows both the characteristics of no sign-change and peak at the right position within the gap, which is expected from HAEM theory for a sign-changing gap. This establishes the validity of our technique for multiple atomic defects. We use it to determine the sign of the superconducting gap on LiFeAs next, which is a subject of contemporary interest.

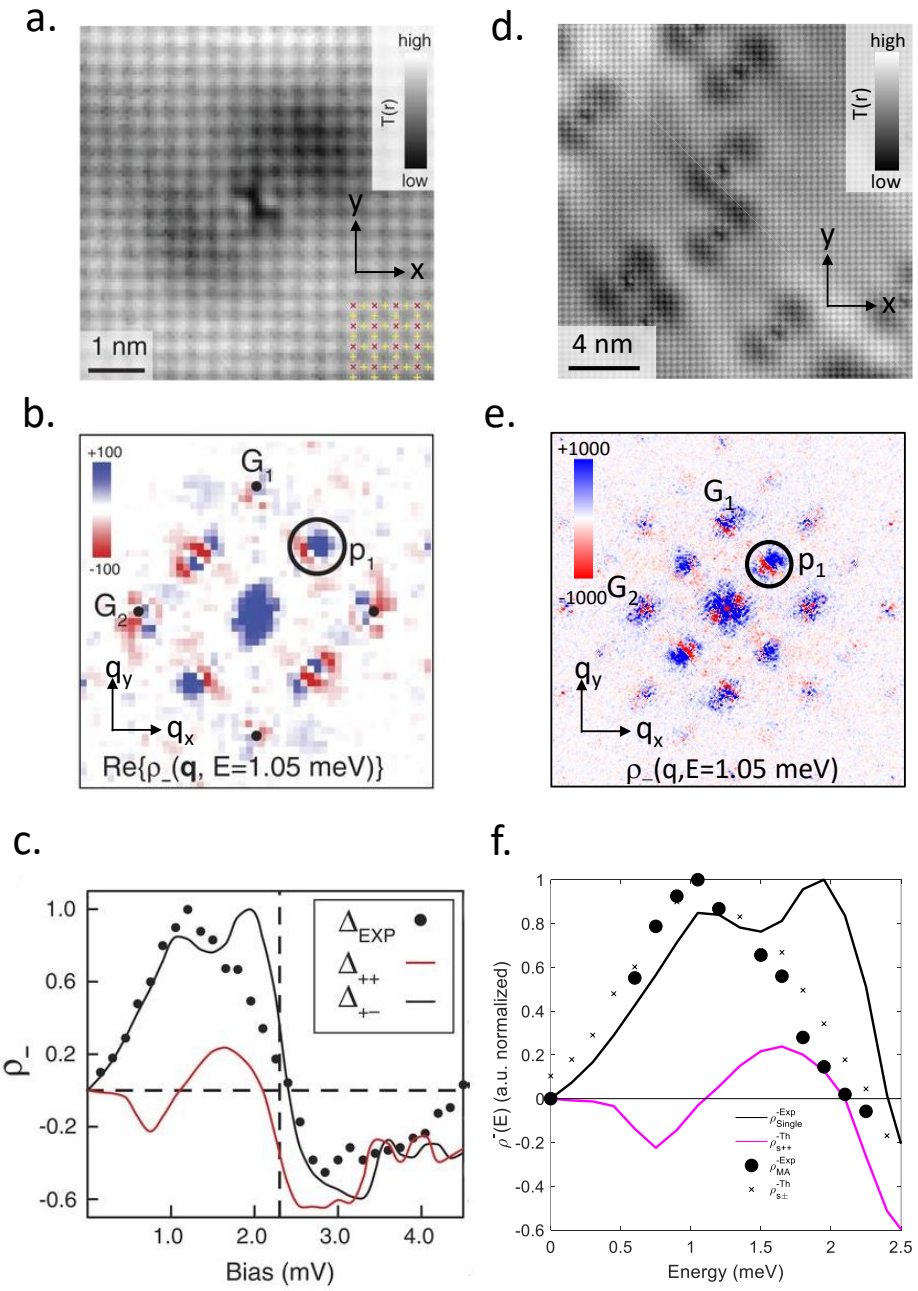

Figure 5.6: Comparison of multi-atom HAEM results with previously studied single impurity results. a) Topograph recorded for a single atomic defect centered FOV used for HAEM analysis in [39] b) The $\rho^{-}(\mathbf{q}, E)$ calculation for the FOV in a). c) The $\rho^{-}(E)$ summed over the circle shown in b. d) The FOV used for analysis using our technique with multiple atomic defects. e) The $\rho^{-}(\mathbf{q}, E)$ calculation using our multi-atom HAEM technique for FOV in a). f) The $\rho^{-}_{\mathrm{MA}}(E)$ summed over the circle shown in d) and the theoretical prediction curves for s_{++} gap symmetry (pink) and $s_{\pm}$ gap symmetry (black). Figures a to c are reproduced from [39]

5.5 Iron Based Superconductivity and LiFeAs

Discovered in 2008 [94], iron-based superconductors opened doors for a new class of unconventional superconductors [95]. The question of gap symmetry in FeSc is inherently more complex than cuprates, where a d-wave gap is fairly well established for a variety of material classes and dopings [96]. This complexity arises from the presence of multiple Fe d-orbitals on the Fermi surface. These d-orbitals lead to small electron and hole like pockets which are quite sensitive to pressure and doping (for a review of these experiments, see section IV-B in [95]). General arguments based on this sensitivity have been presented to argue for a sign-changing gap structure of $s_{\pm}$ symmetry for Fe-based superconductors [97]. This is also considered a natural way to create pairing glue out of repulsive Coulomb interactions for the ground state of iron-pnictides based on the Fermi surface structure [98, 99]. However, it was also discovered that due to multi-orbital nature and doping or pressure causing changes in the Fermi surface where only electron or hole pocket may be present, a competition exists between d-wave and s-wave states. These complex but interesting possibilities lead to multiple possibilities for superconducting gap symmetry as shown in Fig. 5.7. Also it must be noted that since the s-symmetry does not distinguish between angular momentum, experiments like corner-junction Josephson experiments are not possible. In general due to sample quality issues, the Josephson experiments on this class of materials have been challenging. Hence the experimental probes for resolving the issue of gap sign in iron-based superconductors are very valuable for understanding the gap symmetry and eventually the pairing mechanism.

LiFeAs has a special place among iron-based superconductors [100].

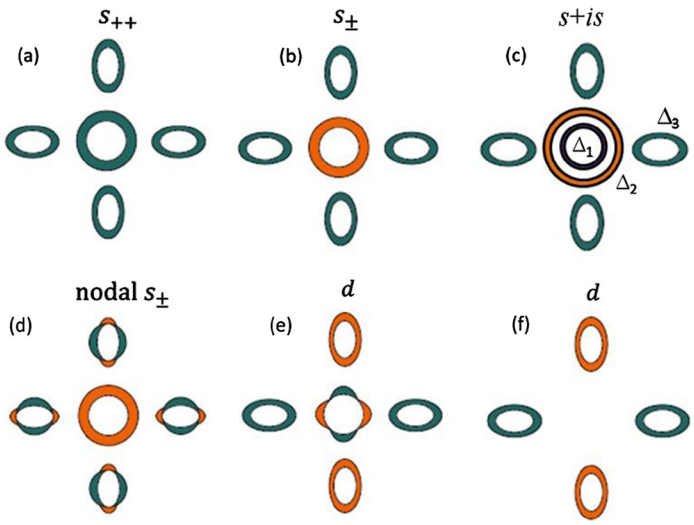

Figure 5.7: Possible order parameters for iron-based superconductors. The different colors represent different signs. The circular pockets in the center are the hole pockets and elliptical pockets at X/Y points are electron pockets.

Fig. 5.8a shows the lattice structure of LiFeAs. STM topography records the As or Li atoms on the top of the layer as shown in Fig. 5.8. The dumbbell-shaped impurities are missing Fe atoms. Fig. 5.8c shows the Fermi surface of LiFeAs calculated using a tight-binding fit [101, 102] to the STM-data [46]. The Fermi surface consists of three hole pockets h_1,h_2 and h_3 around Γ-point and two electron pockets e_1 and e_2 around X-point. The hole pockets around Γ-point on the Fermi surface (FS) revealed by angle-resolved photoemission spectroscopy (ARPES) [103], and spectroscopic imaging scanning tunneling microscope (SI-STM) [46] are much smaller as compared 122 iron-based superconductors. Local density approximation (LDA) and dynamical mean-field theory (DMFT) calculations have attributed the small size of hole pocket to stronger electron-electron correlation in this material. The superconducting gap reported by both ARPES [103] and SI-STM [46] is substantially anisotropic with fourfold symmetry. For a $s_{\pm}$ pairing generally expected for iron-based superconductors, if both electron and hole pockets are present [104], the pairing arises from spin-

fluctuation which is enhanced by nesting between electron and hole pockets. Due to the observed small hole pockets due to electron correlations and resulting weak magnetic fluctuations, the picture of a $s_{\pm}$ gap in LiFeAs is a matter of discussion [105]. It has a much higher impurity density hence provides a perfect testbed for our new technique to solve an important issue.

5.6 Multi-Atom HAEM Analysis on LiFeAs

To figure out the sign of the superconducting gap, we wish to analyze the interband scattering between the electron band and the hole band. Fig. 5.10a shows the Fermi surface with orbital weights and shows the hole pockets around the Γ-point and electron pockets around X-point in the Brillouin zone. From the available STM [46] and ARPES [103] data on the superconducting state for this material, we fit the orbital gaps and calculate the theoretical BQPI pattern which is shown in Fig. 5.10b. The electron-hole scattering leads to a "horn"-shaped feature which is encircled and this scattering vector is labeled $\mathbf{q_{eh}}$. The theoretical prediction for the HAEM quantity $\rho^{-}(E)$ (eq.(3.33)) is also made by imposing the sign of the gap by hand and the resulting theoretical curves are shown in Fig. 5.10c.

For putting this theoretical HAEM model to test we performed BQPI imaging at T=1.2K in a 74x74 nm FOV with a resolution of 512x512 pixels which has multiple impurities as shown in Fig. 5.8b. The tunneling spectrum measured using our STM-tip consists of two gaps corresponding to Δ_1 = 5.3meV and Δ_2 = 2.6meV as shown in Fig. 5.8d. The electron-hole scattering leads to a horn-shaped feature in the BQPI as expected from the theoretical model and in-

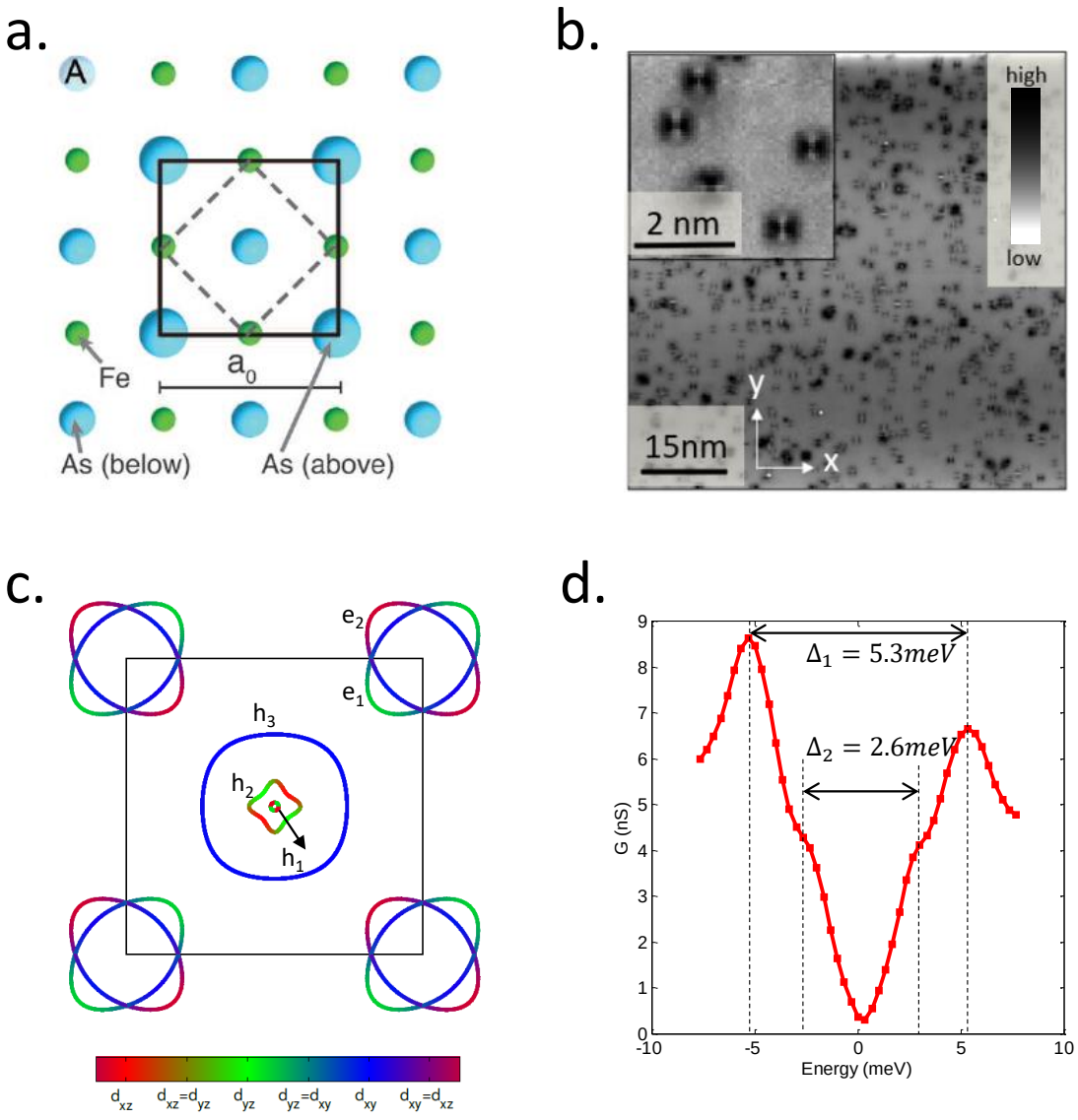

Figure 5.8: a) The lattice structure of LiFeAs with 1-Fe (2-Fe) unit cell showed with dashed (solid) lines. b) Topograph recorded on LiFeAs with multiple atomic defects. The inset shows a zoomed version of the atomic defects. c) The Fermi surface of LiFeAs showing 3 hole pockets h_1, h_2 and h_3 around Γ-point and 2 electron pockets e_1 and e_2 around X-point in a 2-Fe zone. d) The tunneling spectrum in the superconducting state on LiFeAs seems to suggest two gaps Δ_1 = 5.3 meV and Δ_2 = 2.6 meV

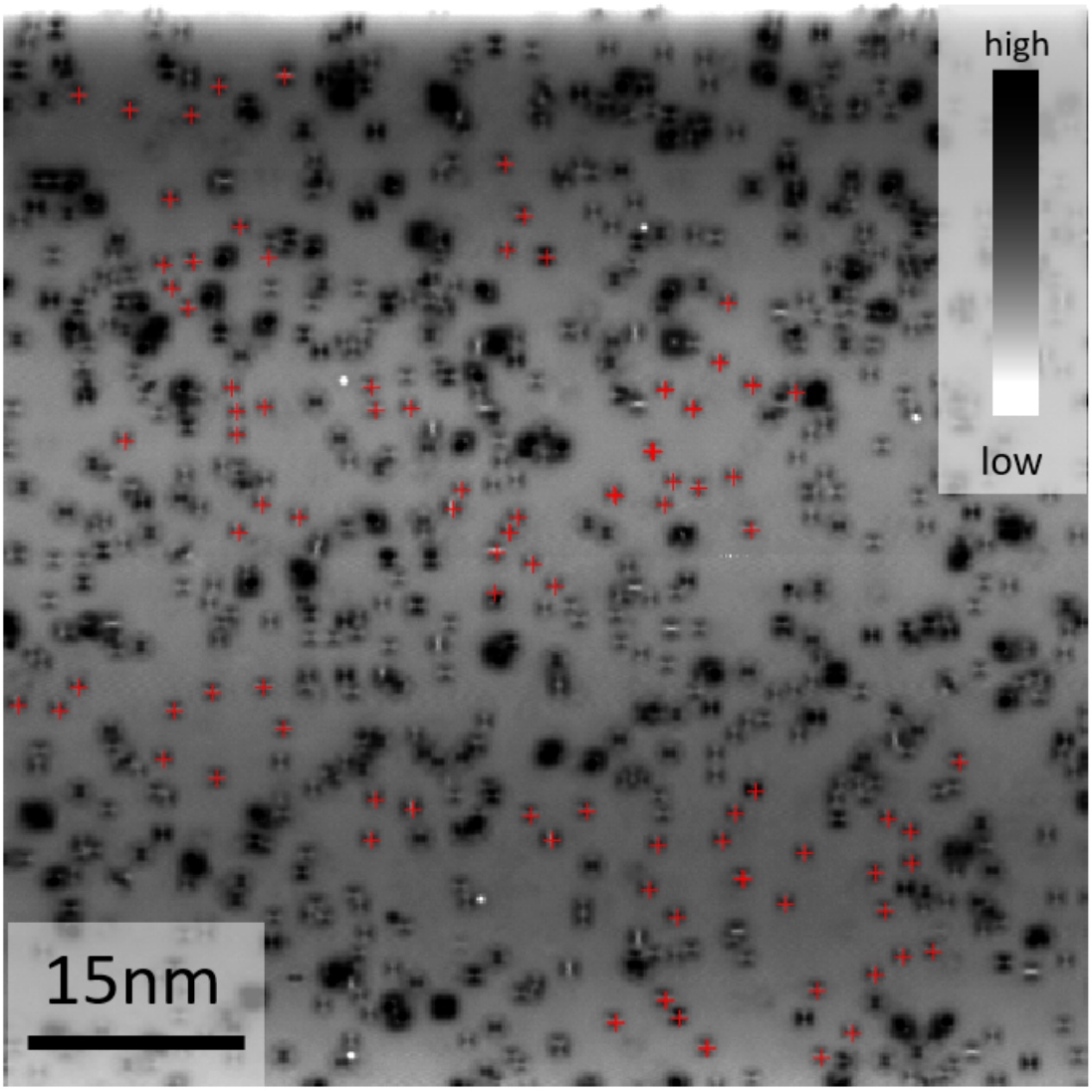

Figure 5.9: Atomic defects used in multiple atom HAEM analysis.

dicated by a circle at the same location $\mathbf{q_{eh}}$ in the experimental Fourier transform of BQPI in Fig. 5.10d. We calculate the multi-atom $\rho^{-}_{\mathrm{MA}}(\mathbf{q}, E)$ with the procedure we introduced in this work (eq. (5.19)) for N=100 impurities. Our analysis employs the dumb-bell shaped atomic defects, which are missing Fe atoms. We show the defects involved in our analysis by red crosses in Fig. 5.9. The resulting image at a representative subgap energy E=3.33 meV is shown in Fig. 5.10e

which has been symmetrized for better visualization, though all the features visible here are present in the raw data. We take the average of the $\rho^{-}_{\mathrm{MA}}(\mathbf{q}, E)$ signal in the region shown by a circle which is at the same location $\mathbf{q_{eh}}$ as in Fig. 5.10b and d, which captures the interband scattering between hole-pocket and electron-pocket. This averaged $\rho^{-}_{\mathrm{MA}}(E)$ is plotted as a function of energy in Fig. 5.10d. The experimental $\rho^{-}_{\mathrm{MA}}(E)$ calculated for the interband scattering between electron and hole pocket shows a good agreement with the overlaid theoretical curve for $s_{\pm}$. The sign of ρ^{-} doesnt change for the energy values within the superconducting gap and ρ^{-} peaks at the energy $\sim \sqrt{\Delta_1 \Delta_2}$, both characteristics of a sign-changing gap (section 3.5). Thus we conclude that the gap symmetry of superconducting state in LiFeAs is $s_{\pm}$.

5.7 Summary and Conclusions

In conclusion, we have introduced a novel multi-atom HAEM scheme which extends the HAEM analysis to multiple atomic defects. We test our technique on FeSe and reproduce the results which were achieved with the original HAEM scheme [40]. Then we set out to use this technique to determine the superconducting gap symmetry of LiFeAs, which is of contemporary interest because small FS pockets cast a shadow on the nesting enhanced spin fluctuations mechanism which leads to $s_{\pm}$ pairing. Using our technique, we show that the superconducting gap on LiFeAs changes sign between hole and electron pocket, implying that the superconducting gap symmetry is indeed $s_{\pm}$. More disordered superconductors can be studied with this multi-HAEM now with better signal to noise and higher k-space resolution due to possibility of using multiple atomic defects in a large FOV. This advancement offered by multi-atom HAEM

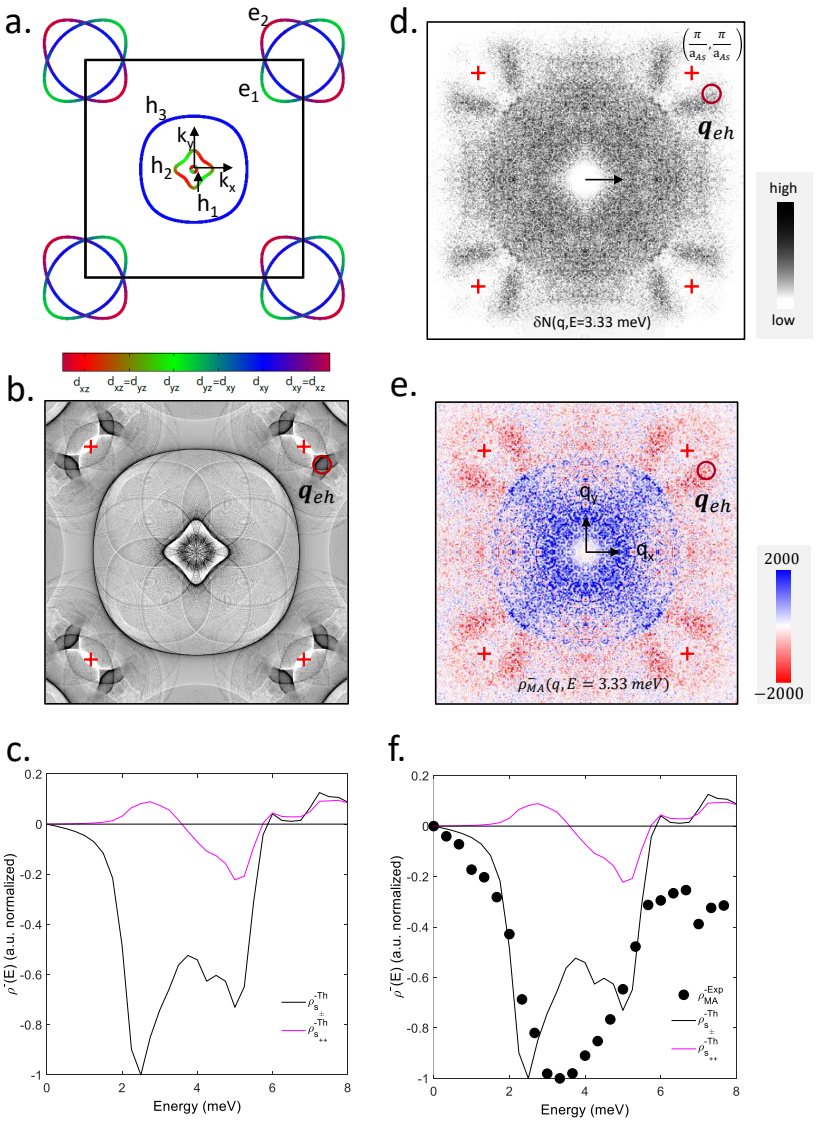

Figure 5.10: Multi-atom HAEM analysis on LiFeAs. a) The Fermi surface with the orbital weights showing the electron pocket at Γ-point and hole pockets at X-points. b) The theoretical BQPI calculated from fits to normal state and superconducting state experimental data as mentioned in the text. The circle indicates the electron hole scattering which appears at the scattering vector $\mathbf{q_{eh}}$. Red crosses denote $(\pm\pi/a, \pm\pi/a)$ points. c) The theoretical prediction curves for $\rho^{-}(E)$ from the experimentally fitted parameters and gap sign imposed by hand for s_{++} (pink) and $s_{\pm}$ (black) gap symmetry. d) The experimental BQPI pattern $\delta N(\mathbf{q}, E = 3.33$ meV) recorded in the FOV with multiple impurities as shown in Fig. 5.8b. The scattering between electron and hole at $\mathbf{q_eh}$ is observed and encircled at the same location as in b). Red crosses denote $(\pm\pi/a, \pm\pi/a)$ points. c) The multi-atom HAEM indicator quantity $\rho^{-}_{\mathrm{MA}}(\mathbf{q}, E)$ calculated using (eq. (5.19)). The circle indicates the electron-hole scattering at $\mathbf{q_{eh}}$, same as in b) and d). Red crosses denote $(\pm\pi/a, \pm\pi/a)$ points. d) The $\rho^{-}_{\mathrm{MA}}(E)$ calculated by summing over the encircled region in c) (black dots), which contains the electron-hole scattering and the theory curves (solid) for $s_{\pm}$ (black) and s_{++} (red) overlaid.

makes BQPI, a powerful tool for sign-determination of superconducting gap in a broader range of superconductors.

CHAPTER 6

SUMMARY AND OUTLOOK

In this thesis, we have presented advanced quasiparticle interference imaging to address two important contemporary problems of superconductivity.

By imaging the quasiparticles at T=90 mK, in Sr_2RuO_4, we have established that the major gap lies on the $\alpha : \beta$ bands and it has eight nodes, all lying within 0.05 radians of the ΓX line. The simplest conclusion agreeing with our experimental data, and consistent with other experiments is a B_{1g} ($d_{x^2-y^2}$-wave) gap symmetry. By developing a novel multi-atom quantum phase-sensitive technique on LiFeAs, we have shown that the superconducting order parameter changes sign between the electron and hole pockets, implying that the superconducting gap symmetry is $s_{\pm}$ in LiFeAs.

These experimental facts are crucial ingredients to come up with an explanation for why pairing occurs in these materials. These facts are helpful in ruling out some of the existing theories and in constraining the future theories. The understanding of pairing in materials eventually helps to come up with new recipes and hopefully have a superconductor with desired properties.

In the future, we hope that the millikelvin STM and the analysis techniques presented in this thesis will be used to solve the problems in heavy-fermion superconductivity [106] and especially to look at a recent candidate of spin-triplet topological superconductivity UTe_2 [107].

The novel multi-atom HAEM method will enable the gap sign to be determined on superconductors with higher disorder. The BQPI signal from multiple impurities can be summed now, to get a higher signal to noise ratio. If need be,

the scattering features in q-space features can be better resolved and analyzed as the FOV can be larger because the need for having only a single impurity in FOV is removed. We hope that this multi-atom HAEM technique will be widely used to settle the issue of symmetry in more superconductors.

APPENDIX A

GAUGE SYMMETRY

Gauge symmetry is an important concept in Physics and leads to an elegant presentation of many concepts. For a superconductor, the non-zero value of the macroscopic phase is the root of its fascinating macroscopic quantum properties. In this chapter, we describe the basic definitions and tools to deal with gauge symmetry in electrodynamics and quantum mechanics.

A.1 Gauge symmetry in Electrodynamics

Let us look at one of the most beautiful set of equations in Physics, the Maxwell equations:

$$\nabla \cdot \mathbf{E} = \frac{\rho}{\varepsilon_0} \tag{A.1}$$

$$\nabla \cdot \mathbf{B} = 0 \tag{A.2}$$

$$\nabla \times \mathbf{E} = -\frac{\partial \mathbf{B}}{\partial t} \tag{A.3}$$

$$\nabla \times \mathbf{B} = \mu_0 \mathbf{j} + \frac{1}{c^2}\frac{\partial \mathbf{E}}{\partial t} \tag{A.4}$$

Equation (A.2) here is divergence of a quantity being zero, and vector calculus identity [108] tells us that divergence of a curl is zero. Hence magnetic field can be written in terms of a *magnetic vector potential* as:

$$\mathbf{B} = \nabla \times \mathbf{A} \tag{A.5}$$

Another vector calculus identity [108] tells us that the curl of a gradient is also zero. Hence equation (A.3) can also be satisfied using this definition of magnetic

vector potential by using a scalar potential φ and writing $\mathbf{E}$ as

$$\mathbf{E} = \nabla\phi - \frac{\partial \mathbf{A}}{\partial t} \tag{A.6}$$

But this choice of φ and $\mathbf{A}$ are not unique for a given $\mathbf{E}$ and $\mathbf{B}$. Since curl of a gradient is always zero, we can transform the magnetic vector potential as $\mathbf{A} \mapsto \mathbf{A} + \nabla\alpha$, where $\alpha(\mathbf{r}, t)$ is a scalar field, without changing the magnetic field in (A.5). To make sure $\mathbf{E}$ is also unchanged, the scalar vector potential has to be transformed as $\phi \mapsto \phi - \partial_t\alpha/c$. This intrinsic ambiguity in choosing the electromagnetic potentials is known as *gauge symmetry* in electrodynamics. The transformations

$$\begin{aligned} \mathbf{A} &\mapsto \mathbf{A} + \nabla\alpha \\ \phi &\mapsto \phi - \frac{1}{c}\frac{\partial \alpha}{\partial t} \end{aligned} \tag{A.7}$$

are called *gauge transformation* and since the choice of α is arbitrary, all physical observables must be independent of α, which is referred to as being *gauge invariant*.

A.2 Gauge Symmetry in Quantum Mechanics

To include electrodynamics coupling in dynamics of a charged particle, momentum $\mathbf{p}$ is transformed as $\mathbf{p} \mapsto \mathbf{p} - eA/c$ [27]. The Schrödinger equation with this transformation looks like [27]

$$i\hbar\frac{\partial \psi}{\partial t} = -\frac{\hbar^2}{2m}\left(\nabla - i\frac{q\mathbf{A}}{c}\right)^2 \psi + (V + q\varphi)\psi \tag{A.8}$$

Now, if we gauge transform the electrodynamic fields using (A.7) and also locally rotate the phase of the wavefunction ψ by the gauge parameter $\alpha(\mathbf{r}, t)$ at each point in space time simultaneously as

$$\psi(\mathbf{r}, t) \mapsto e^{i\frac{q\alpha}{\hbar}}\psi(\mathbf{r}, t) \tag{A.9}$$

Then the Schrödinger equation becomes

$$i\hbar\frac{\partial\psi}{\partial t} - q\frac{\partial\alpha}{\partial t}\psi = -\frac{\hbar^2}{2m}\left(\nabla + i\frac{q\nabla\alpha}{\hbar} - i\frac{q\mathbf{A}}{c} - iq\frac{\nabla\alpha}{\hbar}\right)^2\psi + \left(V + q\varphi - \frac{q\partial\alpha}{\partial t}\right)\psi \tag{A.10}$$

It can be clearly seen that the α dependent terms drop out and we recover the original Schrödinger equation (A.8). Hence the quantum mechanics is invariant under a gauge transformation

$$\begin{aligned} \psi(\mathbf{r}, t) &\mapsto e^{i\frac{q\alpha}{\hbar}}\psi(\mathbf{r}, t) \\ \mathbf{A} &\mapsto \mathbf{A} + \nabla\alpha \\ \phi &\mapsto \phi - \frac{1}{c}\frac{\partial\alpha}{\partial t} \end{aligned} \tag{A.11}$$

Quantum mechanics, therefore, is said to possess a *local* $U(1)$ *gauge-symmetry*. Local because the phase of the wave-function can be rotated independently at each location, unlike weaker global symmetry where the phase of the wave-function can be rotated by a same fixed amount at each location. $U(1)$ because the gauge transformations belong to the group of 1-dimensional matrices $e^{i\theta}$.

A.3 Four-vector notation

We introduce four-vector notation [109] which will be convenient for following the future chapters. We follow the sign convention $(+, -, -, -,)$. Spacetime coordinates are written as $x^\mu = (t, \mathbf{x})$ where $\mu = 0, 1, 2, 3$. The derivatives with respect

to x^μ is written as ∂_μ. The scalar and vector potentials of electromagnetism are combined in a 4-vector as $(\varphi, -\mathbf{A})$. We follow Einstein's summation convention, which means that sum over the repeated indices are implied. We define the field-strength tensor

$$F_{\mu,\nu} = \partial_\mu A_\nu - \partial_\nu A_\mu \tag{A.12}$$

The electromagnetic fields can be recovered from the field strength tensor as

$$\begin{aligned} \mathbf{E_i} &= F_{0i} \\ \mathbf{B_i} &= \frac{1}{2}\epsilon_{ijk}F_{jk} \end{aligned} \tag{A.13}$$

where non-greek indices i, j, k represent the conventional space coordinates.

APPENDIX B

GAUGE SYMMETRY IN SUPERCONDUCTORS

Both BCS and Mean-field treatments show that the key-property of a superconductor is a well-defined phase or macroscopic phase coherence. We have seen that the BCS wavefunction (1.14) creates Cooper-pairs with well-defined phase due to complex numbers $u_{\mathbf{k}}$ and $v_{\mathbf{k}}$ creating each pair from the vacuum, however, the state is a superposition of all possible numbers of pairs and the number is not conserved as a result of number and phase uncertainties having a conjugate relationship. In the mean-field formalism, the mean-field order parameter $\Delta_{\mathbf{k}} = -\sum_{\mathbf{k}'} V_{\mathbf{k}\mathbf{k}'}\langle c_{-\mathbf{k}'\downarrow} c_{\mathbf{k}'\uparrow}\rangle$ has a nonzero expectation value in the superconducting state, which should only happen if the number is not conserved (For a number conserving state as a typical metal, such bilinear operators will have an expectation-value of zero due to Fermi-statistics). Due to the conjugate relationship between number and phase uncertainties [4], this again implies that the phase in the superconducting state is well-defined. Hence both formalisms are equivalent and the essence of the superconducting state is the phase. In this chapter we look at what are the implications of having this macroscopic phase and how it explains the fascinating electrodynamics properties of a superconductor.

A symmetry of a Hamiltonian is a transformation under which the Hamiltonian remains unchanged. The so called *gauge transformations* in quantum mechanics add a scalar phase to operators (see Appendix B) and given as:

$$\begin{aligned} c_{\mathbf{k}\sigma} &\mapsto e^{i\frac{e\alpha}{\hbar}} c_{\mathbf{k}\sigma} \\ c^{\dagger}_{\mathbf{k}\sigma} &\mapsto e^{-i\frac{e\alpha}{\hbar}} c^{\dagger}_{\mathbf{k}\sigma} \end{aligned} \tag{B.1}$$

It can be checked that the H_{BCS} in (1.12) is unchanged under this gauge trans-

formation [1]

However, in the superconducting state, the non-number conserving operator $\Delta_{\mathbf{k}} = -\sum_{\mathbf{k}'} V_{\mathbf{k}\mathbf{k}'} \langle c_{-\mathbf{k}'\downarrow} c_{\mathbf{k}'\uparrow} \rangle$ acquires a non-zero value. Due to the conjugate relationship between number and phase, this means that the superconductor has a well-defined phase and macroscopic phase coherence while the Hamiltonian is invariant under a gauge transformation. Under gauge transformation, superconducting order transforms as

$$\Delta \mapsto e^{i\frac{2e\alpha}{\hbar}} \Delta \tag{B.2}$$

Now, Δ has a phase as $\Delta = \Delta_0 e^{i\phi}$, where Δ_0 is a real positive number. Hence under gauge transformation (B.2), the superconducting phase will transform as

$$\phi \mapsto \phi + \frac{2e\alpha}{\hbar} \tag{B.3}$$

Any measurable quantity needs to be gauge invariant, hence one can only measure changes in the phase, not the absolute phase itself. This means that though, well defined and coherent, the phase of a superconductor can be chosen arbitrarily from a degenerate manifold of possibilities of ground states. This is very similar to the spontaneous symmetry breaking in the Landau phase transition picture (see Appendix C). Hence it is common to say that superconductors break the gauge symmetry. However, as we shall see in the next section, the physical state of superconductor also involves electromagnetic field, and once the complete picture is considered, it turns out that all possible phases are re-

[1] Note that this will not be the case with the mean-field Hamiltonian (1.15), because there the order parameter is already introduced and symmetry is lowered.

ally just gauge equivalent ways to describe the same physical ground state of superconductor $\Delta = \Delta_0 e^{i\phi}, \mathbf{E} = 0, \mathbf{B} = 0$ and at no point, gauge symmetry is actually *broken*. Also, at least in lattice gauge theories, famous Elitzur's theorem prohibits local gauge symmetry breaking[110].

To see this, consider the ground state of superconductor $\Delta = \Delta_0 e^{i\phi}, \mathbf{E} = 0, \mathbf{B} = 0$. Electromagnetic fields $\mathbf{E} = 0, \mathbf{B} = 0$ when the field-strength tensor $F_{\mu\nu} = 0$ (see (A.13)). Hence, from (A.12), $F_{\mu\nu}$ can be represented as what is known as a *pure gauge* i.e. $F_{\mu\nu} = \partial_\mu \beta$, where β is a scalar. Hence the ground state of superconductor is

$$\Delta = \Delta_0 e^{i\phi}, \quad A_\mu = \partial_\mu \beta \tag{B.4}$$

Now, if we perform gauge transformation, $A_\mu \mapsto A_\mu + \alpha$ and $\phi \mapsto \phi + \frac{2e\alpha}{\hbar}$, we get

$$\Delta = \Delta_0 e^{i\left(\phi + \frac{2e\alpha}{\hbar}\right)}, \quad A_\mu = \partial_\mu(\beta + \alpha) \tag{B.5}$$

Here, the phase of the superconductor is changed, and since α is arbitrary it might give the impression that we have a degenerate manifold of ground states to choose from and picking one phase *breaks* this gauge symmetry. However, two states related by gauge transformations are the *same physical state with merely different descriptions.* Hence there is only one physical state with $|\Delta| = \Delta_0, \mathbf{E} = 0, \mathbf{B} = 0$ and the different phases are gauge equivalent ways of describing this state. The gauge invariance of the Hamiltonian and gauge covariance of the ground state superconductor, has important consequences which we discuss in the next section.

B.1 Electrodynamics of Superconductors from Gauge Symmetry: An Effective Field Theory Picture

In effective field theories for phase transition, an analysis pioneered by Ginzburg and Landau, rather than solving the microscopic Hamiltonian which might be complicated, we construct a free energy $\mathcal{F}$ with an order parameter (see Appendix C) which respects all the symmetries of the problem. Then this free energy $\mathcal{F}$ can be minimized variationally to calculate the quantities associated with the phase transition [111]. As we saw in the previous section, the Hamiltonian of superconductivity is gauge invariant and the superconducting ground state is gauge covariant. These two critical properties can explain the fundamental electrodynamics of a superconductor using an effective mean-field.

First we generalize the order parameter to a time dependent one as $\Delta(\mathbf{r}, t)$. The free energy will also need an electromagnetic field. In the most general case, the free energy $\mathcal{F}$ can depend on the order parameter, its conjugate, the electrodynamic field, their derivatives as $\mathcal{F}\left[\Delta, \Delta^*, \partial_\mu\Delta, \partial_\mu\Delta^*, A_\mu, \partial_\mu A_\nu\right]$. However, the gauge invariance severely restricts the form of $\mathcal{F}$. Due to the gauge covariance $\Delta \mapsto e^{-i\frac{2e\alpha}{\hbar}}\Delta$ of the order parameter Δ, the corresponding gauge invariant quantity that can be constructed is simply the magnitude $\Delta^*\Delta$. We also need to create a gauge covariant version of the derivative D_μ as the simple derivative ∂_μ under gauge transformation transforms as

$$\partial_\mu\Delta \mapsto \partial_\mu\left(e^{i\frac{2e\alpha}{\hbar}}\Delta\right) = e^{i\frac{2e\alpha}{\hbar}}\left(\partial_\mu + i\frac{2e}{\hbar}\partial_\mu\alpha\right)\Delta \tag{B.6}$$

which is clearly not gauge covariant. Hence to construct gauge invariant terms

in $\mathcal{F}$, we introduce gauge covariant derivative

$$D_\mu \equiv \partial_\mu - i\frac{2e}{\hbar}A_\mu \tag{B.7}$$

It can be checked that this is now gauge covariant as under gauge transformation

$$\begin{aligned} D_\mu\Delta = \left(\partial_\mu - i\frac{2e}{\hbar}A_\mu\right)\Delta \mapsto \left(\partial_\mu - i\frac{2e}{\hbar}(A_\mu + \partial_\mu\alpha)\right)(e^{i\frac{2e\alpha}{\hbar}}\Delta) = e^{i\frac{2e\alpha}{\hbar}}\left(\partial_\mu + i\frac{2e}{\hbar}\partial_\mu\alpha - i\frac{2e}{\hbar}(A_\mu + \partial_\mu\alpha)\right) \\ \implies D_\mu\Delta \mapsto e^{i\frac{2e\alpha}{\hbar}}D_\mu\Delta \end{aligned} \tag{B.8}$$

Hence the gauge invariant term from this gauge covariant Derivative will be simply $(D_\mu\Delta)^* D^\mu\Delta$. However, there can be less restriction if we take into account some properties of the mean field. Let us have a closer look at $\partial_\mu\Delta$, where we separate magnitude and phase explicitly as $\Delta = |\Delta|e^{i\phi}$

$$\partial_\mu\Delta = \partial_\mu\left(|\Delta|e^{i\phi}\right) = \left(\partial_\mu\phi + \frac{\partial_\mu|\Delta|}{|\Delta|}\right)\Delta \tag{B.9}$$

From our discussions of the mean field theory (section 1.1.3), we have seen that the order parameter $|\Delta|$ has a finite value in the superconducting state and fluctuations around this mean value is ignored, hence for low energy physics, it can be safely assumed that $\partial_\mu|\Delta| \ll |\Delta|$ and the second term can be ignored and we get $\partial_\mu\Delta \approx \partial_\mu\phi\Delta$. We also recall that, the phase transforms under gauge transformation as $\phi \mapsto \phi + \frac{2e\alpha}{\hbar}$ (Appendix B). The gauge transformation of an electromagnetic field is (Appendix A) $A_\mu \mapsto A_\mu - \partial_\mu\alpha$. With these observations, we can construct a gauge-invariant derivative as:

$$D_\mu\Delta = i\left(\partial_\mu - \frac{2eA_\mu}{\hbar}\right)\Delta \tag{B.10}$$

It can be checked that with Gauge transformation, this derivative stays invariant as

$$D_\mu\Delta = i\left(\partial_\mu\phi - \frac{2eA_\mu}{\hbar}\right)\Delta \mapsto i\left(\partial_\mu(\phi + 2e\alpha/\hbar) - \frac{2e(A_\mu + \partial_\mu\alpha)}{\hbar}\right)\Delta = i(\partial_\mu\phi - 2eA_\mu)\Delta = D_\mu\Delta \tag{B.11}$$

In fact, no other gauge-invariant combinations of the fields can be formed and the gauge-invariant free energy should have the dependence $\mathcal{F}\left[|\Delta|, \partial_\mu\phi - 2eA_\mu/\hbar\right]$.

Finally the free energy $\mathcal{F}$ needs to be minimized using a variational method. By assumption, this will occur at a non-zero value of order parameter $|\Delta|$. Also for a stable minimum, the term $\partial_\mu\phi - 2eA_\mu/\hbar$ should appear as a quadratic dependence near the minimum.

$$\mathcal{F} \sim K\left(\partial_\mu\phi - \frac{2eA_\mu}{\hbar}\right)^2 \tag{B.12}$$

Then $\mathcal{F}$ is minimized at

$$\partial_\mu\phi = \frac{2eA_\mu}{\hbar} \tag{B.13}$$

The relation in (B.13) is derived purely on the basis of gauge invariance of the free energy and the gauge covariance of the superconducting state. We will next derive key properties of superconductors using only this relation.

B.1.1 Perfect Conductivity

The time component of the eq.(B.13) leads to

$$\partial_t \phi = 2e\varphi/\hbar \tag{B.14}$$

where ϕ is the phase of the superconducting order-parameter and φ is the electric potential. Hence for any time independent field configuration where superconducting phase ϕ is not changing in time and $\partial_t \phi = 0$, eq. (B.13) means

$$\varphi = 0 \tag{B.15}$$

Hence no voltage or potential difference can be developed in steady-state in a superconductor. Constant current $\mathbf{j}$ is also a steady-state and by this argument, must flow without developing a potential difference and $\mathbf{j} = \sigma \mathbf{V}$ then implies that the conductivity σ is infinite for zero voltage V, if a finite current $\mathbf{j}$ flows.

B.1.2 Flux Quantization

Let us consider a thick ring of a superconductor with a closed contour γ inside it of an area S. The magnetic flux Φ through this contour will be

$$\begin{aligned} \Phi &= \int_S \mathbf{B} \cdot d\mathbf{S} \\ &= \int_S (\nabla \times \mathbf{A}) \cdot d\mathbf{S} \end{aligned} \tag{B.16}$$

using Stoke's theorem, we can convert the integral on the surface S to the contour γ we get

$$\Phi = \oint_\gamma \mathbf{A} \cdot d\mathbf{r} \tag{B.17}$$

Since the contour γ is inside a superconducting ring, the spatial components of eq.(B.13) tell us

$$\nabla\phi = \frac{2e\mathbf{A}}{\hbar} \tag{B.18}$$

Then we get,

$$\begin{aligned}\Phi &= \frac{\hbar}{2e}\oint_{\gamma}\nabla\phi\cdot d\mathbf{r} \\ &= \frac{\hbar}{2e}\Delta\phi\end{aligned} \tag{B.19}$$

Now around a closed loop, the $\Delta\phi$, the change in the superconducting phase can only change by an integer multiple of 2π (since the phase of a superconductor is well defined, this is necessary for the ensuring single valuedness). Hence

$$\Phi = n\frac{h}{2e} \tag{B.20}$$

B.1.3 Meissner Effect

One easy way to see Meissner Effect is to look at the spatial components of eq. (B.13)

$$\nabla\phi = \frac{2e\mathbf{A}}{\hbar} \tag{B.21}$$

Since magnetic field is $\mathbf{B} = \nabla\times\mathbf{A}$, in ground state of superconductor, $\nabla\times\mathbf{A} = \nabla\times\nabla\phi = 0$, as curl of a gradient is always zero [108]. Hence magnetic field cannot exist inside a superconductor.

APPENDIX C

SPONTANEOUS SYMMETRY BREAKING AND PHASE TRANSITIONS

A symmetry of a system is a transformation under which the Hamiltonian describing the system remains unchanged. The symmetry can be *broken* by adding terms to the Hamiltonian which do not respect the symmetry (with the new term, the Hamiltonian is no longer invariant under transformation). The symmetry is said to be *spontaneously broken* when no additional term is added to the Hamiltonian, but the ground state can have a reduced symmetry as compared to the Hamiltonian i.e., there is a symmetry transformation under which Hamiltonian is invariant but the ground state is not. These deep ideas were developed by Landau to study phase transitions. In terms of phase transition, below the critical point where the phase transition occurs, the system can develop a non-zero expectation value for an operator of lower symmetry than Hamiltonian in a ground state than the ground state before transition where expectation value of the operator was zero. The expectation value of this operator is referred to as the order parameter Δ. The reason for the non-zero value of this expectation value is that the system is no longer ergodic. It picks a ground state among a possible set of degeneracies, however, the different possibilities are separated by an energy barrier after phase transition, hence it likes to stay in only one of them (the phase). If there were to be no barrier between these degeneracies, ergodicity would ensure that system goes in all of them and that will effectively average out the order parameter Δ to be zero. This is illustrated in a free energy diagram in Fig. C.1. Before the phase transition the ground state of the system (Free energy minimum) is at $\Delta = 0$ as shown in Fig. C.1. After phase transition induced changes in Free energy, the ground state of the system has a degeneracy at $\Delta = \Delta_0$ and $\Delta = -\Delta_0$ separated by an energy barrier. The system picks

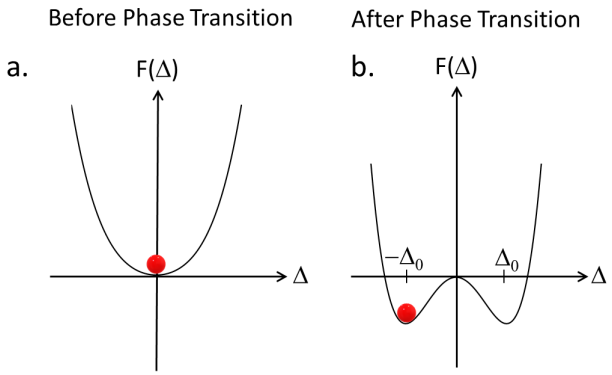

Figure C.1: Spontaneous symmetry breaking and phase transition. The system before the phase transition is in the ground state at a minimum in Free energy at order parameter $\Delta = 0$. After the phase transition, the free energy has changed and the ground state is degenerate at $\Delta = \pm\Delta_0$. System picks one and symmetry is said to be spontaneously broken.

one of them, and the phase-transition is said to have occurred. An example is a crystal which breaks translational symmetry of space by having atoms at lattice points separated in space or a Ferromagnet which breaks rotational symmetry by picking a direction in the space for the magnetization axis. It will cost energy to change one lattice to another degenerate one or one magnetization axis to another degenerate one. We reiterate here that in the case of superconductors, the gauge symmetry is not spontaneously broken.

APPENDIX D

ANDERSON-HIGGS MECHANISM: MEISSNER EFFECT AS PHOTONS ACQUIRING MASS

The discovery of Higgs boson was a major discovery in Physics which was announced in Summer 2012, the time I was learning the ropes in condensed matter physics and I was very fascinated by it. Soon afterward, this discovery was awarded the noble prize. However, the initial ideas were worked out by Anderson in the context of superconductivity [112]. Let us consider a Lorentz-invariant analog of superconductivity, the Abelian Higgs-model which is defined by a Lagrangian [113]:

$$\mathcal{L} = (D^{\mu}\Delta)^{*}(D_{\mu}\Delta) - \frac{1}{4}F_{\mu\nu}F^{\mu\nu} - V(|\Delta|) \tag{D.1}$$

It must be noted that this model does not actually describe a superconductor but is just a useful pedagogical tool to illustrate Anderson-Higgs mechanism. For an order-parameter $\Delta = |\Delta|e^{i\phi}$, the gauge covariant dervative can be defined as in eq.B.10 in section B.1$D_{\mu}\Delta = (\partial_{\mu}\phi - 2eA_{\mu}/\hbar)\Delta$. Like in Field-theory literature, let us use natural units: $\hbar = c = 1$. Using this, the Lagrangian (D.1)takes the form:

$$\mathcal{L} = |\Delta|^2(\partial_{\mu}\phi - 2eA_{\mu})^2 - \frac{1}{4}F_{\mu\nu}F^{\mu\nu} - V \tag{D.2}$$

We can define a new gauge invariant vector field

$$\tilde{A}_{\mu} \equiv A_{\mu} - \frac{1}{2e}\partial_{\mu}\phi \tag{D.3}$$

It can be checked that $\tilde{A}_{\mu}$ is guage invariant since under a gauge transformation,

$$\tilde{A}_{\mu} \mapsto A_{\mu} + \partial_{\mu}\alpha - \frac{1}{2}\partial_{\mu}(\phi + 2e\alpha) = A_{\mu} - \frac{1}{2e}\partial_{\mu}\phi = \tilde{A}_{\mu} \tag{D.4}$$

The field strength tensor in A.12 stays invariant under this transformation. With this new gauge field, the Lagrangian becomes:

$$\mathcal{L} = (2e)^2|\Delta|^2\tilde{A}_\mu\tilde{A}^\mu - \frac{1}{4}F_{\mu\nu}F^{\mu\nu} - V \tag{D.5}$$

Now, in Field-theory terms, the term quadratic in $\tilde{A}_\mu$ means that this electromagnetic vector field, (whose quantum is a photon.) has a mass of $m^2 = 2e^2|\Delta|^2$! This can be seen more explicitly if we use this Lagrangian to write the Euler-Lagrange equations of motions [114] of the system:

$$\begin{aligned}
\frac{\partial\mathcal{L}}{\partial\tilde{A}^\nu} - \partial_\mu\frac{\partial\mathcal{L}}{\partial(\partial_\mu\tilde{A}^\nu)} &= 0 \\
m^2\tilde{A}_\nu + \partial^\mu F_{\mu\nu} &= 0 \\
m^2\tilde{A}_\nu + \partial^\mu(\partial_\mu\tilde{A}_\nu - \partial_\nu\tilde{A}_\mu) &= 0 \\
m^2\tilde{A}_\nu + \partial^\mu\partial_\mu\tilde{A}_\nu - \partial_\nu\partial^\mu\tilde{A}_\mu &= 0
\end{aligned} \tag{D.6}$$

The current is given by[115]

$$j_\mu = -\frac{\partial\mathcal{L}}{\partial\tilde{A}^\mu} = -m^2\tilde{A}_\mu \tag{D.7}$$

For this current to be conserved, we must have $\partial^\mu j_\mu = 0$ implying $\partial^\mu\tilde{A}_\mu = 0$. This sets the last term in Euler-Lagrange equation of motion in eq. (D.6) to 0, leaving us with simply

$$(\partial_\mu\partial^\mu + m^2)\tilde{A}_\mu = 0 \tag{D.8}$$

This is Klein-Gordon equation [115] of a classical field of mass m. This can be made more visible if we decompose the electromagnetic field in its Fourier components as

$$\tilde{A}_\mu = \int d^4x e^{ip_\mu p^\mu}\tilde{A}_\mu(p) \tag{D.9}$$

where 4-momentum $p^\mu = (E, \mathbf{p})$. Then the Klein-Gordon equation becomes

$$\begin{aligned}(-p_\mu p^\mu + m^2)\tilde{A}_\mu(p) &= 0 \\ -p_\mu p^\mu + m^2 &= 0 \\ E &= p^2 + m^2\end{aligned} \tag{D.10}$$

Which is readily identified as the relativistic dispersion of a particle with mass m. *Thus, the photons (vector field $\tilde{A}_\mu$) in a superconductor, due to the interplay of gauge covariance and gauge invariance, acquire a mass!* This mechanism was first proposed by Anderson [112] in the context of Superconductors. The same mechanism generates masses of W and Z bosons[1]. However it must be noted that, the "broken" gauge group in electroweak theory is Non-Abelian, hence the details of dynamics of course differs from the description here. There have been experimental observations of Higgs modes in superconductors summarized in Ref.[116].

To see the Meissner effect resulting from this acquisition of mass by photons, we can restrict to spacelike components of the Klein-Gordon equation (D.8) and further restrict to time-independent scenarios (for static magnetic field). Then Klein-Gordon equation (D.8) becomes

$$(-\nabla^2 + m^2)\tilde{\mathbf{A}} = 0 \tag{D.11}$$

Taking curl of this equation, and from relation $\nabla \times \tilde{\mathbf{A}} = \mathbf{B}$, we get

$$(-\nabla^2 + m^2)\mathbf{B} = 0 \tag{D.12}$$

This admits a solution that decays inside the superconductor exponentially $\sim e^{-mr}$, which is basically the Meissner effect.

[1] Anderson-Higgs mechanism also generates the mass of quarks and leptons but with a Yukawa coupling which is not analogous Superconductors.

For a more physical result, let us use the Ginzburg-Landau free energy for superconductors (For details of Ginzburg-Landau theory please see Tinkham**??**)

$$\mathcal{F} = \int d^3x \frac{|\Delta|^2}{2m^*}(\nabla\phi - 2e\mathbf{A})^2 + \frac{1}{2}\mathbf{B}^2 + V(|\Delta|) \tag{D.13}$$

In terms of the vector field $\tilde{\mathbf{A}}$,

$$\mathcal{F} = \int d^3x \frac{(2e)^2|\Delta|^2}{2m^*}\tilde{\mathbf{A}}^2 + \frac{1}{2}\mathbf{B}^2 + V(|\Delta|) \tag{D.14}$$

Analogous to the relativistic case, the current is given by [7]

$$\mathbf{j} = -\frac{\delta F}{\delta \tilde{\mathbf{A}}} = -\frac{(2e)^2|\Delta|^2}{m^*}\tilde{\mathbf{A}} \tag{D.15}$$

We know from Maxwell's equation (A.4) that in static field configurations, $\nabla \times \mathbf{B} = \mathbf{j}$, this gives us

$$\nabla \times \mathbf{B} = -\frac{(2e)^2|\Delta|^2}{m^*}\tilde{\mathbf{A}} \tag{D.16}$$

Taking curl of both sides

$$\nabla \times \nabla \times \mathbf{B} = \nabla(\nabla \cdot \mathbf{B}) - \nabla^2\mathbf{B} = -\frac{(2e)^2|\Delta|^2}{m^*}\nabla \times \tilde{\mathbf{A}} \tag{D.17}$$

Maxwell's equation (A.2) tells us that $\nabla \cdot \mathbf{B} = 0$ and we also have $\nabla \times \tilde{\mathbf{A}} = \mathbf{B}$. This gives us

$$-\nabla^2\mathbf{B} = -\frac{(2e)^2|\Delta|^2}{m^*}\mathbf{B} \tag{D.18}$$

Hence, the magnetic field inside a superconductor decays as

$$\mathbf{B} = \mathbf{B}_0 e^{-r/\lambda} \quad \lambda^{-2} = \frac{(2e)^2|\Delta|^2}{m^*} \tag{D.19}$$

where λ is the penetration depth, which in SI units is given as [4]

$$\lambda = \sqrt{\frac{m_e}{2\mu_0 e^2|\Delta|^2}} \tag{D.20}$$

Hence, due to the Anderson-Higgs mechanism arising from interplay of gauge covariance and gauge invariance, the photons acquire a mass in superconductors, which leads to the exponential decay of magnetic field inside a superconductor leading to the characteristic Meissner effect given by eq. (D.19).

APPENDIX E

TOPOLOGICAL SUPERCONDUCTIVITY

In mathematics, topology refers to study of spaces which can be transformed into one another by stretching, bending, crumpling, but not by cutting or gluing. Hence the properties of such spaces are based on a global nature in a certain sense which will be clear as we look at some examples later. This means that these properties are robust against small distortions of spaces.

Similarly in physics, there are properties which are robust to small changes in Hamiltonians, unless one opens or closes a gap. The extremely robust quantization in Integer Quantum Hall Effect (IQHE) is a result of Hall conductivity being a topological quantity. Kosterlitz, Thouless and Haldane won Nobel prize in 2016 for the theoretical development of topological ideas in Physics. Many other scientists have contributed to this endeavor greatly through the decades. Superconductor, being a gapped Hamiltonian, can also have topological classifications and interesting related properties. Since Sr_2RuO_4, a subject of the thesis has been touted as a topological superconductor for a long time, I provide an extremely brief overview here so that we can later put our experimental results in context. The discussion here is limited only to the very basic definitions and toy models. Interested readers may refer for more details to the references mentioned at relevant locations in the following.

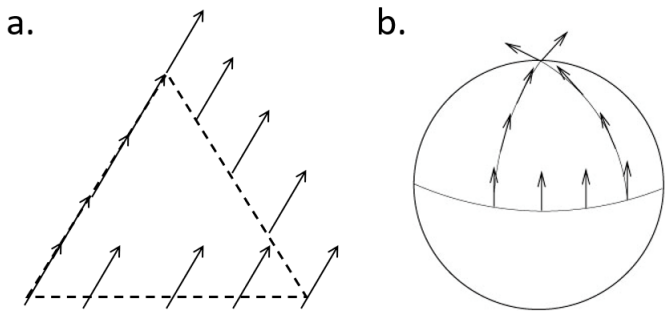

Figure E.1: Geometric phase and curvature. a) The oriented vector after moving along the closed path on a flat (zero curvature surface) returns to the same orientation as beginning. b) The oriented vector after moving along the closed path on a non-flat (nonzero curvature surface) does not return to the same orientation as beginning.

E.1 Motivation from Mathematics: Geometric Phase, Curvature and Topology

We start with mathematics, where the original ideas come from. Consider transporting an oriented object like a vector across a closed path as shown in Fig. E.1. This exercise is usually called parallel transport.

In Fig. E.1a, on a closed path, it can be seen that the the parallel transport of a vector finishes with the same orientation it started from. While in Fig. E.1b, it can be seen that the parallel transport of the vector changes the orientation after traveling along a closed path. This difference in the orientation of vector on traveling a closed path on a manifold is defined as *geometric phase*. As can be seen, it is zero for a flat surface and non-zero for a surface with finite curvature. This is basically a demonstration of the deep relationship between curvature and geometric phase.

A nice demonstration of topological property is offered by the Gauss-Bonnet

Figure E.2: Topological equivalence of a coffee mug and a donut.

Theorem, which relates the number of holes (called genus g) in an object to the curvature κ integrated over the whole manifold.

$$\frac{1}{2\pi}\int_M \kappa dA = 2(1-g) \tag{E.1}$$

This is striking because the integrand on the left-hand side, curvature κ of a manifold is a local quantity which can be changed by stretching, bending and crumpling the manifold but as long as these deformations do not poke a new hole, the theorem states that the value of integration over a closed manifold will just be a simple constant related to the number of holes g. This means that if we integrate the curvature in any of the stages of deformation of a mug to a donut as shown in Fig. E.2, the result will always be zero (corresponding to $g = 1$).

All the objects in Fig. E.2, including the mug and the donut, belong to the same topological class of $g = 1$. A sphere for example, having no holes will be a different topological class of $g = 0$ and by Gauss-Bonnet theorem (E.1), the integration of curvature of any surface with zero holes, will give the same result 2. An example of different topological classes are shown in Fig. E.3, where each row is in the same topological class.

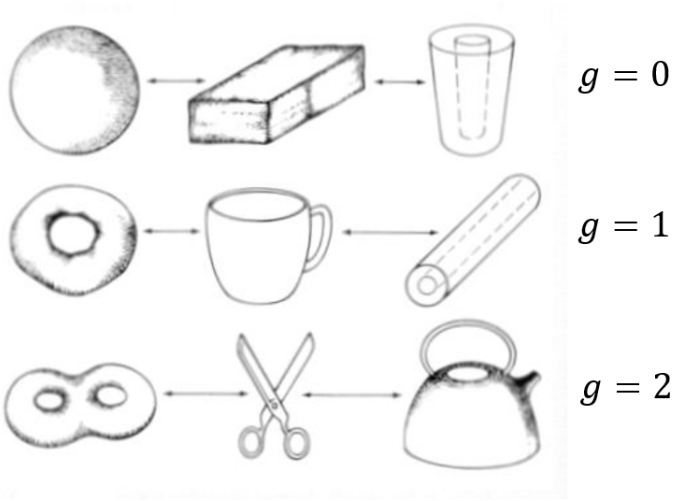

Figure E.3: Different topological classes

E.2 Condensed Matter Physics: Berry Phase, Berry Curvature and Topology

When we talk of topology in condensed matter physics, we are talking about the spaces of Hamiltonians. Gapped Hamiltonians which can be transformed into one another without closing the gap or opening a new one, are said to be in the same topological class.

The concept of parallel transport, as described in previous section, also exists for condensed matter physics thanks to quantum adiabatic theorem [35] which states that n^{th} eigenstate of a Hamiltonian H_1 is carried over to n^{th} eigenstate of a Hamiltonian H_2, if H_2 is obtained by slowly varying the parameters of H_1. Similar to the idea of geometric phase accumulated over a closed loop, the phase acquired when a Hamiltonian is parallel transported across a closed loop by adiabatic variation of its parameters, is called Berry Phase.[1] Also analogous

[1]The choice of phase in quantum mechanics is usually considered to be trivial, but Michael V. Berry [117] in 1986 showed that the phase accumulated around a loop is non-trivial and can

to the previous section, the Berry phase is non-trivial for non-trivial curvature, which is known as Berry curvature [119].

Similar to the discussion of Gauss-Bonnet theorem in the previous section, Berry curvature integrated over a closed manifold of Brillouin zone (BZ) leads to a topological invariant known as Chern number or TKNN invariant (named after the theorists Thouless, Kohmoto, den Nijs and Nightingale who developed topological ideas to explain integer quantum hall effect (IQHE) and found that hall conductivity is actually a Chern number [120].)

$$C_{\text{TKNN}} = \frac{1}{2\pi} \int_{\text{BZ}} d\mathbf{k}\Omega(\mathbf{k}) \tag{E.2}$$

Analogous to the Gauss-Bonnet theorem creating classes of manifolds, this integer can divide Hamiltonians into different topological classes as shown in figure E.4. A simple gapped Hamiltonian of an insulator is in class $C = 0$ and IQHE with insulating bulk and conducting edge states [121] is in class $C = 1$

Before we move onto the definition of topological superconductors, I just want to mention that lately a lot of research is driven into the field of topological materials [122, 123] because necessity of having the magnetic field to have a topologically non-trivial material was removed by the idea of time-reversal symmetry preserving topological insulators [124]. For this class of materials, Chern number is zero, but there is another $\mathbb{Z}_2$ invariant $\nu_{\mathbb{Z}_2}$ which characterizes this class of bulk insulators having conducting counter-propagating spin-polarized, edge states; and distinguishes it from a trivial bulk insulator as shown in Fig. E.5.

have physical consequences like Aharonov-Bohm effect [118]

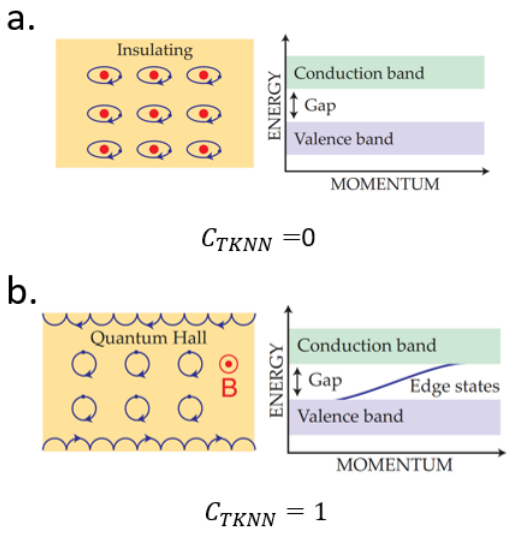

Figure E.4: Different topological classes based on TKNN invariant. a) A simple atomic insulator with a gap between conduction and valence band. b) Integer quantum Hall effect with insulating bulk. Conducting edge states connecting valence and conduction band and lead to integer quantized Hall conductance.

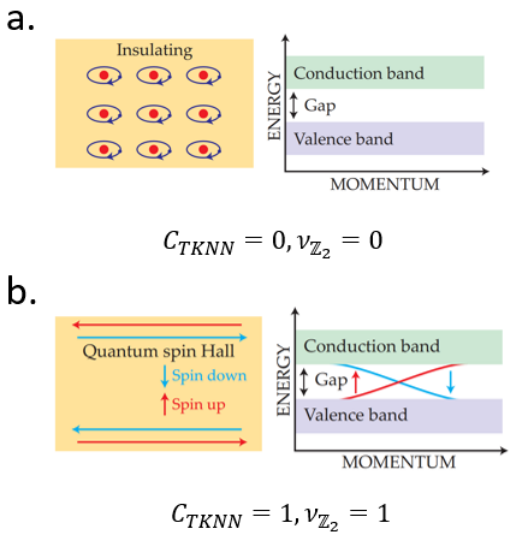

Figure E.5: Time reversal symmetric topological insulator. a) Trivial insulator. b) Topological insulator, a topologically non-trivial class realized without external magnetic field with conducting, counter propagating, spin polarized edge states [124]

E.3 Topological Superconductors

We have seen that the superconductors also have a gap for quasiparticle excitations in section 1.1.3. Hence these topological classifications can also be applied to superconductors. I only mention key definitions here for a simple toy-model and direct the interested readers for more details to excellent reviews on this subject [125, 126]. A complete classification of topological superconductors based on symmetries present in a system can be found in [127].

The Bogoliubov de Gennes Hamiltonian is represented in the form of a 2×2 matrix (1.20) which we reproduce here

$$H_{\mathrm{BdG}} = \begin{pmatrix} \xi_{\mathbf{k}} & \Delta_{\mathbf{k}} \\ \Delta_{\mathbf{k}}^{*} & -\xi_{\mathbf{k}} \end{pmatrix} \tag{E.3}$$

The Bogoliubov Hamiltonian H_{BdG} can be expressed in the basis of 2×2 Pauli matrices $\boldsymbol{\sigma} = (\sigma_x, \sigma_y, \sigma_z)$ as

$$H_{\mathrm{BdG}} = \mathbf{h} \cdot \boldsymbol{\sigma} \tag{E.4}$$

Now this vector $\mathbf{h}$ can be used to define a Chern number [125] (we only look at the 2D case, relevant for claims made on Sr_2RuO_4 which is being studied here) as

$$C = \frac{1}{4\pi} \int d\mathbf{k} \left[\hat{\mathbf{h}} \cdot \left(\partial_{k_x} \hat{\mathbf{h}} \times \partial_{k_x} \hat{\mathbf{h}} \right) \right] \tag{E.5}$$

where $\hat{\mathbf{h}}$ is the unit vector from $\mathbf{h}$, which encodes the superconducting Hamiltonian H_{BdG}. If this Chern number is non-zero, then the superconductor is time reversal symmetry breaking, $p + ip$ spinless superconductor [125]. For a intuitive picture [125], one can imagine the unit vector $\hat{\mathbf{h}}$ moving on a unit sphere as k-values are scanned across the Brillouin zone as shown in Fig. E.6. If the this unit vector does not wind around the sphere completely, it is topologically

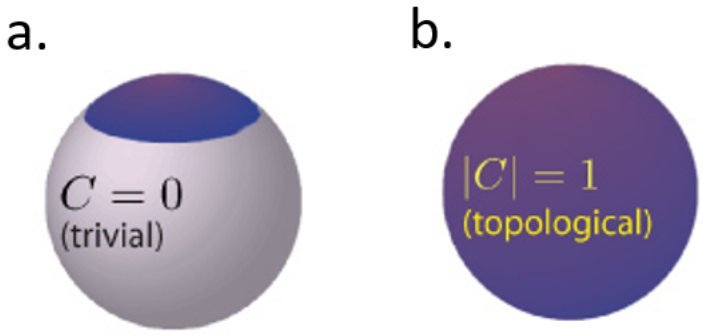

Figure E.6: Intuitive picture for Chern number of Topological superconductors. a) The vector $\hat{\mathbf{h}}$ does not wind around the whole sphere, hence this is a topologically trivial superconductor with $C = 0$. b) The vector $\hat{\mathbf{h}}$ does not wind around the whole sphere once, hence $C = 1$ and this is a spinless $p + ip$ topological superconductor.

equivalent to a sphere where there is no winding, hence topologically trivial. On the other hand, if the unit vector winds around the sphere completely once, then it is topologically non-trivial as this winding cannot be undone without poking a hole in the map.

A quick note about material systems, from my perspective. In the H_{BdG} there are two parameters to be played with: the normal dispersion $\xi_{\mathbf{k}}$ and the superconducting gap $\Delta_{\mathbf{k}}$. For obtaining a non-trivial topological invariant, one can look for systems in mother Nature which have a non-trivial $\Delta_{\mathbf{k}}$ because of exotic pairing interactions. For example, an Odd parity $\Delta_{\mathbf{k}}$ will be a topological superconductor [125, 126]. The other way is to engineer a system with an intrinsically trivial superconductor with a constant s-wave gap Δ but with materials with normal state dispersion $\epsilon_{\mathbf{k}}$ is non-trivial. Hence there is a huge effort to engineer a topological superconductor by interfacing topological insulators with s-wave superconductors via doping or heterostructures [125, 126].

E.4 Majorana Zero Modes in Topological Superconductors

A Majorana fermion is a fermion (i.e. a half-integer spin particle) that is its own antiparticle, as hypothesized by Ettore Majorana in 1937[2]. It differs from Dirac fermions in the sense that the creation and annihilation operators are distinct for a Dirac fermion but the same for a Majorana fermion i.e. $\gamma_i^\dagger = \gamma_i$, where $\gamma_i^\dagger$ creates a Majorana fermion in the state i. Because particles and antiparticles have opposite conserved charges, a Majorana fermion has to be neutral. In the standard model, all the fundamental half-integer particles have gauge charges so they are Dirac fermions with the exception of neutrino, whose nature is not settled and it may be a Majorana fermion. In condensed matter systems, this property of $\gamma^\dagger = \gamma$ may be realized for quasiparticles as we discuss in this section. Hence Majorana has made a return in condensed matter physics [128]. In this section, we provide a very brief glimpse at Majorana zero modes in topological superconductors. For more details on Majorana physics, please refer to the reviews in [125, 129].

Let us consider solution of Dirac equation, which describes spin-1/2 Fermions. Dirac equation is complex and hence the solutions, the Dirac fermions are described by complex operators. This is natural because the complex conjugate of a complex Dirac fermions is the antiparticle, the first such discovery being the positron (antiparticle of electron). However, Before Dirac, Ising realized that complex fermion operators $c^\dagger$ and c can be decomposed using

[2]Majorana disappeared under unknown circumstances after buying a boat trip a ticket from Palermo to Naples in 1938. The yet to be discovered elusive Majorana states go hand in hand with the story of his mysterious disappearance.

real operators γ_1 and γ_2 as:

$$\begin{aligned} c^\dagger &= \frac{1}{2}(\gamma_1 + i\gamma_2) \\ c &= \frac{1}{2}(\gamma_1 - i\gamma_2) \end{aligned} \tag{E.6}$$

The real operators γ_i are in a sense *half a fermion*. The Ising fermion decompositon in eq. E.6 can be inverted to get:

$$\begin{aligned} \gamma_1 &= \frac{1}{2}(c + c^\dagger) \\ \gamma_2 &= \frac{i}{2}(c - c^\dagger) \end{aligned} \tag{E.7}$$

It can be seen easily that $\gamma_i^\dagger = \gamma_i$. These operators, with the normalization such that $\gamma_i^2 = I$, I being the identity, follow the anti-commutation relations:

$$\{\gamma_i, \gamma_j\} = 2\delta_{ij} \tag{E.8}$$

The same algebra as outlined in eq.(E.8) describes the Majorana fermions in the real solution to the Dirac equation Majorana proposed and these operators came to be known as the Majorana operators.

The defining condition for Majorana fermions $\gamma_i^\dagger = \gamma$ prevents any charged particles from being a Majorana fermion. Here, the superconductors come to our rescue as the quasiparticles in a superconductor, the Bogoliubons are a mix of electrons and holes! We recall from the section 1.1.3 that the mean-field BCS Hamiltonian is diagonalized by the Bogoliubov-Valatin transformation as given in eq. (1.21), which defined new quasiparticles γ as.

$$\begin{aligned} \gamma_{\mathbf{k}\uparrow} &= u_{\mathbf{k}}^* c_{\mathbf{k}\uparrow} + v_{\mathbf{k}} c_{-\mathbf{k}\downarrow}^\dagger \\ \gamma_{-\mathbf{k}\uparrow}^\dagger &= -v_{\mathbf{k}}^* c_{\mathbf{k}\uparrow} + u_{\mathbf{k}} c_{-\mathbf{k}\downarrow}^\dagger \end{aligned} \tag{E.9}$$

Where the coherence factors $u_{\mathbf{k}}$ and $v_{\mathbf{k}}$ are given as in eq. (E.10)

$$\begin{aligned} |u_{\mathbf{k}}|^2 &= \frac{1}{2}\left(1 + \frac{\xi_{\mathbf{k}}}{E_{\mathbf{k}}}\right) \\ |v_{\mathbf{k}}|^2 &= \frac{1}{2}\left(1 - \frac{\xi_{\mathbf{k}}}{E_{\mathbf{k}}}\right) \end{aligned} \tag{E.10}$$

where

$$E_{\mathbf{k}} = \sqrt{\xi_{\mathbf{k}}^2 + |\Delta_{\mathbf{k}}|^2} \tag{E.11}$$

If we measure energies from the Fermi-level, then normal state dispersion $\xi_{\mathbf{k}} = 0$ at Fermi level. Hence at Fermi level we get $|u_{\mathbf{k}}| = |v_{\mathbf{k}}| = 1/\sqrt{2}$. If we have a bound state at the Fermi level made from Bogoliubons, the Bogoliubons will be given from eq.(E.9) as

$$\gamma_{\mathbf{k}\uparrow}(E = 0) = \frac{1}{\sqrt{2}}(c^{\dagger}_{-\mathbf{k}\downarrow} + c_{\mathbf{k}\uparrow}) \tag{E.12}$$

$$\gamma^{\dagger}_{-\mathbf{k}\uparrow}(E = 0) = \frac{1}{\sqrt{2}}(c^{\dagger}_{-\mathbf{k}\downarrow} - c_{\mathbf{k}\uparrow}) \tag{E.13}$$

Where we have assumed real $u_{\mathbf{k}}$ and $v_{\mathbf{k}}$. It can be seen that if the spin and momenta indices can be suppressed, then the Bogoliubons in eq. (E.12) at zero energy evidently satisfy $\gamma^{\dagger}(E = 0) = \gamma(E = 0)$, the Majorana condition! These states are called Majorana zero modes, which is a more accurate way to refer to them rather than calling them Majorana fermions (the distinctions is not always maintained in literature) as they no longer follow the fermion statistics. For a simple two body state, the Fermion statistics implies $\psi(\mathbf{r}_1, \mathbf{r}_2) = -\psi(\mathbf{r}_2, \mathbf{r}_1)$. Instead, Majorana fermions follow the non-abelian anyon statistics. The anyon statistics for a simple two body state implies $\psi(\mathbf{r}_1, \mathbf{r}_2) = e^{i\phi}\psi(\mathbf{r}_2, \mathbf{r}_1)$. The non-abelian anyon statistics means that the state resulting from a clockwise-exchange of the two particles will be different from the state resulting from an anti-clockwise exchange of the two particles. In the next section, we will see how we can achieve

the Majorana zero modes with vortices in a chiral odd-parity superconductor.

E.5 Majorana Zero Modes in Half Quantum Vortices in Chiral Odd-Parity Superconductors

From the discussion in the previous section, we see that to realize Majorana condition, we will need a Bogoliubon state at zero energy, within the superconducting gap. One way to get the states in the superconducting gap is to apply a magnetic field to a superconductor. As been shown in appendix D in eq. (D.19), the magnetic field exponentially decays within a Superconductor. However, for certain superconductors, up to a certain critical magnetic field, the magnetic field can penetrate the superconductor as tubes known as vortices [4]. The superconducting gap goes to zero at the core of such vortices as the magnetic field cannot survive in a superconductor(eq. (D.19)). The Hamiltonian describing a vortex in a superconducting plane can be written as [130]:

$$H = \int d^2\mathbf{r}\left[\psi^\dagger\left(-\frac{-\nabla^2}{2m} - E_F\right) + \psi^\dagger[e^{i\theta}\Delta(r)\psi^\dagger] + \text{H.c.}\right] \tag{E.14}$$

where (r, θ) represent the 2D coordinates. Caroli, de Gennes and Matricon solved the equation (E.14) using the Bogoliubov-Valatin transformation (see section 1.1.3 and eq. (1.21)) $\gamma^\dagger = u\psi^\dagger + v\psi$ and showed that there are bound states at the vortex [130]. These bound states are known as Caroli-de Gennes-Matricon (CdGM) states and for an even-parity superconductor studied, the CdGM states are located at energies $E = (n + 1/2)\hbar\omega_0$, where n is an integer and $\hbar\omega_0 \sim \Delta^2/E_F$. Hence there are no states at 0 energy for even parity superconductor.

Let us look at the Hamiltonian for a vortex in a chiral p-wave superconduc-

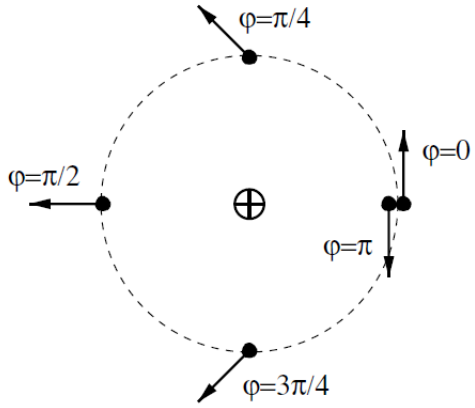

Figure E.7: A half quantum vortex. The arrows denote the d-vector. Figure reproduced from [131].

tor:

$$H = \int d^2\mathbf{r}\left[\psi^\dagger\left(-\frac{-\nabla^2}{2m} - E_F\right) + \psi^\dagger[e^{i\theta}\Delta(r) * (\nabla_x + i\nabla_y)\psi^\dagger] + \text{H.c.}\right] \tag{E.15}$$

where $*$ is the symmetrized product given as $A * B = (AB + BA)/2$. The wavefunction ψ for the condensate in the vortex can be given as [131]:

$$\psi(r,\theta) = \Delta(r)[e^{i\theta}|\uparrow\uparrow\rangle + |\downarrow\downarrow\rangle](k_x + ik_y) \tag{E.16}$$

The condensate in the vortex of an odd-parity chiral superconductor is very different from the vortices in the even-parity chiral superconductor. We have seen in section 1.2.1 that the order parameter for odd-parity superconductors is a vector order parameter, the d-vector (eq.(1.29)). Since the phase of the superconductor is well defined, the overall wavefunction should change the phase by 2π when the loop occurs around a vortex. If the d-vector can be rotated, then the overall phase of the cooper pair can be changed by both rotating the d-vector, and rotating the phase of the orbital part of the wavefunction. Hence to achieve an overall phase change of 2π around a vortex core, we can rotate the spatial wavefunction φ by π and the d-vector by π as schematically shown in Fig. E.5.

Since the orbital part of wavefunction rotates only by half of the usual 2π, these vortices are called *half quantum vortices*. The spin-up and spin-down sections here decouple and the spin-down sector has no vortex and hence no bound states, while the spin-up sector is described by Hamiltonian in eq. (E.14). This makes the model effectively spinless. This cannot be achieved with an even-parity superconductor as the spins, in that case, have to be singlet. Hence the Bogoliubons to diagonalize Hamiltonian (E.14) ,

$$\gamma^\dagger = u\psi^\dagger + v\psi \tag{E.17}$$

$$\gamma = v^*\psi^\dagger + u^*\psi \tag{E.18}$$

can be spinless. This diagonalization has been performed [132] and the resulting bound state energies are given as $n\hbar\omega_0$, where n represents an integer. Hence now, there can be a bound state at zero energy! Since this model is effectively spinless, u and v represent the same spin (same fermion). Hence we get from eq. (E.12), the zero-energy bound state as:

$$\gamma^\dagger(E=0) = \frac{1}{\sqrt{2}}(\psi + \psi^\dagger) = \gamma(E=0) \tag{E.19}$$

Thus we have a Majorana Zero mode at the vortex core of a chiral-odd parity superconductor! Majorana zero mode is a better-suited term than Majorana fermions as these states follow non-abelian anyon statistics rather than fermion statistics. In the next section, we look at the statistics of these Majorana zero modes in Half quantum vortices of a chiral p-wave superconductors next.

E.6 Non Abelian Anyon Statistics of Majorana Zero Modes in A Chiral p-wave Superconductors

Quantum statistics, the existence of symmetry rules for what happens to many-body wavefunctions when two particles are interchanged, is important for the existence of the world as we know it. Pauli exclusion principle, metals, superconductors, bose-einstein condensate etc. are a manifestation of quantum statistics at play. In 3+1 dimensional world, the world lines of the particles cannot get tangled (all knots in 3D are trivial in 4D, as whenever one finds an intersection in 3D, one can move to 4th dimension and untangle it.) and all world lines are basically representations of permutation group S_N, the two irreducible representations in one dimension being fermions and bosons. Let us look at the simplest case of two particles. Let the particle exchange be denoted by μ

$$\text{one exchange: } \psi(\mathbf{r}_1, \mathbf{r}_2) \mapsto \mu\psi(\mathbf{r}_1, \mathbf{r}_2) = \psi(\mathbf{r}_2, \mathbf{r}_1) \tag{E.20}$$

$$\text{two exchanges: } \psi(\mathbf{r}_1, \mathbf{r}_2) \mapsto \mu^2\psi(\mathbf{r}_1, \mathbf{r}_2) = \mu\psi(\mathbf{r}_2, \mathbf{r}_1) = \psi(\mathbf{r}_1, \mathbf{r}_2) \tag{E.21}$$

Hence we have $\mu^2 = 1$ for two exchanges from eq. (E.20), because as discussed the state after two exchanges is trivially related to the initial state. This statistics leaves us with the two possibilities $\mu = +1$ for a boson and $\mu = -1$ for a fermion.

However in 2+1 dimensions, the world lines can most definitely get tangled [3]! Let us consider performing two interchanges, which bring a particle back to the initial positions. For 3+1 dimensional world lines, this is a topologically trivial operation because the winding of world lines can be undone (like knots in 3D can be undone in 4D). But if the particles are confined to 2+1 dimensions,

[3] This concept of non-trivial statistics in 2+1 D was realized first by Leinaas and Myrheim [133] and Wiczek [134] further contributed to it.

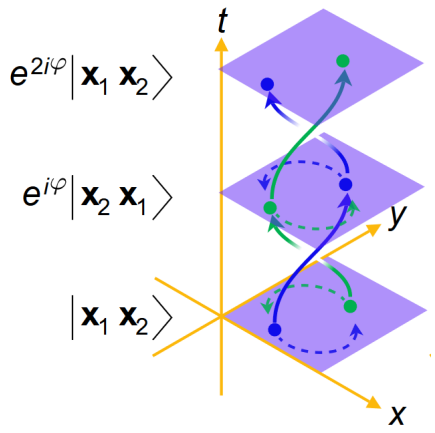

Figure E.8: Worldlines showing non-trivial topology of exchange of two anyons. It can be noticed that the worldlines cannot be untangled in 2+1 dimensions as shown and allow for anyon statistics. For 3+1 dimensions, such worldlines can be unentangled by moving into the 4th dimension whenever one encounters an intersection, hence this operation of two exchanges will be trivial in 3+1 dimensions which only allows boson and fermion statistics. Figure from Wikimedia Commons.

the world lines contain an imprint of these operations which cannot be undone and hence are topologically non-trivial as can be seen in Fig. E.8.

Since the two particle exchange is no longer trivial, if we let σ denote an exchange of two particles, since it is not going to ever return to the initial state, $\sigma^2 \neq 1$. This is the crucial distinction between anyon and fermion/boson statistics, which materializes in 2+1 D. For 2 anyons, σ is in fact given by the operator $\sigma = e^{i\phi}$. For N-such worldlines in 2+1 D, now the group becomes the braid group $\mathcal{B}_N$ as opposed to permutation group S_N for 3+1 D. Notice that the braid group has infinite number of elements even for two particles, while the number of elements for a permutation group is $|S_N| = N!$. The braid group $\mathcal{B}_N$ can be represented in terms of the exchange operators, which are called generators in group theory language. For arbitrarily ordered N anyons $1, 2, \ldots N$, let us denote the anti-clockwise (clockwise) exchange of ith and $i+1$th anyons by σ_i

(σ_i^{-1}). Then, the defining algebra for the braid group is given by [135]:

$$\sigma_i \sigma_j = \sigma_j \sigma_i \quad \text{for } |i-j| \geq 2, \tag{E.22}$$

$$\sigma_i \sigma_{i+1} \sigma_i = \sigma_{i+1} \sigma_i \sigma_{i+1} \quad \text{for } 1 \leq i \leq N-1 \tag{E.23}$$

Let us discuss the simplest member of the braid group, which is the set of 1D operations simply denoted as $\sigma = e^{im\phi}$, where m denotes the difference between the number of anti-clockwise exchanges and clockwise exchanges. The order of performing these operations will not matter and the statistics of a two anyon system is abelian. (the operator $e^{im\phi}$ commutes: $e^{im\phi}e^{in\phi} = e^{in\phi}e^{im\phi}$)

However, for higher dimensional representation of the braid group, the statistics may not be abelian. Consider a set of g degenerate states $\psi_1, \psi_2 \ldots \psi_g$ at n locations $R_1, R_2 \ldots R_n$. An element of braid group, is denoted now by a $g \times g$ unitary matrix $M(\sigma_i)$ acting on these states as (Einstein summation convention implying sum over repeated indices is used).

$$\psi_\alpha \mapsto [M(\sigma_i)]_{\alpha\beta}\psi_\beta \tag{E.24}$$

If matrices $M(\sigma_i)$ do not commute ($M(\sigma_i)M(\sigma_j) \neq M(\sigma_j)M(\sigma_i)$), then the statistics are non-abelian. A graphical representation of braid group statistics can be seen in Fig. E.6

Now, let us return to the system of Majorana Zero Modes in half quantum vortices in chiral p-wave superconductors as we discussed in the previous section E.5. Let us see how the $U(1)$ gauge transformation affects these states. If the overall phase of the superconductor changes by ϕ, the creation and annihilation operators (see eq. (E.16) and following discussion) in the vortex core change in phase by $\phi/2$ (Because the d-vector rotation by half, for the chiral p-wave superconductor causes the other half phase change). Thus $\psi_\alpha \mapsto e^{i\phi/2}\psi_\alpha$,

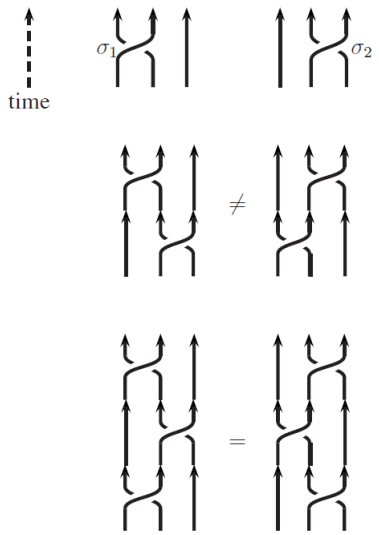

Figure E.9: A graphical representation of the braid group. Top: The elementary braid operations σ_1 and σ_2. Middle: Here it is shown that $\sigma_1\sigma_2 \neq \sigma_2\sigma_1$, hence the braid group in this representation is non-abelian. Bottom: Demonstration of one of the braid group defining relationship $\sigma_i\sigma_{i+1}\sigma_i = \sigma_{i+1}\sigma_i\sigma_{i+1}$ as outlined in eq. (E.23).Figure reproduced from [135].

$\psi_\alpha^\dagger \mapsto e^{-i\phi/2}\psi_\alpha^\dagger$ which means that the Bogoliubons, as given in eq. (E.17) will transform as $(u, v) \mapsto (ue^{-i\phi/2}, ve^{i\phi/2})$. Therefore, for exchange of half-quantum vortices then, where condensate makes one 2π phase winding around a vortex core, the Majorana zero mode as given in eq. (E.19) will transform as:

$$\begin{aligned} \gamma^\dagger &\mapsto \frac{1}{2}(\psi^\dagger e^{-i\pi/2} + \psi e^{-i\pi/2}) = -\gamma^\dagger \\ \gamma &\mapsto \frac{1}{2}(\psi^\dagger e^{i\pi/2} + \psi e^{-i\pi/2}) = -\gamma \end{aligned} \tag{E.25}$$

Enabled with this information, let us consider a vortex interchange σ_i braiding the Majorna zero modes (MZM) as shown in Fig. E.10 in a set of vortices $1, 2, \ldots N$. One of the MZM moves around another where it must cross a line where the phase for the other vortex jumps from 0 to 2π (a branch cut), so it picks up the phase as given in eq. (E.25) relative to the other. All the other vortices

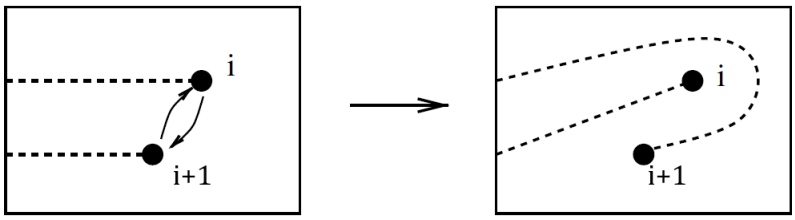

Figure E.10: Schematic for an elementary braid exchange. Figure adapted from [131]

remain unaffected. Hence the the elementary braid operation σ_i exchanging the positions of two vortices affects the MZMs as [131]

$$\sigma_i : \begin{cases} \gamma_i \mapsto \gamma_{i+1}, \\ \gamma_{i+1} \mapsto -\gamma_i \\ \gamma_j \mapsto \gamma_j \quad for j \neq i+1 and j \neq i \end{cases} \tag{E.26}$$

From the elementary braiding operation on the MZMs as given in eq.(E.26), it can be checked that the this representation satisfies the conditions for the braid group as given in eq. (E.22) and (E.23). Hence the MZM's in the core of half quantum vortices are part of the braid group! To construct the explicit operators acting on Hilbert space, we can create fermionic operators from MZMs and operate them on vacuum states. The condition we need to impose for an operator $\tau(T_i)$ is

$$\tau(T_i)\gamma_j \left[\tau(T_i)\right]^{-1} = T_i\gamma_j \tag{E.27}$$

where the action of operator T_i on γ_j is given in eq. (E.26). With the normalization condition $\{\gamma_i, \gamma_j\} = 2\delta_{ij}$, the expression for the braid operators for MZMs are given as [131]:

$$\tau(T_i) = \exp\left(\frac{\pi}{4}\gamma_{i+1}\gamma_i\right) = \frac{1}{\sqrt{2}}(1 + \gamma_{i+1}\gamma_i) \tag{E.28}$$

For example, in case of 2 vortices, we have 2 MZMs γ_1 and γ_2, which can lead

to only 1 fermion given by $\psi = (\gamma_1 + i\gamma_2)/2$, $\psi = (\gamma_1 - i\gamma_2)/2$. The ground state is doubly degenerate and the braid group has only one member which exchanges these and given as [131]:

$$\tau(T) = \exp(\pi/4\gamma_2\gamma_1) = \exp\left[i\frac{\pi}{4}(2\psi^\dagger\psi - 1)\right] = \exp\left(i\frac{\pi}{4}\sigma_z\right) \tag{E.29}$$

where σ_z is the Pauli matrix in basis $\left(|0\rangle, \psi^\dagger|0\rangle\right)$.

For the case of 4 vortices, we have 4 MZMs and 2 fermions given by $\psi_1 = (\gamma_! + i\gamma_2)/2$, $\psi_2 = (\gamma_3 + i\gamma_4)/2$ and the two hermitian conjugate operators $\psi_1^\dagger$ and $\psi_2^\dagger$. The ground state has a degeneracy of 4, hence there are 3 possible exchanges given by $\tau(T_i)$ operators as [131]:

$$\tau(T_1) = \begin{pmatrix} e^{-i\pi/4} & & & \\ & e^{i\pi/4} & & \\ & & e^{-i\pi/4} & \\ & & & e^{i\pi/4} \end{pmatrix}, \quad \tau(T_3) = \begin{pmatrix} e^{-i\pi/4} & & & \\ & e^{-i\pi/4} & & \\ & & e^{i\pi/4} & \\ & & & e^{i\pi/4} \end{pmatrix}$$

$$\tau(T_2) = \frac{1}{\sqrt{2}} \begin{pmatrix} 1 & 0 & 0 & -i \\ 0 & 1 & -i & 0 \\ 0 & -i & 1 & 0 \\ -i & 0 & 0 & 1 \end{pmatrix} \tag{E.30}$$

where the basis is $\left(|0\rangle, \psi_1^\dagger|0\rangle, \psi_2^\dagger|0\rangle, \psi_1^\dagger\psi_2^\dagger|0\rangle\right)$.

There are several key things to note from this discussion. First, all the exchange operators $\tau(T_i)$ are even in the fermion number. This is a reflection of underlying superconducting Hamiltonian which allows creation and destruction of electrons only in pairs. This means that a parity operator can be defined and the representations can be restricted to odd or even subsector, containing 2^{N-1} states. In each of these subspaces the representation operators $\tau(T_i)$ are

non-commuting and non-trivial. These properties are derived on the fact that a)MZM exists and b) MZM exchange is given by $\gamma \mapsto -\gamma$, which is possible because of the presence of a d-vector which rotates to compensate a phase of π resulting in the orbital part having a phase of π, to give a total phase of 2π for a phase winding around a vortex. Hence this is possible for a chiral odd-parity superconductor. These MZMs and braiding statistics do not rely on the exact form of the Hamiltonian, but overall topological structure, hence they are protected against local perturbations of the Hamiltonian and local disorder as long as the vortices survive. This is termed as topological protection.

Since Majorana zero modes exchange operators $\tau(T_i)$ discussed above follow non-abelian anyon statistics, they can be employed as qubits (quantum-bits) [136] for quantum computation [137, 135], where information can be encoded as states of non-abelian anyons and operations, can be performed by *braiding* multiple non-abelian anyons. After all the operations, the anyons can be fused to measure the final states. This quantum computing process is schematically depicted in Fig. E.11. Information encoded and processed in such a fashion is provided a topological protection (a braid cannot be destroyed easily until the thread is damaged by cutting!) and hence quantum computation using non-abelian anyons is also called topological quantum computation [138, 135] [For a popular and easy to follow article on topological quantum computation in Scientific American, see [139]].

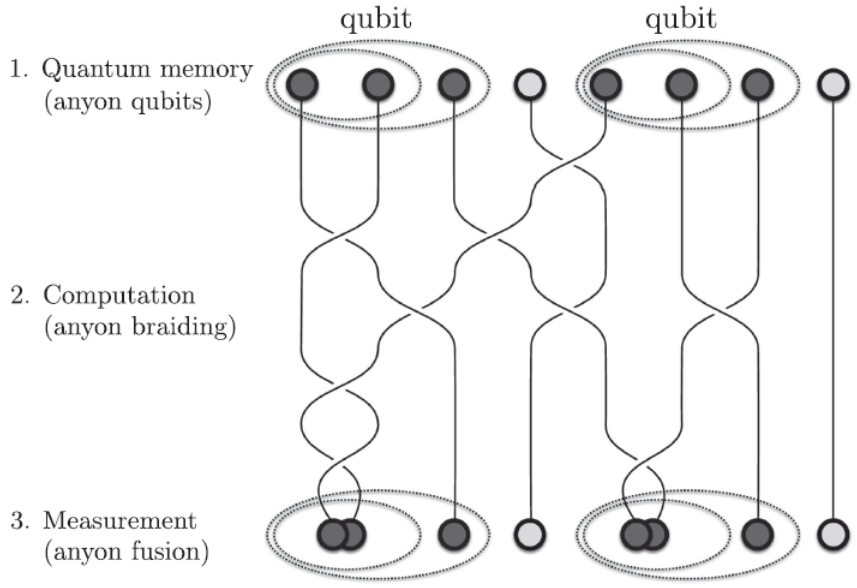

Figure E.11: Topological quantum computation using Non-Abelian anyons. This schematic shows two qubits each comprising of four anyons. The ellipses show anyons grouped into qubits to initialize the state. Braiding is performed to apply gates and eventually the anyons are fused to measure the final states. The light grey anyons are parts of qubits do not participate in computation and can be used for error-corrections. Figure reproduced from [140]

APPENDIX F

MATLAB SCRIPTS

F.1 T-matrix calculation for BSCCO

```
%script to calculate bqpi pattern using t-matrix formalism for bscco
%See  Wang and Lee QPI PRB  67, 020511(R) (2003)
n_q = 401; % number of points in k-space, odd for center to lie ...
   on a pixel
E = 0.024; %Energy in eV, code generates results from E to -E,
n_E = 12; % number of energy layers from E to -E, odd to have FS: E=0
tic
[qx,qy] = meshgrid(linspace(-1,1,n_q));
Epoints = linspace(-E,E,n_E);
I = eye(2);
Vs = 0.1;
Vm = 0.0;

% calculate TB model energies as per Wang and Lee QPI PRB  67,
% 020511(R) (2003), who used Norman
t1 = 0.1305;
t2 = -0.5951;
t3 = 0.1636;
t4 = -0.0519;
t5 = -0.1117;
t6 = 0.0510;
E_tb = t1 + t2*(cos(pi*qx)+cos(pi*qy))/2 ...
    +t3*cos(pi*qx).*cos(pi*qy)+ t4*(cos(2*pi*qx)+cos(2*pi*qy))/2 ...
    +t5*(cos(2*pi*qx).*cos(pi*qy)+cos(pi*qx).*cos(2*pi*qy))/2 ...
```

```
    + t6*cos(2*pi*qx).*cos(2*pi*qy);


% calculate gap function
D0 = 0.025;% gap max in meV
D = D0/2*(cos(pi*qx)-cos(pi*qy));

%calculate Green's function (2x2 matrix) for each k and E value
G11 = zeros(n_q,n_q,n_E);
G12 = zeros(n_q,n_q,n_E);
G21 = zeros(n_q,n_q,n_E);
G22 = zeros(n_q,n_q,n_E);
G11r = zeros(n_q,n_q,n_E);
G12r = zeros(n_q,n_q,n_E);
G22r= zeros(n_q,n_q,n_E);
G21r = zeros(n_q,n_q,n_E);
%broadening parameter,
%usually the bias modulation in dI/dV experiment
d=0.0015;
for k=1:n_E
    den = (Epoints(k)^2-E_tb.^2-D.^2-d^2+1i*2*Epoints(k)*d);
    G11(:,:,k) = (Epoints(k) + E_tb + 1i*d) ./den;
    G22(:,:,k) = (Epoints(k) - E_tb + 1i*d) ./den;
    G12(:,:,k) = D./den;
    G21(:,:,k) = G12(:,:,k);
    %get all G's in r-space for useful computations later
    G11r(:,:,k) = fftshift(fft2(G11(:,:,k)))/(n_q*n_q);
    G12r(:,:,k) = fftshift(fft2(G12(:,:,k)))/(n_q*n_q);
    G21r(:,:,k) = fftshift(fft2(G21(:,:,k)))/(n_q*n_q);
    G22r(:,:,k) = fftshift(fft2(G22(:,:,k)))/(n_q*n_q);
end
```

```
toc

%calculate T matrix
T11 = zeros(1,n_E);
T12 = zeros(1,n_E);
T21 = zeros(1,n_E);
T22 = zeros(1,n_E);
sumG_ind = (n_q+1)/2;
for k=1:n_E
    A = [Vs+Vm, 0.0;...
           0.0, -Vs+Vm];
    B = [G11r(sumG_ind,sumG_ind,k),G12r(sumG_ind,sumG_ind,k);...
        G21r(sumG_ind,sumG_ind,k),G22r(sumG_ind,sumG_ind,k)];
    C = I - A*B;
    T = A/C;
    T11(k) = T(1,1);
    T12(k) = T(1,2);
    T21(k) = T(2,1);
    T22(k) = T(2,2);
end
toc

%calculate A
A11r = zeros(n_q,n_q,n_E);
A22r = zeros(n_q,n_q,n_E);
for k=1:n_E
for i=1:n_q
for j=1:n_q
 A11r(i,j,k) = G11r(i,j,k)*T11(k)*G11r(n_q-i+1,n_q-j+1,k)...
             + G11r(i,j,k)*T12(k)*G21r(n_q-i+1,n_q-j+1,k)...
             + G12r(i,j,k)*T21(k)*G11r(n_q-i+1,n_q-j+1,k)...
             + G12r(i,j,k)*T22(k)*G21r(n_q-i+1,n_q-j+1,k);
```

```
 A22r(i,j,k) = G21r(i,j,k)*T11(k)*G12r(n_q-i+1,n_q-j+1,k)...
             + G21r(i,j,k)*T12(k)*G22r(n_q-i+1,n_q-j+1,k)...
             + G22r(i,j,k)*T21(k)*G12r(n_q-i+1,n_q-j+1,k)...
             + G22r(i,j,k)*T22(k)*G22r(n_q-i+1,n_q-j+1,k);
end
end
end
toc


%calculate dn, change in density of states
dnr = zeros(n_q,n_q,n_E);
dnq = zeros(n_q,n_q,n_E);
for k=1:n_E
    dnr(:,:,k) = -imag(A11r(:,:,k)+A22r(:,:,n_E-k+1))/pi/2 ;
    %calculate dnq, the bqpi pattern
    dnq(:,:,k) = fftshift(fft2(dnr(:,:,k)));
end
%calculate the spectral function Ak, for one spin
%(other will be symmetric)
Ak = -imag(G11);



% do some plotting to see the results
m = 4; %number of rows in subplot, note that m*n must be n_E
n = 3;%number of columns in subplot, note that m*n must be n_E
%define [vertical,horizontal]margins between the subplots
margins = [0.02,0.02];

height=(1-(m+1)*margins(1))/m; % single subplot height
```

```
width=(1-(n+1)*margins(2))/n;  % single subplot width
 %position of text relative to each subplot in fraction
text_left = 0.35;
%position of text relative to each subplot in fraction
text_bottom = 0.08;
text_font_size = 8;
text_color = 'r';

% plot Ak
figure
colorscale = 'gray';
for k=1:n_E
 [subplot_row,subplot_col] = ind2sub([m,n],k);
 % merged subplot bottom position
 bottom=(m-(subplot_row))*(height+margins(1)) +margins(1);
 % merged subplot left position
 left=(subplot_col)*(width+margins(2))-width;
 subplot('Position',[left,bottom,width,height])
 %set colorbar limits
 Akk = Ak(:,:,k);
  cl2 = max(Akk(:))/10;
  cl1 = min(Akk(:))/10;
 imagesc(Ak(:,:,k));colormap(colorscale);axis equal;axis off;
 caxis([cl1,cl2]);
 text(text_left,text_bottom,[num2str(1000*Epoints(k),'%6.2f'),...
     ' meV'],'Units','normalized','Fontsize',text_font_size,...
     'Color',text_color,'FontWeight','Bold');
end
suptitle('Spectral Function A(k)')


% plot dnr
```

```
figure
colorscale = 'gray';
for k=1:n_E
 [subplot_row,subplot_col] = ind2sub([m,n],k);
  % merged subplot bottom position
 bottom=(m-(subplot_row))*(height+margins(1)) +margins(1);
 % merged subplot left position
 left=(subplot_col)*(width+margins(2))-width;
 subplot('Position',[left,bottom,width,height])
 dnrk = dnr(:,:,k);
 %set colorbar limits
cl2 = max(dnrk(:))/10;
cl1 = min(dnrk(:))/10;
 imagesc(dnr(:,:,k));colormap(colorscale);axis equal;axis off;
 caxis([cl1,cl2]);
 text(text_left,text_bottom,[num2str(1000*Epoints(k),'%6.2f'),...
     ' meV'],'Units','normalized','Fontsize',text_font_size,...
     'Color',text_color,'FontWeight','Bold');
end
suptitle('Real space BQPI \a N(r)')

% plot dnq
figure
colorscale = 'gray';

for k=1:n_E
 [subplot_row,subplot_col] = ind2sub([m,n],k);
 % merged subplot bottom position
 bottom=(m-(subplot_row))*(height+margins(1)) +margins(1);
 % merged subplot left position
 left=(subplot_col)*(width+margins(2))-width;
 subplot('Position',[left,bottom,width,height])
```

```
 dnqk = dnq(:,:,k);
 %set colorbar limits
    cl2 = max(abs(dnqk(:)))/2;
    cl1 = min(abs(dnqk(:)))/2;
 imagesc(abs(dnq(:,:,k)));colormap(colorscale);axis equal;axis off;
 caxis([cl1,cl2]);
 text(text_left,text_bottom,[num2str(1000*Epoints(k),'%6.2f'),...
     ' meV'],'Units','normalized','Fontsize',text_font_size,...
     'Color',text_color,'FontWeight','Bold');
end
suptitle('Fourier Transoform of real space BQPI \a N(q)')
```

F.2 Demonstration of Multi Atom Fourier Transform

```
%script to generate and analyze Freidel oscillation
%cos(k0r+phi)/r^2
clear
N=100; % number of impurities
npx = 512; % number of pixels for simulation
r = 1:1:npx;
[rx,ry] = meshgrid(r,r);
%create the windowing function
x = linspace(0,pi,npx);
y = linspace(0,pi,npx);
w = sin(x)'*sin(y);
%define the center of the grid
if mod(npx, 2) == 0
    cpx = npx/2 + 1;
else
    cpx = (npx-1)/2 + 1;
```

```
end
%define k-space
kx = 1/npx*(rx-cpx);
ky = 1/npx*(ry-cpx);

k0 = [1,0]; % set k0
kappa=0;
%set what limits you want to randomize the impurity to,
%usually it is good to avoid boundaries,
%hence the floor(npx/10) term, set it as needed
minX = min(r)+floor(npx/10);
maxX = max(r)-floor(npx/10);

%set phi
phi = 0;
%get random coordinates for the defect
%within min and max limits set in
%lines 23-24
x0 = floor((maxX-minX)*rand(N,1)+minX);
y0 = floor((maxX-minX)*rand(N,1)+minX);
dnr = zeros(npx,npx);
dnqC = zeros(npx,npx);
%%%Generate signal
for n=1:N
      ys = cos(norm(k0)*sqrt((rx-x0(n)).^2+(ry-y0(n)).^2)+phi)./ ...
      (sqrt((rx-x0(n)).^2+(ry-y0(n)).^2)).^2 ...
  .*exp(-kappa*sqrt((rx-x0(n)).^2+(ry-y0(n)).^2));
  %set infinity values at origin to 1, that's how sinc does it
  ys(isinf(ys)) = cos(phi)*1;
  dnr = dnr + ys;
end
dnr = dnr/N; %noramlize by number of defects
```

```
% Correct signal with shift theorem
  %shift  is from center [x0-cpx,y0-cpx]
  for n=1:N
    sftr = exp(1i*2*pi*(kx*(x0(n)-cpx)+ky*(y0(n)-cpx)));
    yq = fftshift(fft2(ifftshift(dnr)));
    sft_yq = yq.*sftr; %shifted in q-space
    %bring back to real space by ifft and multiple by sine window
    wind_sft_yq = ifftshift(fftshift(ifft2(ifftshift(sft_yq))).*w);
    %take fft again of the windowed data
    ft_wind_sft_yq = fftshift(fft2(wind_sft_yq));
    dnqC = dnqC +  ft_wind_sft_yq;
  end
dnq = fftshift(fft2(dnr));
dnrC = real(fftshift(ifft2(ifftshift(dnqC))));

%perform azimuthal integration
 for i=cpx:-1:2
     mask = circlematrix([npx,npx],i,cpx,cpx)...
         -circlematrix([npx,npx],i-1,cpx,cpx);
     real_dnq_curve(i) = sum(sum(mask.*real(dnq)));
     imag_dnq_curve(i) = sum(sum(mask.*imag(dnq)));
     real_dnqC_curve(i) = sum(sum(mask.*real(dnqC)));
     imag_dnqC_curve(i) = sum(sum(mask.*imag(dnqC)));
 end


figure;
%plot the dnr before correction
subplot(1,2,1)
imagesc(dnr);axis equal; axis off;colormap('gray');
caxis([-0.002,0.002])
```

```
% caxis([min(dnr(:)),max(dnr(:))]/100);
title(gca,'\Δ N(r)')
%plot the dnr after correction, this makes sense only for N=1, for
%multiple defects, this will show sum of more than one images
subplot(1,2,2)
imagesc(dnrC);axis equal; axis off;colormap('gray');
caxis([-0.002,0.002])
% caxis([min(dnrC(:)),max(dnrC(:))]/100);
title(gca,'Shift Corrected \Δ N(r)')
suptitle('Real space Friedel oscillations')

% define a three color colormap with 0 in the middle
%to be able to see sign
% we choose to go from Red [1,0,0] to White [1,1,1] to Blue [0,0,1]
rwb = [linspace(1,1,128),linspace(1,0,128);
    linspace(0,1,128),linspace(1,0,128);
    linspace(0,1,128),linspace(1,1,128);
    ];
rwb = rwb';
figure;
%Plot Fourier transform of Friedel oscillations
subplot(2,2,1)
imagesc(real(dnq));axis equal; axis off; colormap(rwb);
caxis([-3,3])
title(gca,'Re\Δ N(q)')
subplot(2,2,2)
imagesc(real(dnq));axis equal; axis off; colormap(rwb);
caxis([-3,3])
title(gca,'Im\Δ N(q)')

%Plot Multiple Atom Fourier transform of Friedel oscillations
subplot(2,2,3)
```

```
imagesc(real(dnqC));axis equal; axis off; colormap(rwb);
caxis([-10,10])
title(gca,'Re\Δ N_{MA}(q)')
subplot(2,2,4)
imagesc(imag(dnqC));axis equal; axis off; colormap(rwb);
caxis([-1,1])
title(gca,'Re\Δ N_{MA}(r)')
suptitle('Fourier Transform and Multi Atom Fourier Transform of ...
    the Freidel oscillations')

%plot azimuthally integrated signal
figure
subplot(1,2,1)
hold on
plot([86 ...
    86],[min(real_dnq_curve),max(real_dnq_curve)],'-k','Linewidth',2)
plot(real_dnq_curve,'r','Linewidth',1)
xlabel('q (a.u.)')
ylabel('Re\Δ N(q) (a.u.)','FontSize',20)
set(gca,'Xtick',[],'FontSize',16)
axis square
box on
axis tight

subplot(1,2,2)
hold on
plot([86 ...
    86],[min(real_dnqC_curve),max(real_dnqC_curve)],'-k','Linewidth',2)
plot(real_dnqC_curve,'b','Linewidth',1)
xlabel('q (a.u.)')
ylabel('Re\Δ N_{MA}(q) (a.u.)','FontSize',20)
set(gca,'Xtick',[],'FontSize',16)
```

```
axis square
box on
axis tight
```

BIBLIOGRAPHY

[1] Dirk van Delft and Peter Kes. The discovery of superconductivity. *Physics Today*, 63:38, Sept 2010. doi:10.1063/1.3490499. URL https://physicstoday.scitation.org/doi/10.1063/1.3490499.

[2] J. Bardeen, L. N. Cooper, and J. R. Schrieffer. Theory of Superconductivity. *Phys. Rev.*, 108:1175–1204, Dec 1957. doi:10.1103/PhysRev.108.1175. URL https://link.aps.org/doi/10.1103/PhysRev.108.1175.

[3] Leon N. Cooper. Bound Electron Pairs in a Degenerate Fermi Gas. *Phys. Rev.*, 104:1189–1190, Nov 1956. doi:10.1103/PhysRev.104.1189. URL https://link.aps.org/doi/10.1103/PhysRev.104.1189.

[4] Michael Tinkham. *Introduction to Superconductivity*. Dover Publications, 2 edition, June 2004. ISBN 0486435032. URL http://www.worldcat.org/isbn/0486435032.

[5] H. Fröhlich. Theory of the Superconducting State. I. The Ground State at the Absolute Zero of Temperature. *Phys. Rev.*, 79:845–856, Sep 1950. doi:10.1103/PhysRev.79.845. URL https://link.aps.org/doi/10.1103/PhysRev.79.845.

[6] P. Morel and P. W. Anderson. Calculation of the Superconducting State Parameters with Retarded Electron-Phonon Interaction. *Phys. Rev.*, 125:1263–1271, Feb 1962. doi:10.1103/PhysRev.125.1263. URL https://link.aps.org/doi/10.1103/PhysRev.125.1263.

[7] Piers Coleman. *Introduction to Many-Body Physics*. Cambridge University Press, 2015. doi:10.1017/CBO9781139020916.

[8] Henrik Bruus and Karsten Flensberg. *Many-Body Quantum Theory in Condensed Matter Physics*. Oxford University Press, 2004. ISBN 9780198566335.

[9] N.N. Bogoliubov. A New Method in the Theory of Superconductivity. *Journal of Experimental and Theoretical Physics*, 7:41, July 1958. URL http://www.jetp.ac.ru/cgi-bin/e/index/e/7/1/p41?a=list.

[10] J. G. Valatin. Comments on the theory of superconductivity. *Il Nuovo Cimento (1955-1965)*, 7(6):843–857, 1958. ISSN 1827-6121. doi:10.1007/BF02745589. URL https://doi.org/10.1007/BF02745589.

[11] Douglas D. Osheroff. Superfluidity in ^{3}He: Discovery and understanding. *Rev. Mod. Phys.*, 69:667–682, Jul 1997. doi:10.1103/RevModPhys.69.667. URL https://link.aps.org/doi/10.1103/RevModPhys.69.667.

[12] Anthony J. Leggett. *Quantum Liquids*. Oxford Graduate Texts. Oxford University Press, 2006.

[13] Patrick A. Lee, Naoto Nagaosa, and Xiao-Gang Wen. Doping a Mott insulator: Physics of high-temperature superconductivity. *Rev. Mod. Phys.*, 78:17–85, Jan 2006. doi:10.1103/RevModPhys.78.17. URL https://link.aps.org/doi/10.1103/RevModPhys.78.17.

[14] J. C. Davis and R. E. Packard. Superfluid ^{3}He Josephson weak links. *Rev. Mod. Phys.*, 74:741–773, Jul 2002. doi:10.1103/RevModPhys.74.741. URL https://link.aps.org/doi/10.1103/RevModPhys.74.741.

[15] Michael R. Norman. The Challenge of Unconventional Superconductivity. *Science*, 332(6026):196–200, 2011. ISSN 0036-8075.

doi:10.1126/science.1200181. URL https://science.sciencemag.org/content/332/6026/196.

[16] James E. Annett. *Superconductivity, Superfluids and Condensates*. Oxford University Press, 2004.

[17] Andrew Peter Mackenzie and Yoshiteru Maeno. The superconductivity of Sr_2RuO_4 and the physics of spin-triplet pairing. *Rev. Mod. Phys.*, 75:657–712, May 2003. doi:10.1103/RevModPhys.75.657. URL https://link.aps.org/doi/10.1103/RevModPhys.75.657.

[18] Yoshiteru Maeno, Shunichiro Kittaka, Takuji Nomura, Shingo Yonezawa, and Kenji Ishida. Evaluation of Spin-Triplet Superconductivity in Sr_2RuO_4. *Journal of the Physical Society of Japan*, 81(1):011009, 2012. doi:10.1143/JPSJ.81.011009. URL https://doi.org/10.1143/JPSJ.81.011009.

[19] J. E. Hoffman, K. McElroy, D.-H. Lee, K. M Lang, H. Eisaki, S. Uchida, and J. C. Davis. Imaging Quasiparticle Interference in $Bi_2Sr_2CaCu_2O8 + \delta$. *Science*, 297(5584):1148–1151, 2002. ISSN 0036-8075. doi:10.1126/science.1072640. URL https://science.sciencemag.org/content/297/5584/1148.

[20] Makoto Hashimoto, Inna M. Vishik, Rui-Hua He, Thomas P. Devereaux, and Zhi-Xun Shen. Energy gaps in high-transition-temperature cuprate superconductors. *Nature Physics*, 10(7):483–495, 2014. ISSN 1745-2481. doi:10.1038/nphys3009. URL https://doi.org/10.1038/nphys3009.

[21] James F. Annett. Unconventional superconductivity. *Contemporary*

Physics, 36(6):423–437, 1995. doi:10.1080/00107519508232300. URL https://doi.org/10.1080/00107519508232300.

[22] Manfred Sigrist and Kazuo Ueda. Phenomenological theory of unconventional superconductivity. *Rev. Mod. Phys.*, 63:239–311, Apr 1991. doi:10.1103/RevModPhys.63.239. URL https://link.aps.org/doi/10.1103/RevModPhys.63.239.

[23] Eduardo Fradkin, Steven A. Kivelson, and John M. Tranquada. Colloquium: Theory of intertwined orders in high temperature superconductors. *Rev. Mod. Phys.*, 87:457–482, May 2015. doi:10.1103/RevModPhys.87.457. URL https://link.aps.org/doi/10.1103/RevModPhys.87.457.

[24] M. H. Hamidian, S. D. Edkins, Sang Hyun Joo, A. Kostin, H. Eisaki, S. Uchida, M. J. Lawler, E.-A. Kim, A. P. Mackenzie, K. Fujita, Jinho Lee, and J. C. SÃ©amus Davis. Detection of a Cooper-pair density wave in $Bi_2Sr_2CaCu_2O_8 + x$. *Nature*, 532(7599):343–347, 2016. ISSN 1476-4687. doi:10.1038/nature17411. URL https://doi.org/10.1038/nature17411.

[25] Zengyi Du, Hui Li, Sang Hyun Joo, Elizabeth P. Donoway, Jinho Lee, J. C. SÃ©amus Davis, Genda Gu, Peter D. Johnson, and Kazuhiro Fujita. Imaging the energy gap modulations of the cuprate pair-density-wave state. *Nature*, 580(7801):65–70, 2020. ISSN 1476-4687. doi:10.1038/s41586-020-2143-x. URL https://doi.org/10.1038/s41586-020-2143-x.

[26] Jacob Linder and Alexander V. Balatsky. Odd-frequency superconductivity. *Rev. Mod. Phys.*, 91:045005, Dec 2019.

doi:10.1103/RevModPhys.91.045005. URL https://link.aps.org/doi/10.1103/RevModPhys.91.045005.

[27] L. D. Landau and L. M. Lifshitz. *Quantum Mechanics Non-Relativistic Theory, Third Edition: Volume 3*. Butterworth-Heinemann, January 1981. ISBN 0750635398. doi:https://doi.org/10.1002/zamm.19590390514. URL https://onlinelibrary.wiley.com/doi/abs/10.1002/zamm.19590390514.

[28] Mildred S. Dresselhaus, Gene Dresselhaus, and Ado Jorio. *Group Theory: Application to the Physics of Condensed Matter*. Springer, 2008. ISBN 9783540328971.

[29] S.-O. Kaba and D. Sénéchal. Group-theoretical classification of superconducting states of strontium ruthenate. *Phys. Rev. B*, 100:214507, Dec 2019. doi:10.1103/PhysRevB.100.214507. URL https://link.aps.org/doi/10.1103/PhysRevB.100.214507.

[30] Kazuhiro Fujita, Andrew R. Schmidt, Eun-Ah Kim, Michael J. Lawler, Dung Hai Lee, J. C. Davis, Hiroshi Eisaki, and Shin-ichi Uchida. Spectroscopic Imaging Scanning Tunneling Microscopy Studies of Electronic Structure in the Superconducting and Pseudogap Phases of Cuprate High-Tc Superconductors. *Journal of the Physical Society of Japan*, 81(1): 011005, 2012. doi:10.1143/JPSJ.81.011005. URL https://doi.org/10.1143/JPSJ.81.011005.

[31] Ali Yazdani, Eduardo H. da Silva Neto, and Pegor Aynajian. Spectroscopic Imaging of Strongly Correlated Electronic States. *Annual Review of Condensed Matter Physics*, 7(1):11–33, 2016.

doi:10.1146/annurev-conmatphys-031214-014529. URL https://doi.org/10.1146/annurev-conmatphys-031214-014529.

[32] Kazuhiro Fujita, Mohammad H. Hamidian, Peter O. Sprau, Stephen D. Edkins, and J.C. Séamus Davis. *Visualizing Electronic Quantum Matter*, pages 1369–1390. Springer International Publishing, Cham, 2019. doi:10.1007/978-3-030-00069-1_28. URL https://doi.org/10.1007/978-3-030-00069-1_28.

[33] Samir Lounis. Theory of Scanning Tunneling Microscopy, 2014.

[34] J. Bardeen. Tunnelling from a Many-Particle Point of View. *Phys. Rev. Lett.*, 6:57–59, Jan 1961. doi:10.1103/PhysRevLett.6.57. URL https://link.aps.org/doi/10.1103/PhysRevLett.6.57.

[35] David J. Griffiths and Darrell F. Schroeter. *Introduction to Quantum Mechanics*. Cambridge University Press, 3 edition, 2018. doi:10.1017/9781316995433.

[36] Julian C. Chen. *Introduction to Scanning Tunneling Microscopy*. Oxford Press, 2 edition, 2007. doi:10.1093/acprof:oso/9780199211500.001.0001.

[37] Curry Taylor. *Coexistence of Bogoliubov Quasiparticles and Cluster Domains in Lightly Hole-Doped Cuprates*. PhD thesis, Cornell University, Ithaca, NY 14853, 2008.

[38] S. H. Pan, E. W. Hudson, and J. C. Davis. 3He refrigerator based very low temperature scanning tunneling microscope. *Review of Scientific Instruments*, 70(2):1459–1463, 1999. doi:10.1063/1.1149605. URL https://doi.org/10.1063/1.1149605.

[39] P. O. Sprau, A. Kostin, A. Kreisel, A. E. Böhmer, V. Taufour, P. C. Canfield, S. Mukherjee, P. J. Hirschfeld, B. M. Andersen, and J. C. Séamus Davis. Discovery of orbital-selective Cooper pairing in FeSe. *Science*, 357(6346): 75–80, 2017. ISSN 0036-8075. doi:10.1126/science.aal1575. URL https://science.sciencemag.org/content/357/6346/75.

[40] P. J. Hirschfeld, D. Altenfeld, I. Eremin, and I. I. Mazin. Publisher's Note: Robust determination of the superconducting gap sign structure via quasiparticle interference [Phys. Rev. B 92, 184513 (2015)]. *Phys. Rev. B*, 94:179905, Nov 2016. doi:10.1103/PhysRevB.94.179905. URL https://link.aps.org/doi/10.1103/PhysRevB.94.179905.

[41] N.W. Ashcroft and N.D. Mermin. *Solid State Physics*. Saunders College, Philadelphia, 1976.

[42] Andrea Damascelli, Zahid Hussain, and Zhi-Xun Shen. Angle-resolved photoemission studies of the cuprate superconductors. *Rev. Mod. Phys.*, 75:473–541, Apr 2003. doi:10.1103/RevModPhys.75.473. URL https://link.aps.org/doi/10.1103/RevModPhys.75.473.

[43] Pedram Roushan, Jungpil Seo, Colin V. Parker, Y. S. Hor, D. Hsieh, Dong Qian, Anthony Richardella, M. Z. Hasan, R. J. Cava, and Ali Yazdani. Topological surface states protected from backscattering by chiral spin texture. *Nature*, 460(7259):1106–1109, Aug 2009. ISSN 1476-4687. doi:10.1038/nature08308. URL https://doi.org/10.1038/nature08308.

[44] A. R. Schmidt, M. H. Hamidian, P. Wahl, F. Meier, A. V. Balatsky, J. D. Garrett, T. J. Williams, G. M. Luke, and J. C. Davis. Imaging the Fano

lattice to â€hidden orderâ€™ transition in URu_2Si_2. *Nature*, 465(7298):570–576, Jun 2010. ISSN 1476-4687. doi:10.1038/nature09073. URL https://doi.org/10.1038/nature09073.

[45] J. E. Hoffman, K. McElroy, D.-H. Lee, K. M Lang, H. Eisaki, S. Uchida, and J. C. Davis. Imaging Quasiparticle Interference in $Bi_2Sr_2CaCu_2O_{8+\delta}$. *Science*, 297(5584):1148–1151, 2002. doi:10.1126/science.1072640.

[46] M Allan, Andreas Rost, A Mackenzie, Yang Xie, J Davis, K. Kihou, Chih-Hao Lee, A Iyo, H Eisaki, and Tien-Ming Chuang. Anisotropic Energy Gaps of Iron-Based Superconductivity from Intraband Quasiparticle Interference in LiFeAs. *Science*, 336:563–7, 05 2012. doi:10.1126/science.1218726.

[47] M. P. Allan, F. Massee, D. K. Morr, J. Van Dyke, A. W. Rost, A. P. Mackenzie, C. Petrovic, and J. C. Davis. Imaging Cooper pairing of heavy fermions in $CeCoIn_5$. *Nature Physics*, 9(8):468–473, Aug 2013. ISSN 1745-2481. doi:10.1038/nphys2671. URL https://doi.org/10.1038/nphys2671.

[48] Rahul Sharma, Stephen D. Edkins, Zhenyu Wang, Andrey Kostin, Chanchal Sow, Yoshiteru Maeno, Andrew P. Mackenzie, J. C. Séamus Davis, and Vidya Madhavan. Momentum-resolved superconducting energy gaps of sr_2ruo_4 from quasiparticle interference imaging. *Proceedings of the National Academy of Sciences*, 117(10):5222–5227, 2020. ISSN 0027-8424. doi:10.1073/pnas.1916463117. URL https://www.pnas.org/content/117/10/5222.

[49] A. V. Balatsky, I. Vekhter, and Jian-Xin Zhu. Impurity-induced states in conventional and unconventional superconductors. *Rev. Mod. Phys.*, 78:

373–433, May 2006. doi:10.1103/RevModPhys.78.373. URL https://link.aps.org/doi/10.1103/RevModPhys.78.373.

[50] Qiang-Hua Wang and Dung-Hai Lee. Quasiparticle scattering interference in high-temperature superconductors. *Phys. Rev. B*, 67:020511, Jan 2003. doi:10.1103/PhysRevB.67.020511. URL https://link.aps.org/doi/10.1103/PhysRevB.67.020511.

[51] Y. Maeno, H. Hashimoto, K. Yoshida, S. Nishizaki, T. Fujita, J. G. Bednorz, and F. Lichtenberg. Superconductivity in a layered perovskite without copper. *Nature*, 372(6506):532–534, 1994. ISSN 1476-4687. doi:10.1038/372532a0. URL https://doi.org/10.1038/372532a0.

[52] Andrew P. Mackenzie, Thomas Scaffidi, Clifford W. Hicks, and Yoshiteru Maeno. Even odder after twenty-three years: the superconducting order parameter puzzle of Sr2RuO4. *npj Quantum Materials*, 2(1):40, 2017. ISSN 2397-4648. doi:10.1038/s41535-017-0045-4. URL https://doi.org/10.1038/s41535-017-0045-4.

[53] A. P. Mackenzie, R. K. W. Haselwimmer, A. W. Tyler, G. G. Lonzarich, Y. Mori, S. Nishizaki, and Y. Maeno. Extremely Strong Dependence of Superconductivity on Disorder in Sr_2RuO_4. *Phys. Rev. Lett.*, 80:161–164, Jan 1998. doi:10.1103/PhysRevLett.80.161. URL https://link.aps.org/doi/10.1103/PhysRevLett.80.161.

[54] A. P. Mackenzie, S. R. Julian, A. J. Diver, G. J. McMullan, M. P. Ray, G. G. Lonzarich, Y. Maeno, S. Nishizaki, and T. Fujita. Quantum Oscillations in the Layered Perovskite Superconductor Sr_2RuO_4. *Phys. Rev. Lett.*, 76:3786–3789, May 1996. doi:10.1103/PhysRevLett.76.3786. URL https://link.aps.org/doi/10.1103/PhysRevLett.76.3786.

[55] C. Bergemann, S. R. Julian, A. P. Mackenzie, S. NishiZaki, and Y. Maeno. Detailed Topography of the Fermi Surface of Sr_2RuO_4. *Phys. Rev. Lett.*, 84:2662–2665, Mar 2000. doi:10.1103/PhysRevLett.84.2662. URL https://link.aps.org/doi/10.1103/PhysRevLett.84.2662.

[56] A. Damascelli, D. H. Lu, K. M. Shen, N. P. Armitage, F. Ronning, D. L. Feng, C. Kim, Z.-X. Shen, T. Kimura, Y. Tokura, Z. Q. Mao, and Y. Maeno. Fermi Surface, Surface States, and Surface Reconstruction in Sr_2RuO_4. *Phys. Rev. Lett.*, 85:5194–5197, Dec 2000. doi:10.1103/PhysRevLett.85.5194. URL https://link.aps.org/doi/10.1103/PhysRevLett.85.5194.

[57] T. M. Rice and M. Sigrist. Sr2RuO4: an electronic analogue of3He? *Journal of Physics: Condensed Matter*, 7(47):L643–L648, nov 1995. doi:10.1088/0953-8984/7/47/002. URL https://doi.org/10.1088%2F0953-8984%2F7%2F47%2F002.

[58] N. D. Mermin. The topological theory of defects in ordered media. *Rev. Mod. Phys.*, 51:591–648, Jul 1979. doi:10.1103/RevModPhys.51.591. URL https://link.aps.org/doi/10.1103/RevModPhys.51.591.

[59] W. D. Knight. Nuclear Magnetic Resonance Shift in Metals. *Phys. Rev.*, 76:1259–1260, Oct 1949. doi:10.1103/PhysRev.76.1259.2. URL https://link.aps.org/doi/10.1103/PhysRev.76.1259.2.

[60] K. Ishida, H. Mukuda, Y. Kitaoka, K. Asayama, Z. Q. Mao, Y. Mori, and Y. Maeno. Spin-triplet superconductivity in sr_2ruo_4 identified by ^{17}o knight shift. *Nature*, 396(6712):658–660, Dec 1998. doi:10.1038/25315.

[61] G. M. Luke, Y. Fudamoto, K. M. Kojima, M. I. Larkin, J. Merrin,

B. Nachumi, Y. J. Uemura, Y. Maeno, Z. Q. Mao, Y. Mori, H. Nakamura, and M. Sigrist. Time-reversal symmetry-breaking superconductivity in Sr_2RuO_4. *Nature*, 394(6693):558–561, 1998. ISSN 1476-4687. doi:10.1038/29038. URL https://doi.org/10.1038/29038.

[62] Jing Xia, Yoshiteru Maeno, Peter T. Beyersdorf, M. M. Fejer, and Aharon Kapitulnik. High Resolution Polar Kerr Effect Measurements of Sr_2RuO_4: Evidence for Broken Time-Reversal Symmetry in the Superconducting State. *Phys. Rev. Lett.*, 97:167002, Oct 2006. doi:10.1103/PhysRevLett.97.167002. URL https://link.aps.org/doi/10.1103/PhysRevLett.97.167002.

[63] Shuji NishiZaki, Yoshiteru Maeno, and Zhiqiang Mao. Changes in the Superconducting State of Sr 2RuO 4 under Magnetic Fields Probed by Specific Heat. *Journal of the Physical Society of Japan*, 69(2):572–578, 2000. doi:10.1143/JPSJ.69.572. URL https://doi.org/10.1143/JPSJ.69.572.

[64] I. Bonalde, Brian D. Yanoff, M. B. Salamon, D. J. Van Harlingen, E. M. E. Chia, Z. Q. Mao, and Y. Maeno. Temperature Dependence of the Penetration Depth in Sr_2RuO_4: Evidence for Nodes in the Gap Function. *Phys. Rev. Lett.*, 85:4775–4778, Nov 2000. doi:10.1103/PhysRevLett.85.4775. URL https://link.aps.org/doi/10.1103/PhysRevLett.85.4775.

[65] C. Lupien, W. A. MacFarlane, Cyril Proust, Louis Taillefer, Z. Q. Mao, and Y. Maeno. Ultrasound Attenuation in Sr_2RuO_4: An Angle-Resolved Study of the Superconducting Gap Function. *Phys. Rev. Lett.*, 86:5986–5989, Jun 2001. doi:10.1103/PhysRevLett.86.5986. URL https://link.aps.org/doi/10.1103/PhysRevLett.86.5986.

[66] K. Deguchi, Z. Q. Mao, H. Yaguchi, and Y. Maeno. Gap Structure of the Spin-Triplet Superconductor Sr_2RuO_4 Determined from the Field-Orientation Dependence of the Specific Heat. *Phys. Rev. Lett.*, 92:047002, Jan 2004. doi:10.1103/PhysRevLett.92.047002. URL https://link.aps.org/doi/10.1103/PhysRevLett.92.047002.

[67] D. F. Agterberg, T. M. Rice, and M. Sigrist. Orbital Dependent Superconductivity in Sr_2RuO_4. *Phys. Rev. Lett.*, 78:3374–3377, Apr 1997. doi:10.1103/PhysRevLett.78.3374. URL https://link.aps.org/doi/10.1103/PhysRevLett.78.3374.

[68] M. E. Zhitomirsky and T. M. Rice. Interband Proximity Effect and Nodes of Superconducting Gap in Sr_2RuO_4. *Phys. Rev. Lett.*, 87:057001, Jul 2001. doi:10.1103/PhysRevLett.87.057001. URL https://link.aps.org/doi/10.1103/PhysRevLett.87.057001.

[69] Yoichi Yanase, Takanobu Jujo, Takuji Nomura, Hiroaki Ikeda, Takashi Hotta, and Kosaku Yamada. Theory of superconductivity in strongly correlated electron systems. *Physics Reports*, 387(1):1 – 149, 2003. ISSN 0370-1573. doi:https://doi.org/10.1016/j.physrep.2003.07.002. URL http://www.sciencedirect.com/science/article/pii/S0370157303003235.

[70] Takuji Nomura and Kosaku Yamada. Roles of Electron Correlations in the Spin-Triplet Superconductivity of Sr_2RuO_4. *Journal of the Physical Society of Japan*, 71(8):1993–2004, 2002. doi:10.1143/JPSJ.71.1993. URL https://doi.org/10.1143/JPSJ.71.1993.

[71] Takuji Nomura and Kosaku Yamada. Detailed Investigation of Gap Structure and Specific Heat in the p-wave Superconductor Sr_2RuO_4. *Journal of*

the Physical Society of Japan, 71(2):404–407, 2002. doi:10.1143/JPSJ.71.404. URL https://doi.org/10.1143/JPSJ.71.404.

[72] K. Miyake and O. Narikiyo. Model for Unconventional Superconductivity of Sr_2RuO_4: Effect of Impurity Scattering on Time-Reversal Breaking Triplet Pairing with a Tiny Gap. *Phys. Rev. Lett.*, 83:1423–1426, Aug 1999. doi:10.1103/PhysRevLett.83.1423. URL https://link.aps.org/doi/10.1103/PhysRevLett.83.1423.

[73] Clifford W. Hicks, John R. Kirtley, Thomas M. Lippman, Nicholas C. Koshnick, Martin E. Huber, Yoshiteru Maeno, William M. Yuhasz, M. Brian Maple, and Kathryn A. Moler. Limits on superconductivity-related magnetization in Sr_2RuO_4 and $PrOs_4Sb_{12}$ from scanning SQUID microscopy. *Phys. Rev. B*, 81:214501, Jun 2010. doi:10.1103/PhysRevB.81.214501. URL https://link.aps.org/doi/10.1103/PhysRevB.81.214501.

[74] P. J. Curran, S. J. Bending, W. M. Desoky, A. S. Gibbs, S. L. Lee, and A. P. Mackenzie. Search for spontaneous edge currents and vortex imaging in Sr_2RuO_4 mesostructures. *Phys. Rev. B*, 89:144504, Apr 2014. doi:10.1103/PhysRevB.89.144504. URL https://link.aps.org/doi/10.1103/PhysRevB.89.144504.

[75] P. J. Curran, V. V. Khotkevych, S. J. Bending, A. S. Gibbs, S. L. Lee, and A. P. Mackenzie. Vortex imaging and vortex lattice transitions in superconducting Sr_2RuO_4 single crystals. *Phys. Rev. B*, 84:104507, Sep 2011. doi:10.1103/PhysRevB.84.104507. URL https://link.aps.org/doi/10.1103/PhysRevB.84.104507.

[76] I. A. Firmo, S. Lederer, C. Lupien, A. P. Mackenzie, J. C. Davis, and

S. A. Kivelson. Evidence from tunneling spectroscopy for a quasi-one-dimensional origin of superconductivity in Sr_2RuO_4. *Phys. Rev. B*, 88: 134521, Oct 2013. doi:10.1103/PhysRevB.88.134521. URL https://link.aps.org/doi/10.1103/PhysRevB.88.134521.

[77] S. Raghu, A. Kapitulnik, and S. A. Kivelson. Hidden Quasi-One-Dimensional Superconductivity in Sr_2RuO_4. *Phys. Rev. Lett.*, 105:136401, Sep 2010. doi:10.1103/PhysRevLett.105.136401. URL https://link.aps.org/doi/10.1103/PhysRevLett.105.136401.

[78] S Raghu, Suk Bum Chung, and Samuel Lederer. Theory of hidden quasi-1D superconductivity in Sr2RuO4. *Journal of Physics: Conference Series*, 449:012031, jul 2013. doi:10.1088/1742-6596/449/1/012031. URL https://doi.org/10.1088.

[79] Z.Q. Mao, Y. Maeno, and H. Fukazawa. Crystal growth of sr2ruo4. *Materials Research Bulletin*, 35(11):1813 – 1824, 2000. ISSN 0025-5408. doi:https://doi.org/10.1016/S0025-5408(00)00378-0. URL http://www.sciencedirect.com/science/article/pii/S0025540800003780.

[80] Zhenyu Wang, Daniel Walkup, Philip Derry, Thomas Scaffidi, Melinda Rak, Sean Vig, Anshul Kogar, Ilija Zeljkovic, Ali Husain, Luiz H. Santos, Yuxuan Wang, Andrea Damascelli, Yoshiteru Maeno, Peter Abbamonte, Eduardo Fradkin, and Vidya Madhavan. Quasiparticle interference and strong electronâEUR"mode coupling in the quasi-one-dimensional bands of Sr_2RuO_4. *Nature Physics*, 13(8):799–805, 2017. ISSN 1745-2481. doi:10.1038/nphys4107. URL https://doi.org/10.1038/nphys4107.

[81] Yi Gao, Tao Zhou, Huaixiang Huang, C. S. Ting, Peiqing Tong, and Qiang-Hua Wang. Probing active/passive bands by quasiparticle interference in Sr_2RuO_4. *Phys. Rev. B*, 88:094514, Sep 2013. doi:10.1103/PhysRevB.88.094514. URL https://link.aps.org/doi/10.1103/PhysRevB.88.094514.

[82] Alireza Akbari and Peter Thalmeier. Multiorbital and hybridization effects in the quasiparticle interference of the triplet superconductor Sr_2RuO_4. *Phys. Rev. B*, 88:134519, Oct 2013. doi:10.1103/PhysRevB.88.134519. URL https://link.aps.org/doi/10.1103/PhysRevB.88.134519.

[83] Peter Thalmeier and Alireza Akbari. Quasiparticle scattering image in hidden order phases and chiral superconductors. *Journal of Magnetism and Magnetic Materials*, 400:23 – 26, 2016. ISSN 0304-8853. doi:https://doi.org/10.1016/j.jmmm.2015.07.059. URL http://www.sciencedirect.com/science/article/pii/S0304885315303656. Proceedings of the 20th International Conference on Magnetism (Barcelona) 5-10 July 2015.

[84] Henrik S. Røising, Thomas Scaffidi, Felix Flicker, Gunnar F. Lange, and Steven H. Simon. Superconducting order of Sr_2RuO_4 from a three-dimensional microscopic model. *Phys. Rev. Research*, 1:033108, Nov 2019. doi:10.1103/PhysRevResearch.1.033108. URL https://link.aps.org/doi/10.1103/PhysRevResearch.1.033108.

[85] A. Pustogow, Yongkang Luo, A. Chronister, Y.-S. Su, D. A. Sokolov, F. Jerzembeck, A. P. Mackenzie, C. W. Hicks, N. Kikugawa, S. Raghu, E. D. Bauer, and S. E. Brown. Constraints on the superconducting order param-

eter in Sr_2RuO_4 from oxygen-17 nuclear magnetic resonance. *Nature*, 574 (7776):72–75, 2019. ISSN 1476-4687. doi:10.1038/s41586-019-1596-2. URL https://doi.org/10.1038/s41586-019-1596-2.

[86] E. Hassinger, P. Bourgeois-Hope, H. Taniguchi, S. René de Cotret, G. Grissonnanche, M. S. Anwar, Y. Maeno, N. Doiron-Leyraud, and Louis Taillefer. Vertical Line Nodes in the Superconducting Gap Structure of Sr_2RuO_4. *Phys. Rev. X*, 7:011032, Mar 2017. doi:10.1103/PhysRevX.7.011032. URL https://link.aps.org/doi/10.1103/PhysRevX.7.011032.

[87] Satoshi Kashiwaya, Kohta Saitoh, Hiromi Kashiwaya, Masao Koyanagi, Masatoshi Sato, Keiji Yada, Yukio Tanaka, and Yoshiteru Maeno. Time-reversal invariant superconductivity of Sr_2RuO_4 revealed by Josephson effects. *Phys. Rev. B*, 100:094530, Sep 2019. doi:10.1103/PhysRevB.100.094530. URL https://link.aps.org/doi/10.1103/PhysRevB.100.094530.

[88] Y. Sidis, M. Braden, P. Bourges, B. Hennion, S. NishiZaki, Y. Maeno, and Y. Mori. Evidence for Incommensurate Spin Fluctuations in Sr_2RuO_4. *Phys. Rev. Lett.*, 83:3320–3323, Oct 1999. doi:10.1103/PhysRevLett.83.3320. URL https://link.aps.org/doi/10.1103/PhysRevLett.83.3320.

[89] O. Gingras, R. Nourafkan, A.-M. S. Tremblay, and M. Côté. Superconducting Symmetries of Sr_2RuO_4 from First-Principles Electronic Structure. *Phys. Rev. Lett.*, 123:217005, Nov 2019. doi:10.1103/PhysRevLett.123.217005. URL https://link.aps.org/doi/10.1103/PhysRevLett.123.217005.

[90] A. T. Rømer, D. D. Scherer, I. M. Eremin, P. J. Hirschfeld, and B. M. Andersen. Knight Shift and Leading Superconducting Instability from

Spin Fluctuations in Sr_2RuO_4. *Phys. Rev. Lett.*, 123:247001, Dec 2019. doi:10.1103/PhysRevLett.123.247001. URL https://link.aps.org/doi/10.1103/PhysRevLett.123.247001.

[91] W. Kohn and J. M. Luttinger. New Mechanism for Superconductivity. *Phys. Rev. Lett.*, 15:524–526, Sep 1965. doi:10.1103/PhysRevLett.15.524. URL https://link.aps.org/doi/10.1103/PhysRevLett.15.524.

[92] M. J. Lawler, K. Fujita, Jhinhwan Lee, A. R. Schmidt, Y. Kohsaka, Chung Koo Kim, H. Eisaki, S. Uchida, J. C. Davis, J. P. Sethna, and Eun-Ah Kim. Intra-unit-cell electronic nematicity of the high-Tc copper-oxide pseudogap states. *Nature*, 466(7304):347–351, 2010. ISSN 1476-4687. doi:10.1038/nature09169. URL https://doi.org/10.1038/nature09169.

[93] M H Hamidian, I A Firmo, K Fujita, S Mukhopadhyay, J W Orenstein, H Eisaki, S Uchida, M J Lawler, E-A Kim, and J C Davis. Picometer registration of zinc impurity states in $Bi_2Sr_2CaCu_2O_{8+\delta}$for phase determination in intra-unit-cell Fourier transform STM. *New Journal of Physics*, 14 (5):053017, may 2012. doi:10.1088/1367-2630/14/5/053017. URL https://doi.org/10.1088%2F1367-2630%2F14%2F5%2F053017.

[94] Yoichi Kamihara, Takumi Watanabe, Masahiro Hirano, and Hideo Hosono. Iron-Based Layered Superconductor La[O1-xFx]FeAs (x = 0.05-0.12) with Tc = 26 K. *Journal of the American Chemical Society*, 130(11):3296–3297, 2008. doi:10.1021/ja800073m. URL https://doi.org/10.1021/ja800073m. PMID: 18293989.

[95] G. R. Stewart. Superconductivity in iron compounds. *Rev. Mod. Phys.*,

83:1589–1652, Dec 2011. doi:10.1103/RevModPhys.83.1589. URL https://link.aps.org/doi/10.1103/RevModPhys.83.1589.

[96] C. C. Tsuei and J. R. Kirtley. Pairing symmetry in cuprate superconductors. *Rev. Mod. Phys.*, 72:969–1016, Oct 2000. doi:10.1103/RevModPhys.72.969. URL https://link.aps.org/doi/10.1103/RevModPhys.72.969.

[97] A F Kemper, T A Maier, S Graser, H-P Cheng, P J Hirschfeld, and D J Scalapino. Sensitivity of the superconducting state and magnetic susceptibility to key aspects of electronic structure in ferropnictides. *New Journal of Physics*, 12(7):073030, jul 2010. doi:10.1088/1367-2630/12/7/073030. URL https://doi.org/10.1088%2F1367-2630%2F12%2F7%2F073030.

[98] Kazuhiko Kuroki, Seiichiro Onari, Ryotaro Arita, Hidetomo Usui, Yukio Tanaka, Hiroshi Kontani, and Hideo Aoki. Unconventional Pairing Originating from the Disconnected Fermi Surfaces of Superconducting $LaFeAsO_{1-x}F_x$. *Phys. Rev. Lett.*, 101:087004, Aug 2008. doi:10.1103/PhysRevLett.101.087004. URL https://link.aps.org/doi/10.1103/PhysRevLett.101.087004.

[99] I. I. Mazin, D. J. Singh, M. D. Johannes, and M. H. Du. Unconventional Superconductivity with a Sign Reversal in the Order Parameter of $LaFeAsO_{1-x}F_x$. *Phys. Rev. Lett.*, 101:057003, Jul 2008. doi:10.1103/PhysRevLett.101.057003. URL https://link.aps.org/doi/10.1103/PhysRevLett.101.057003.

[100] Peter J. Hirschfeld. Using gap symmetry and structure to reveal the pairing mechanism in fe-based superconductors.

Comptes Rendus Physique, 17(1):197 – 231, 2016. ISSN 1631-0705. doi:https://doi.org/10.1016/j.crhy.2015.10.002. URL http://www.sciencedirect.com/science/article/pii/S1631070515001693. Iron-based superconductors.

[101] Y. Wang, A. Kreisel, V. B. Zabolotnyy, S. V. Borisenko, B. Büchner, T. A. Maier, P. J. Hirschfeld, and D. J. Scalapino. Superconducting gap in LiFeAs from three-dimensional spin-fluctuation pairing calculations. *Phys. Rev. B*, 88:174516, Nov 2013. doi:10.1103/PhysRevB.88.174516. URL https://link.aps.org/doi/10.1103/PhysRevB.88.174516.

[102] Helmut Eschrig and Klaus Koepernik. Tight-binding models for the iron-based superconductors. *Phys. Rev. B*, 80:104503, Sep 2009. doi:10.1103/PhysRevB.80.104503. URL https://link.aps.org/doi/10.1103/PhysRevB.80.104503.

[103] K. Umezawa, Y. Li, H. Miao, K. Nakayama, Z.-H. Liu, P. Richard, T. Sato, J. B. He, D.-M. Wang, G. F. Chen, H. Ding, T. Takahashi, and S.-C. Wang. Unconventional Anisotropic *s*-Wave Superconducting Gaps of the LiFeAs Iron-Pnictide Superconductor. *Phys. Rev. Lett.*, 108:037002, Jan 2012. doi:10.1103/PhysRevLett.108.037002. URL https://link.aps.org/doi/10.1103/PhysRevLett.108.037002.

[104] S. Maiti, M. M. Korshunov, T. A. Maier, P. J. Hirschfeld, and A. V. Chubukov. Evolution of the Superconducting State of Fe-Based Compounds with Doping. *Phys. Rev. Lett.*, 107:147002, Sep 2011. doi:10.1103/PhysRevLett.107.147002. URL https://link.aps.org/doi/10.1103/PhysRevLett.107.147002.

[105] D. Altenfeld, P. J. Hirschfeld, I. I. Mazin, and I. Eremin. Detecting sign-

changing superconducting gap in LiFeAs using quasiparticle interference. *Phys. Rev. B*, 97:054519, Feb 2018. doi:10.1103/PhysRevB.97.054519. URL https://link.aps.org/doi/10.1103/PhysRevB.97.054519.

[106] Frank Steglich and Steffen Wirth. Foundations of heavy-fermion superconductivity: lattice Kondo effect and Mott physics. *Reports on Progress in Physics*, 79(8):084502, jul 2016. doi:10.1088/0034-4885/79/8/084502. URL https://doi.org/10.1088%2F0034-4885%2F79%2F8%2F084502.

[107] Sheng Ran, Chris Eckberg, Qing-Ping Ding, Yuji Furukawa, Tristin Metz, Shanta R. Saha, I-Lin Liu, Mark Zic, Hyunsoo Kim, Johnpierre Paglione, and Nicholas P. Butch. Nearly ferromagnetic spin-triplet superconductivity. *Science*, 365(6454):684–687, 2019. ISSN 0036-8075. doi:10.1126/science.aav8645. URL https://science.sciencemag.org/content/365/6454/684.

[108] Tom M. Apostol. *Calculus, Vol.1*. J. Wiley, 1 edition, 1967.

[109] David J. Griffiths. *Introduction to Electrodynamics*. Cambridge University Press, 4 edition, 2017.

[110] S. Elitzur. Impossibility of spontaneously breaking local symmetries. *Phys. Rev. D*, 12:3978–3982, Dec 1975. doi:10.1103/PhysRevD.12.3978. URL https://link.aps.org/doi/10.1103/PhysRevD.12.3978.

[111] Mehran Kardar. *Statistical Physics of Fields*. Cambridge University Press, 1 edition, 2007.

[112] P. W. Anderson. Plasmons, Gauge Invariance, and Mass. *Phys. Rev.*, 130:439–442, Apr 1963. doi:10.1103/PhysRev.130.439. URL https://link.aps.org/doi/10.1103/PhysRev.130.439.

[113] Valery Rubakov and Stephen S Wilson. *Classical Theory of Gauge Fields*. Princeton University Press, 2002. ISBN 9780691059273. URL http://www.jstor.org/stable/j.ctt7snx1.

[114] L. D. Landau and E. M. Lifshitz. *Mechanics, Third Edition: Volume 1 (Course of Theoretical Physics)*. Butterworth-Heinemann, 3 edition, January 1976. ISBN 0750628960. URL http://www.worldcat.org/isbn/0750628960.

[115] Matthew D. Schwartz. *Quantum Field Theory and the Standard Model*. Cambridge University Press, 3 edition, 2014. ISBN 9781107034730. URL http://www.worldcat.org/isbn/9781107034730.

[116] Ryo Shimano and Naoto Tsuji. Higgs Mode in Superconductors. *Annual Review of Condensed Matter Physics*, 11(1):103–124, 2020. doi:10.1146/annurev-conmatphys-031119-050813. URL https://doi.org/10.1146/annurev-conmatphys-031119-050813.

[117] M. V. Berry. Quantal phase factors accompanying adiabatic changes. *Proceedings of the Royal Society of London Series A*, 392(1802):45–57, March 1984. doi:10.1098/rspa.1984.0023.

[118] Y. Aharonov and D. Bohm. Significance of Electromagnetic Potentials in the Quantum Theory. *Phys. Rev.*, 115:485–491, Aug 1959. doi:10.1103/PhysRev.115.485. URL https://link.aps.org/doi/10.1103/PhysRev.115.485.

[119] Di Xiao, Ming-Che Chang, and Qian Niu. Berry phase effects on electronic properties. *Rev. Mod. Phys.*, 82:1959–2007, Jul 2010.

doi:10.1103/RevModPhys.82.1959. URL https://link.aps.org/doi/10.1103/RevModPhys.82.1959.

[120] D. J. Thouless, M. Kohmoto, M. P. Nightingale, and M. den Nijs. Quantized Hall Conductance in a Two-Dimensional Periodic Potential. *Phys. Rev. Lett.*, 49:405–408, Aug 1982. doi:10.1103/PhysRevLett.49.405. URL https://link.aps.org/doi/10.1103/PhysRevLett.49.405.

[121] Klaus von Klitzing. Quantum Hall Effect: Discovery and Application. *Annual Review of Condensed Matter Physics*, 8(1):13–30, 2017. doi:10.1146/annurev-conmatphys-031016-025148. URL https://doi.org/10.1146/annurev-conmatphys-031016-025148.

[122] M. Z. Hasan and C. L. Kane. Colloquium: Topological insulators. *Rev. Mod. Phys.*, 82:3045–3067, Nov 2010. doi:10.1103/RevModPhys.82.3045. URL https://link.aps.org/doi/10.1103/RevModPhys.82.3045.

[123] Xiao-Liang Qi and Shou-Cheng Zhang. Topological insulators and superconductors. *Rev. Mod. Phys.*, 83:1057–1110, Oct 2011. doi:10.1103/RevModPhys.83.1057. URL https://link.aps.org/doi/10.1103/RevModPhys.83.1057.

[124] Liang Fu and C. L. Kane. Topological insulators with inversion symmetry. *Phys. Rev. B*, 76:045302, Jul 2007. doi:10.1103/PhysRevB.76.045302. URL https://link.aps.org/doi/10.1103/PhysRevB.76.045302.

[125] Jason Alicea. New directions in the pursuit of Majorana fermions in solid state systems. *Reports on Progress in Physics*, 75(7):076501, jun

2012. doi:10.1088/0034-4885/75/7/076501. URL https://doi.org/10.1088%2F0034-4885%2F75%2F7%2F076501.

[126] Masatoshi Sato and Yoichi Ando. Topological superconductors: a review. *Reports on Progress in Physics*, 80(7):076501, may 2017. doi:10.1088/1361-6633/aa6ac7. URL https://doi.org/10.1088%2F1361-6633%2Faa6ac7.

[127] Andreas P. Schnyder, Shinsei Ryu, Akira Furusaki, and Andreas W. W. Ludwig. Classification of topological insulators and superconductors in three spatial dimensions. *Phys. Rev. B*, 78:195125, Nov 2008. doi:10.1103/PhysRevB.78.195125. URL https://link.aps.org/doi/10.1103/PhysRevB.78.195125.

[128] Frank Wilczek. Majorana returns. *Nature Physics*, 5(9):614–618, Sep 2009. ISSN 1745-2481. doi:10.1038/nphys1380. URL https://doi.org/10.1038/nphys1380.

[129] Masatoshi Sato and Satoshi Fujimoto. Majorana Fermions and Topology in Superconductors. *Journal of the Physical Society of Japan*, 85(7):072001, 2016. doi:10.7566/JPSJ.85.072001. URL https://doi.org/10.7566/JPSJ.85.072001.

[130] C. Caroli, P. De Gennes, and J. Matricon. Bound Fermion states on a vortex line in a type II superconductor. *Physics Letters*, 9(4): 307–09, 1964. ISSN 0031-9163. doi:https://doi.org/10.1016/0031-9163(64)90375-0. URL http://www.sciencedirect.com/science/article/pii/0031916364903750.

[131] D. A. Ivanov. Non-Abelian Statistics of Half-Quantum Vortices in

p-Wave Superconductors. *Phys. Rev. Lett.*, 86:268–271, Jan 2001. doi:10.1103/PhysRevLett.86.268. URL https://link.aps.org/doi/10.1103/PhysRevLett.86.268.

[132] N. B. Kopnin and M. M. Salomaa. Mutual friction in superfluid ^{3}He: Effects of bound states in the vortex core. *Phys. Rev. B*, 44:9667–9677, Nov 1991. doi:10.1103/PhysRevB.44.9667. URL https://link.aps.org/doi/10.1103/PhysRevB.44.9667.

[133] J. M. Leinaas and J. Myrheim. On the theory of identical particles. *Il Nuovo Cimento B (1971-1996)*, 37(1):1–23, Jan 1977. ISSN 1826-9877. doi:10.1007/BF02727953. URL https://doi.org/10.1007/BF02727953.

[134] Frank Wilczek. Quantum Mechanics of Fractional-Spin Particles. *Phys. Rev. Lett.*, 49:957–959, Oct 1982. doi:10.1103/PhysRevLett.49.957. URL https://link.aps.org/doi/10.1103/PhysRevLett.49.957.

[135] Chetan Nayak, Steven H. Simon, Ady Stern, Michael Freedman, and Sankar Das Sarma. Non-Abelian anyons and topological quantum computation. *Rev. Mod. Phys.*, 80:1083–1159, Sep 2008. doi:10.1103/RevModPhys.80.1083. URL https://link.aps.org/doi/10.1103/RevModPhys.80.1083.

[136] Sergey Bravyi and Alexei Kitaev. Fermionic quantum computation. 2000. doi:10.1006/aphy.2002.6254.

[137] John Preskill. Lecture Notes on Quantum Computation, 2019. URL http://www.theory.caltech.edu/~preskill/ph219/ph219_2019-20.

[138] A. Yu. Kitaev. Fault-tolerant quantum computation by anyons. 1997. doi:10.1016/S0003-4916(02)00018-0.

[139] Graham Collins. Computing with Quantum Knots. *Scientific American*, 294:56–63, 05 2006. doi:10.1038/scientificamerican0406-56.

[140] Bernard Field and Tapio Simula. Introduction to topological quantum computation with non-Abelian anyons. *Quantum Science and Technology*, 3 (4):045004, jul 2018. doi:10.1088/2058-9565/aacad2. URL https://doi.org/10.1088%2F2058-9565%2Faacad2.